Acknowledgements

Throughout my time pursuing my Ph.D., I have benefitted from the support, advice, and friendship of numerous other students in the Department of Materials Science and Engineering. In particular, I'd like to acknowledge the members of my research group, Li Li and Yiling Zhang. Along with Li and Yiling, I'd like to thank some of the other members of my cohort, Ben Anglin, Patrick Callahan, Clay Stein, and Reeju Pokharel. Thanks also to Stephanie Bojarski, June Bott, Begum Gulsoy, Ayesha Hashambhoy, Ranga Kamaladasa, Ammon Lu, Clare Mahoney, Noey Munprom, Carolyn Norwood, Sutatch Ratanaphan, Ellen Reifler, Erica Sampson, Aswin Tejasukmana, Fatma Uyar, Lu Yan, and all the other members of the department who have made the past four years an enjoyable experience. June Bott deserves particular credit for giving me a place to live in the last few months of my time in Pittsburgh. The staff of the Materials Science and Engineering Department were hugely helpful in my successes. In particular, thanks to Jason Wolf for all his time and guidance, both technical and otherwise. Also thank you to Adam Wise and Tom Nuhfer. Thanks also to Marygrace Antkowski, Anita Connelly, Angela Pusateri, and Suzy Smith. Lastly, Jeanna Pekarcik deserves infinite thanks for all of her help and conversation throughout the years.

My time with the Graduate Student Assembly has provided some of the most rewarding experiences I've had and best friends I've made while at Carnegie Mellon. Particular thanks to my fellow GSA executive committee members, Dave Bergman, Will Boney, Grace Heckmann, and Jason Imbrogno. Thanks and good luck to my successors on GSA exec, Carolyn Norwood (again) and Ashlie Henery. Lastly, thanks to all the other people I've met through GSA, Emily Carson, Carolyn Denomme, Patrick Foley, Jon Kowalski, Amelia Kriss, Jessica Lyman, Zach Moir, and Ruth Poproski, each of whom contributed to an enjoyable experience at Carnegie Mellon, and probably at least one too many nights at PHI. My joining the Graduate Student Assembly was largely due to the friendship of Patrick Kelley, my first and best friend at Carnegie Mellon.

Carnegie Mellon University is a uniquely stimulating place to attend graduate school. That it remains so is due to the hard work of numerous members of the university

administration. I have had the pleasure of working with many of these people during my time with GSA, and am continually impressed by their devotion to improving the graduate student experience. In particular, Suzie Laurich-McIntire and the Office of Graduate Education deserve the thanks of every graduate student. I would also like to thank Amy Burkert, Gina Casalegno, Jared Cohon, Holly Hippensteel, Lisa Krieg, Michael Murphy, Kaycee Palko, and Gloriana St. Clair for their service to the university and its graduate students.

Lastly, and most importantly, thank you to my family, including my parents, Mike Schultz and Amy Thomas for their support and encouragement, not least of which being the financial support of my education. Also a sincere thank you to my sister and friend, Laura Schultz. I was raised in an environment conducive to learning, and I am continually thankful for the opportunities they have given me. Those opportunities are largely responsible for the person I am today.

ANDY SCHULTZ
Pittsburgh, PA
September 2012

Abstract

For photochemical hydrogen production to reach acceptable efficiencies, semiconductor photolysis systems that make use of visible light must be developed. This work presents results for the photochemical activity of iron-based materials and structures. Hematite, or α-Fe2O3, and BiFeO3 absorb light in the visible range.

The photochemical reactivity of bulk Fe2O3 and thin Fe2O3 films on single crystal and polycrystalline substrates is reported. Bulk Fe2O3 crystallites show strong anisotropic photochemical activity. Crystallites with a surface orientation near the hexagonal ($1\bar{2}10$) plane are significantly more reactive than other orientations. Thin Fe2O3 films supported on SrTiO3 (111) substrates are significantly more reactive than similar films on Al2O3 substrates and bulk polycrystalline hematite. Films on polycrystalline substrates showed similar orientation dependent reactivity as for bulk Fe2O3 crystallites, with higher reactivity than the bulk material. Overall, films supported on SrTiO3 substrates were more reactive than the bulk material and films on Al2O3 substrates.

Details on the growth via pulsed laser deposition of Fe2O3 films on perovskite SrTiO3 substrates are also reported. Orientation relationships between films and single crystal or polycrystalline substrates were determined using electron backscatter diffraction. Epitaxial (0001)-oriented films were grown on SrTiO3 (111) substrates. Films on SrTiO3 (001) substrates were polycrystalline, but showed preferred orientations based on alignment of close-packed (eutactic) networks. Films on polycrystalline SrTiO3 substrates also showed alignment of eutactic networks between substrate and film. The heteroepitaxial growth of polycrystalline films on polycrystalline substrates presents a much wider range of orientation conditions than available for growth on single crystals. Combinatorial substrate epitaxy, the growth and analysis using electron backscatter diffraction of films on polycrystalline substrates, opens many opportunities for wide-ranging epitaxy studies.

The photochemical behavior of BiFeO3 surfaces is reported. BiFeO3 surfaces exhibit spatially selective visible-light photochemical activity. Silver ions in solution were photochemically reduced by the BiFeO3, depositing solid silver on the surface in patterns corresponding to positive ferroelectric domains. This is suggested to arise from upward band bending in the negative domains that prevents electrons from reaching the surface and these locations do not reduce silver. Electric fields arising from ferroelectric domains

at the surface overwhelm anisotropy in the photochemical activity that might arise from grain orientation alone.

Contents

Introduction & Background

Experiments on Photochemical Activity

Experiments on Film Growth

Experiments on Bismuth Ferrite

Summary, Conclusions, & Future Paths

Appendix

List of Figures

List of Tables

Publications

Some ideas and figures have appeared previously in the following publications:

- Yiling Zhang, Andrew M. Schultz, Li Li, Harry Chien, Paul A. Salvador, and Gregory S. Rohrer, "Combinatorial Substrate Epitaxy: A high throughput method for determining phase and orientation relationships and its application to $BiFeO_3/TiO_2$ heterostructures," *Acta Materialia*, accepted for publication, 2012.
- Li Li, Yiling Zhang, Andrew M. Schultz, Xuan Liu, Paul A. Salvador and Gregory S. Rohrer, "Visible Light Photochemical Activity of Heterostructured $PbTiO_3/TiO_2$ Core-Shell Particles." *Catalysis Science and Technology* 2012, 2, 1945-1952.
- Andrew M. Schultz, Paul A. Salvador, and Gregory S. Rohrer "Enhanced photochemical activity of α-Fe_2O_3 films supported on $SrTiO_3$ substrates under visible light illumination." *Chemical Communications*, 2012, 48, 2012-2014.
- Andrew M. Schultz, Yiling Zhang, Paul A. Salvador, and Gregory S. Rohrer. "Effect of Crystal and Domain Orientation on the Visible-Light Photochemical Reduction of Ag on $BiFeO_3$." *ACS Applied Materials and Interfaces*, 2011, 3, (5), 1562-1567.
- Yiling Zhang, Andrew M. Schultz, Paul A. Salvador, and Gregory S. Rohrer. "Spatially selective visible-light photocatalytic activity of $TiO_2/BiFeO_3$ heterostructures." *Journal of Materials Chemistry*, 2011, 21, 4168-4174.

PART I

INTRODUCTION & BACKGROUND

Chapter 1

Introduction

1.1 MOTIVATION

Recent energy crises, along with increased worries about long-term fossil fuel supplies and the negative environmental effects associated with fossil fuel energy have driven research into alternative methods of energy production. One possible alternative, especially for mobile energy applications like powering automobiles, is hydrogen as a fuel source. For hydrogen to become a viable energy source, a new method of sustainable hydrogen production must be developed. The dominant method of industrial hydrogen production utilizes steam reformation of natural gas.[1] This process releases greenhouse gases into the atmosphere, ofsetting the environmental benefits of hydrogen combustion. A promising clean method of hydrogen production is the photolysis of water. This process uses the energy of solar photons to split water into hydrogen and oxygen gas. Fujishima and Honda[2] showed in 1972 that, under UV illumination, TiO2 can catalyze water splitting when used as an electrode in an photoelectrochemical cell. Since that discovery, many researchers have worked to develop systems to split water using TiO2.[3–7] Major improvements in the performance of photolysis systems are needed before they can compete with steam reformation. The efficiency of current systems is low, owing to charge carrier recombination within the photolysis catalyst and back reaction of intermediate species on the surface. Additionally, many photolysis catalysts are only able to absorb ultraviolet light, which makes up only a small portion of the solar spectrum. This combination of criteria, the need to engineer ways to improve efficiency of photolysis catalysts while also making use of a wider portion of the solar spectrum inspired the research presented in this document.

1.2 RESEARCH NARRATIVE

This work was guided by the aim of developing further understanding of the effects of polar surfaces and interfaces on photochemical activity. Polar surfaces give rise to

electric fields at material surfaces and at interfaces of heterostructures. These electric fields are believed to increase the photochemical activity of the structures by decreasing the rate of charge carrier recombination and increasing charge carrier drift to the surface. The experiments presented in this document test the effects of buried polar surface terminations on the photochemical activity of supported films. This document also represents a drive toward the utilization of visible light for photochemical reactions. Experiments were carried out testing the following questions:

- Do ferroelectric domains in a substrate affect the photochemical activity of supported films, even if the substrate material does not generate charge carriers?
- Does spatial selectivity corresponding to ferroelectric domains occur on p-type $BiFeO_3$ under visible light?

In the process of studying these questions, pulsed laser deposition of hematite Fe_2O_3 films was also examined. By growing films on polycrystalline substrates, a much larger array of orientation relationships between the substrate and film were examined. Initial photochemical experiments on hematite films suggested strong substrate effects on film photochemical activity. These observations led to experiments addressing the following questions related to the effect of polar surface terminations, hematite photochemistry, and hematite thin film growth:

- How do hematite films grow on perovskite substrates?
- Is it possible to stabilize and characterize epitaxial films on surfaces located far away from low index orientations?
- Do polar substrate surface terminations lead to increased reactivity on the surface of supported films?

1.3   HYPOTHESES

In the context of the stated questions driving this research, the following hypotheses are proposed:

- Charged interfaces increase the photochemical activity of heterostructured systems.
- Iron-based ferroelectrics and their heterostructures will show spatially selective reactivity under visible light.
- Fe_2O_3 films on single crystal and polycrystalline perovskite substrates will demonstrate a consistent orientation relationship between substrate and film

1.4   APPROACH

Hematite phase Fe2O3 was selected as a visible light, photochemically active catalyst to study the effect of charged surface terminations and ferroelectric domains on the photochemical properties of visible light active films. Fe2O3 film growth on SrTiO3 single crystals and randomly oriented polycrystalline SrTiO3 substrates was characterized via electron backscatter diffraction. Orientation relationships between the substrate and film were examined. Experiments testing the ferroelectric domain selectivity of reactivity of visible light active, p-type BiFeO3 was motivated by the previously observed spatial selectivity on BaTiO3, which is n-type and only reactive under ultraviolet illumination. The photochemical marker reaction of the reduction of aqueous silver ions to neutral silver was used to measure photochemical activity.

1.5   ORGANIZATION

This document is organized in five parts. Part I provides an introduction and background to the document, relevant scientific material, and experimental procedures. Part II contains results for experiments testing the photochemical activity of various hematite structures. The bulk reactivity of hematite, and its anisotropic photochemical activity, is reported in Chapter 4. The photochemical activity of hematite films on single crystal and polycrystalline substrates is reported in Chapters 5 and 6, respectively. Part III includes results for film growth experiments. Chapter 7 presents results for single crystal substrates and Chapter 8 for polycrystalline substrates. Part IV presents the results from early work on BiFeO3 that inspired the experiments comprising the bulk of this document. Finally, Chapter 10 summarizes the information in this document, and provides some context for future paths resulting from this work.

Chapter 2

Background

This chapter provides background information for the research presented in this document. The basics of semiconductor photochemistry are presented, as well as background on the effect of p-n junctions, ferroelectric polarization, and polar surfaces on photochemistry. The crystallography and relevant properties of the materials utilized in this document are also included.

2.1 PHOTOCHEMISTRY ON SEMICONDUCTOR SURFACES

When a semiconductor is illuminated by a photon with energy larger than the semiconductor's band gap, the photon can be absorbed by the semiconductor.[8] In this process, an electron is excited to the conduction band, leaving behind a hole in the valence band. If the electron-hole pair is generated near the surface, or is driven to the surface by an electric field, it can participate in surface chemical reactions. The process is illustrated schematically in Figure 2.1.

For water splitting (water photolysis),[9] the electrons and holes are used to drive the following reactions:

$$2\,H^+ + 2\,e^- \longrightarrow H_{2(g)} \qquad \text{(Reduction)} \qquad\qquad (2.1)$$

$$H_2O + 2\,h^+ \longrightarrow \tfrac{1}{2}\,O_{2(g)} + 2\,H^+ \qquad \text{(Oxidation)}. \qquad\qquad (2.2)$$
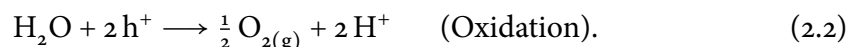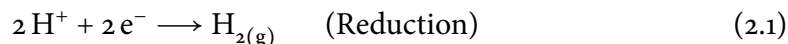
Only electrons and holes with appropriate electrochemical potentials can promote these reactions. The conduction band edge of the semiconductor must lie above the potential of the reduction reaction and the valence band edge must be below the potential for

FIGURE 2.1: Simplified schematic of the water photolysis process. A photon with an energy larger than the band gap is absorbed, exciting an electron from the conduction band to the valence band. The electron and hole are driven to the opposite surfaces by an electric field, represented here by sloped bands. At the surface, the charge carriers take part in photochemical reactions.

FIGURE 2.2: Array of band positions for traditional and oxide semiconductors. The area shaded in blue less than ~2.1 eV represents materials unsuitable for water splitting, as the band gap is not large enough to drive water splitting when overpotentials are considered. The shaded blue area between -1.23 eV and 0 eV on the hydrogen scale represents the position on the energy scale that must be straddled by the band positions. The valence band must be below -1.23 eV and the conduction band must lie above 0 eV.[8]

FIGURE 2.3: Solar irradiance at the earth's surface as a function of wavelength. The shaded regions represent the portion of the solar spectrum that can be utilized by a semiconductor with a 3.2 eV band gap (red) and a 2.0 eV band gap (blue).[12]

oxidation. An effective photocatalyst has a band gap that is both large enough to promote both reactions and is properly located in relation to the potential of each reaction. For water splitting, the hydrogen and oxygen half reactions are located at 0 V and 1.23 V respectively,[10] on the hydrogen scale. This requirement on the band gap and energy levels of potential photolysis catalysts is non-trivial. Figure 2.2 shows an array of the valence and conduction band energies of potential materials for water photolysis.[8] Only materials with electron and valence band energies in the white area of the array satisfy both requirements on the position of the energy levels of the semiconductor. Significant research efforts[11] are invested in the discovery and synthesis of new materials that satisfy the necessary energy requirements for water photolysis.

Photolysis and the Solar Spectrum

Before water photolysis can serve as a viable method of hydrogen production, systems must be made less expensive and more efficient. Major limitations on the efficiency of water photolysis are the separation of photogenerated charge carriers in the material and the utilization of a wider portion of the solar spectrum. After a photon is absorbed in a semiconductor and an electron is excited to the valence band, the electron or hole must reach the surface before recombining. Recombination is the process by which a photogenerated charge carrier combines with an oppositely charged carrier. Recombined electron-hole pairs represent lost efficiency, as the recombined electron no longer contains the necessary energy to drive photochemical reactions.

The solar spectrum is shown in Figure 2.3. The majority of the light reaching the earth's surface lies in the visible range of the electromagnetic spectrum, corresponding to photon energies of 1.6 eV to 3 eV. Titanium dioxide, TiO_2, one of the most studied photocatalysts, has a band gap of 3.2 eV. This value is well in to the ultraviolet portion of the solar spectrum. Only 2% of the light reaching the earth's surface is of sufficient energy to excite an electron in TiO_2. This means that for TiO_2, 98% of solar radiation is unavailable for use in water splitting. Moving to materials with a smaller band gap that can utilize light in the visual portion of the spectrum greatly increases the

FIGURE 2.4: (a) Photoelectrochemical cell. When light shines on the TiO2 electrode, an electron-hole pair is generated. The electron travels through an external 'circuit to the platinum electrode, where it generates hydrogen. The hole generates oxygen at the surface of the TiO2 electrode. (b) A particulate cell. In this case, oxidation and reduction occur on the same particle.

percent utilization of the solar spectrum. A shift to a material with a band gap of 2.0 eV, corresponding to orange light, represents an increased maximum absorption efficiency of using 34% of the solar spectrum. It should be noted that the absorption efficiency is always greater than the overall efficiency. Each absorbed photon is used to perform 1.23 eV of work, regardless of the energy of the photon. Any excess energy of the photon over the minimum for water splitting represents lost efficiency of the overall system. This goal of shifting to materials with smaller band gaps adds additional complexity to the selection of photolysis catalysts when viewed in connection with Figure 2.2. Smaller band gaps are desirable to make use of a wider portion of the solar spectrum, but the band edges must be located correctly in relation to the levels for the reactions of water splitting.

Photolysis Systems

Currently, research has concentrated on two systems for photolytic hydrogen evolution. The photoelectrochemical cell has shown promising efficiencies,[2,3] however it is too expensive for large scale hydrogen production. Particulate photocatalysts have the potential to be much less expensive than photoelectrochemical cells, however their efficiencies are much lower.[13] Because the electrodes in the particle catalysts are not physically separated as in the photoelectrochemical cell, charge carrier recombination limits the efficiency of the catalyst. Much of the work on particulate photocatalysts centers on creating physical separation of the anode (oxidation sites) and cathode (reduction sites).[14,15] Schematics of the photoelectrochemical cell and particulate photocatalyst are depicted in Figure 2.4.

In the photoelectrochemical cell depicted in Figure 2.4(a), the TiO2 electrode is illuminated, generating electrons and holes. The holes participate in oxidation at the TiO2 electrode, generating oxygen. The electrons travel through an external circuit to a platinum electrode separated by a salt bridge. At the platinum electrode, the electrons reduce hydrogen ions to form hydrogen gas. The particulate catalyst in Figure 2.4(b) represents a short-circuited version of the photoelectrochemical cell. Electrons and holes are generated in the TiO2 under illumination. Holes oxidize water at the surface of the TiO2 surface, while electrons travel to hydrogen particles on the surface, where they participate in reduction.

FIGURE 2.5: Schematic energy level diagram showing band bending at a semiconductor surface, along with a depiction of typical length scales relevant to semiconductor photochemistry.

Length Scales in Photochemistry

A number of competing characteristic length scales play an important role in semiconductor photochemistry. The ideal photolysis catalyst must optimize these characteristic lengths to achieve high efficiencies. The relevant lengths are labelled and compared in Figure 2.5. Each is discussed in the following section, including its importance to semiconductor photochemistry, relative magnitude, and relation to other relevant parameters.

The penetration depth of light into the semiconductor is the first important length to consider. Not all light is absorbed directly at the surface of the semiconductor. Instead, light penetrates into the semiconductor, its intensity decreasing as it travels further into the crystal and photons are absorbed. The penetration into the crystal is a function of the material's absorption coefficient, which itself is a function of light wavelength. The Beer-Lambert law (Eq. 2.3) describes how the intensity of incident light decays within a material, where z is the depth within the material and α is the absorption coefficient. The penetration depth is defined as the depth within the material where the ratio of intensity to incident intensity is reduced to $\frac{1}{e}$ (Eq. 2.4). This point occurs at $\frac{1}{\alpha}$ (Eq. 2.5).

$$I(z) = I_o e^{-\alpha z}, \tag{2.3}$$

$$\delta_p \equiv \frac{I(z)}{I_o} = \frac{1}{e}, \tag{2.4}$$

$$\delta_p = \frac{1}{\alpha}. \tag{2.5}$$

For hematite under illumination by a 470 nm blue LED (the material and light source used in the majority of experiments presented in this document), the penetration depth is ~450 nm. [16] The majority light absorption occurs within this length, and consequently the majority of electron-hole pairs are generated within this length.

Once an electron-hole pair is generated through the absorption of a photon, it must reach the surface to participate in a chemical reaction. If the electron-hole pair is generated within an electric field, that field will cause the electron and hole to move in opposite directions, causing one of the carriers to reach the surface. In the heterostructures used for experiments in this document, electric fields arise from built in sources. Details of these sources are presented in §2.2. In all of the presented cases, the presence of an electric field gives rise to a space charge region. On simple energy level diagrams such as the one in Figure 2.5 and others presented throughout this document, these electric fields are represented by bands bent at an angle relative to the horizontal axis. The width of this space charge region is an important value affecting the photochemical

performance of the semiconductor. Only electrons and holes that are generated within or near the space charge region are separated and driven to the semiconductor surface. In the example depicted in Figure 2.5, a space charge region is shown at the surface of the semiconductor, arising from the presence of surface states. The width of space charge region is governed by the one dimensional Poisson equation in

$$\frac{\partial^2 V}{\partial z^2} = -\frac{e^2 N_D}{\varepsilon \varepsilon_o}, \tag{2.6}$$

where $z = 0$ is defined as the surface of the material and N_D is the dopant density. After integrating twice, the solution takes the form

$$V(z) = -\frac{e^2 N_D}{2\varepsilon \varepsilon_o}(z - z_o)^2, \tag{2.7}$$

and if z is defined as 0 at the surface, and z_o is the width of the space-charge region (the point where $V = 0$), the width W of the space-charge region near the surface is

$$-(z - z_o) = W = \sqrt{\frac{2 V_{z=0}\varepsilon}{e^2 N_D}}. \tag{2.8}$$

A typical value for the width of the space charge region is 100 nm. This means that for Fe2O3, a significant portion of light absorption occurs beyond the width of the space charge region at the surface. Electron-hole pairs generated by this light are unlikely to reach the surface of the semiconductor to drive chemical reactions, and thus represent lost energy. Using Equation 2.4, the total percentage of light absorbed in the first 100 nm for hematite is only ~20%. 80% of the incident light is absorbed beyond the space charge region, and resulting photogenerated charge carriers are unlikely to reach the surface.

As stated in the last paragraph, electrons and holes must be generated within or near the space charge region to be separated and driven to the surface. While charge carriers generated within the space charge region are accelerated by the electric field towards or away from the surface, carriers generated near the space charge region must diffuse to it before they can be driven to the surface. The carrier diffusion length (L_n for electrons and L_p for holes) quantifies what specifically is meant by "near" the space charge region. The diffusion length is given by

$$L_{p,n} = \sqrt{D\tau}, \tag{2.9}$$

where D is the diffusion coefficient for the charge carrier and τ is the lifetime of the carrier. Only carriers generated within one diffusion length are likely to reach this region. Any charge carriers generated beyond the space charge width plus one diffusion length will not reach the surface, and represent lost energy.

In many of the experiments presented in this document, the light absorbing Fe2O3 material is present in the form of a thin film supported on a wider band gap substrate,

Figure 2.6: Simplified energy level diagram showing the movement of photogenerated charge carriers in an electric field. The electric field is represented by the sloped bands. Electrons move down on the band to lower energy states, while holes move up.

SrTiO3. In the case of visible light illumination, only the film is capable of absorbing the light. The thickness of the film then plays a major role in determining how much light is absorbed by the heterostructure. If the film is significantly thinner than the penetration depth of the light, a large portion of the incident light passes through the film without being absorbed, reducing the efficiency of the heterostructure. However, if the film is too thick, the band bending effects arising from the substrate-film interface described in Section 2.2 will be completely screened by charge carriers in the film. The film thickness must selected to ensure that a sufficient amount of light is absorbed (favoring a thicker film) while interface effects are not completely screened (favoring a thinner film).

Surface Activity Considerations

Surface roughness can significantly affect the photochemical properties of a semiconductor surface. Given two otherwise identical semiconductors, one with a rough surface and the other smooth, the sample with the rougher surface has a higher surface area exposed and, therefore, is expected to be more photochemically active. Photogenerated electron and holes must interact with species in solution to participate in chemical reactions. With a higher surface area, more reaction sites are available for the charge carriers and reaction species to interact, the reaction rate increases. This is one of the drivers of research into high surface area nanoparticles and films for photochemical applications.[15] For this reason, photochemical activity is often normalized by the active material's surface area. Where relevant, the affect of surface roughness on the interpretation of results is included in the results sections of this document.

2.2   CHARGED INTERFACES AND SURFACES

Under the presence of an electric field, electrons and holes are physically separated in a material. The electric field drives electrons and holes in the opposite direction. This is shown schematically in Figure 2.6. In simple energy level diagrams such as the one depicted in Figure 2.6, electric fields are represented by bands that are angled with respect to the horizontal axis. Electrons are accelerated towards a lower energy state by electric fields, corresponding to traveling "downhill" on the band diagram. The reverse is true of holes. Holes are driven "uphill" to higher energy states. The presence of electric fields is desirable in the case of photochemistry, as the fields can be engineered to drive electrons or holes to the sample surface, where they can participate in chemical reactions.

FIGURE 2.7: Three sources of charged interfaces. (a) Polarization from a ferroelectric $BaTiO_3$ core causes electric fields at the surface of a TiO_2 shell. (b) A p-n junction. At the interface, electrons and holes are driven in opposite directions by an electric field as a result of the p-n junction formed by n-type TiO_2 and p-type $BiFeO_3$. (c) Uncompensated charge at the interface between a core and film causes electric fields. The charge arises from incompletely compensated polar surface terminations at the interface between $SrTiO_3$ and TiO_2.

Electrons and holes that do not reach the surface of the material are eventually lost to recombination, reducing the photochemical efficiency. Heterostructure interfaces are an an established method of generating electric fields within a material. Three possible sources of electric fields in heterostructured interfaces are discussed in this section, including p-n junctions, ferroelectrics, and polar surface terminations. Each of these cases is depicted schematically in Figure 2.7.

p-n Junction

The presence of a p-n junction has long been known to separate photogenerated charge carriers. A p-n junction arises when a semiconductor with an excess of negative charge carriers (n-type) is placed in contact with a semiconductor with an excess of positive charge carriers (p-type). Excess charge carriers arise in semiconductors as a result of intentional doping with impurity atoms, or as a result of the processing conditions of the material. An intrinsic semiconductor, as in the case of pure silicon, has an equal concentration of electrons and holes. By including a small amount of an impurity element with more or fewer electrons in its valance shell than silicon, the semiconductor can be made p-type or n-type. For example, the inclusion of arsenic in a silicon semiconductor will make the silicon n-type. Arsenic has a five valence electrons, one more than silicon's four, contributing one excess electron for every arsenic atom. If boron, with three valence electrons, is added to pure silicon, the net result is one fewer electron in the material for each boron atom. This "missing" electron is termed a hole, and has a positive charge equal in magnitude to the charge on an electron. When studying semiconductors, it is useful to describe the hole as a particle, even through it actually represents the absence of an electron.

In oxide semiconductors, including all the materials discussed in this document, the bulk oxide often shows p-type or n-type conductivity even in the absence of intentional doping. This arises as a result of the processing conditions. The presence of oxygen vacancies gives rise to n-type oxides, while the presence of metal vacancies gives rise to p-type oxides. The defect reactions corresponding to the formation of oxygen or metal vacancies are:

$$MO \longrightarrow M_M + V_O^{\bullet\bullet} + 2\,e^- + \tfrac{1}{2}\,O_{2(g)} \quad \text{(Oxygen vacancy)} \tag{2.10}$$

$$MO \longrightarrow O_O + V_M'' + 2\,h^+ + M_{(g/l/s)} \quad \text{(Metal vacancy)} \tag{2.11}$$
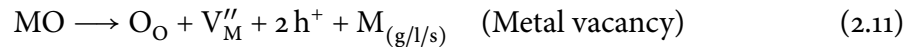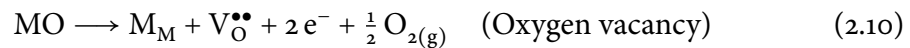
FIGURE 2.8: The formation of a p-n junction. When an n-type and p-type semiconductor are brought in contact, their Fermi levels align as electrons move from the n-type material into the p-type material. An electric field is created at the interface that drives photogenerated charge carriers in opposite directions.

Oxygen vacancies arise through equilibrium with the atmosphere during material fabrication. Increased oxygen partial pressure in during sintering leads to a decrease in oxygen vacancy concentration, and as a result, excess electron concentration. Volatile metal metal elements often lead to metal vacancies during high temperature sintering. For example, bismuth is easily lost to the atmosphere during the sintering of $BiFeO_3$, the photochemical properties of which are discussed in this document. The loss of bismuth during sintering leads to its p-type conductivity. Additionally, aliovalent substitution leads to increased charge carriers. For example, the presence of an ion in the 4^+ oxidation state on a 3^+ site leads to on extra free electron.

When n-type and p-type materials are joined, electrons near the junction in the n-type material diffuse into the p-type material, leading to charged regions. The missing electrons in the n-type region leave a region of net positive charge. The excess electrons that have diffused into the p-type material lead to a region of negative charge. These charged regions, collectively termed the space charge regions, give rise to an electric field. The field drives electrons and holes in opposite directions. If electrons-hole pairs are generated in the region of the electric field, the electrons are driven toward the n-type material, while holes are driven to the p-type material. The formation of the p-n junction and the resulting effect on photogenerated electron hole pairs are shown in Figure 2.8.

The p-n junction is the foundation for conventional solar photovoltaic technology. The photogenerated charges separated by the p-n junction are collected at either end of the device, resulting in a direct current. The same phenomenon also has potential use in photochemical devices, increasing the likelihood of photogenerated charge carriers reaching the surface of the semiconductor, where they can participate the chemical reactions.

Ferroelectric Polarization

Ferroelectrics are a subclass of a group of materials called piezoelectrics. Piezoelectrics are materials that exhibit an electrical polarity under an applied mechanical stress. The reverse is also true; piezoelectric materials deform under an applied electric field.[17] All piezoelectrics belong to one of the non-centric crystal classes. When a stress is applied to a centrosymmetric crystal, any movement of charge is symmetric, resulting in no net polarization. Charge movement is not symmetric when stress is applied to most non-centrosymmetric crystals, resulting in a net polarization across the crystal.[17]

Ferroelectric materials exhibit spontaneous polarization below a specific temperature, called the Curie temperature T_c, in the absence of an electric field.[17] Multiple

orientational configurations of the polarization vector exist, and an applied electric field can switch the orientation of the polarization vector from one state to another.[17,18] As the temperature of a ferroelectric material is lowered below the Curie temperature, different regions of the crystal polarize in each of the different directions. These regions of uniform polarization are called domains.[17–19]

At the surface of the crystal, the termination of the ferroelectric polarization gives rise to a depolarization field. Charge carriers within the crystal can move to the surface to counteract this field. If the field is perfectly compensated by charge carriers, then the energy associated with the depolarization field is zero. However, if the conductivity of the material is low, this compensation could take a very long time, resulting in high energies associated with the depolarization field. However, the formation of domains acts to minimize the energy associated with depolarization fields. The boundaries between domains, across which the polarization vector changes, are called domain walls. Domain walls are usually classified by the angle between the polarization vector on each side of the boundary. As the domain walls stray from the ideal crystal lattice arrangement, a nonzero energy is associated with their formation. The overall domain configuration of the crystal is determined in general by the balancing of the energy gained by reducing the depolarization fields and the energy cost of forming domain walls.

It has been shown that, for ferroelectric materials such as $BaTiO_3$, the domain structure effectively promotes photochemical oxidation and reduction on spatially distinct areas of the surface.[20–23] Domains with a positive polarization at the surface promote photochemical reduction, while domains with a negative surface polarization promote oxidation. The ferroelectric polarization acts to bend the bands at the surface. The positive polarization bends the bands downward, driving electrons to the surface. The negative polarization bends the bands upward, driving holes to the surface. This effect is shown schematically in Figure 2.9. Similar effects have also been observed in ferroelectric $Pb(Zr_xTi_{1-x})O_3$ (PZT) and $LiNbO_3$.[24–26]

By driving charge carriers in opposite directions, the ferroelectric fields reduce the recombination rates of electron-hole pairs generated in the space charge region near the surface of the ferroelectric. Additionally, because oxidation and reduction are occurring on distinct areas of the sample surface, the ferroelectric fields are hypothesized to reduce the rate of back reaction of intermediate products in the water splitting process. Burbure[21,27,28] demonstrated that the spatial separation of oxidation and reduction from ferroelectric domains persists, even when a thin film of TiO_2 was deposited on $BaTiO_3$. This phenomenon suggest the possibility of increased photochemical efficiency through the inclusion of ferroelectric interfaces.

FIGURE 2.10: The surface of an annealed SrTiO3 (111) single crystal before (a) and after (b) reaction with AgNO3. The silver is preferentially deposited on certain faces, corresponding to surfaces of different polar terminations.[29]

FIGURE 2.11: Band bending at the surface of an orientation with polar surface terminations. A positive surface termination bends the bands downward, favoring reduction. A negative surface charge bends the bands upward, favoring oxidation.

Polar Terminations

Giocondi[29] discovered that polar surface terminations can also result in spatially selective photochemical reactivity on the surface of SrTiO3. Figure 2.10 shows the surface of a (111) SrTiO3 single crystal before and after photochemical reaction with aqueous silver nitrate. The bright areas on the surface after reaction correspond to the reduced solid silver reaction product. The silver does not cover the entire surface. Instead, it appears as regions of total coverage and regions of no coverage. The shapes of these regions appear similar to the shapes of the terraces before reaction. Giocondi attributed this spatially selective reaction to the two possible surface terminations of the (111) SrTiO3 surface. As discussed in more detail in Section 2.4 on SrTiO3 crystallography, (111) SrTiO3 surfaces are terminated by either SrO_3^{4-} or Ti^{4+} layers. After measuring the step heights between the terraces on the clean surface, it was determined that regions of similar reactivity correspond to terraces separated by an even multiple of the spacing between lattice planes. Areas of differing reactivity were separated by an odd multiple. From this information, it was concluded that the areas of high reactivity shared the same termination, and all nonreactive areas shared the other termination.

It was hypothesized that the charge at these surfaces could lead to the presence of a space charge region at the surface, similar to that for ferroelectric polarization. Terraces with a SrO_3^{4-} termination have a negative surface charge, associated with a upward band bending at the surface. Ti^{4+} terminated surfaces have a positive surface charge, leading to negative band bending. This hypothesis is illustrated schematically in Figure 2.11. Up to this point, the effect of polar surface terminations on the photochemical reactivity of supported films has not been tested. The effect of the polar surface terminations of (111) SrTiO3 on the reactivity of hematite films is reported in this document.

2.3   EPITAXY

Epitaxy refers the ordered growth of new solid film phase on an existing solid material.[30–32] During epitaxial growth, the film phase and orientation can be controlled through proper choice of substrate and processing conditions. The periodic lattice of

FIGURE 2.12: Diagram showing the sets of parallel directions that describe epitaxial growth. The planes of the film and substrate parallel to the sample surface make up one pair. A direction within that plane makes up the second pair.

FIGURE 2.13: (adapted from Opel [30]) Effect of lattice mismatch on epitaxial growth and strain. When the film lattice parameter equals the substrate, as in (a), the film is unstrained. A smaller film lattice parameter (b) or larger film lattice parameter (c) than the substrate results in a strained film. (d) As the film grows thicker, dislocations appear in the lattice, reducing the strain state of the film.

the substrate drives the film to adopt a lattice with similar lattice parameters. Epitaxial film growth is an important aspect of electronic and optical technologies.

Depending on the nature of the materials involved in film growth, the type of epitaxy can be termed homoepitaxy or heteroepitaxy. Homoepitaxy refers to growth of the same material as the substrate. When the film material is different from the substrate material, the process is called heteroepitaxy. For example, this document reports on heteroepitaxial hematite films grown on perovskite substrates. Epitaxial growth is characterized by a consistent orientation relationship between the film and the substrate. This relationship is described by two orthogonal pairs of parallel directions. Generally, the first pair is the set of normals to the planes parallel to the sample surface in both the film and the substrate. The second pair is two parallel directions within that plane (one in the substrate, one in the film).

Predictions of epitaxial growth and the resulting orientation relationships typically look at a 2D analysis of the surface lattice parameters. If possible, the film material is energetically stabilized by forming a face and orientation that closely matches the substrate lattice parameter. The difference between the film and substrate lattice parameter is called the lattice misfit, and is given by

$$f = \frac{a_f - a_s}{a_s}, \tag{2.12}$$

where a_f is the film lattice parameter and a_s is the substrate lattice parameter.[30] When the lattice mismatch f is zero, the film lattice parameter is equal to the substrate lattice parameter and the film is unstrained. When f is less than zero, the film lattice parameter is smaller than the substrate lattice parameter and an epitaxial film will exhibit tensile in plane strain and compressive out of plane strain. When the reverse is true and f is greater than zero, the film experiences compressive in plane strain and tensile out of plane strain. As the film grows thicker, misfit dislocations can be introduced to the lattice, reducing the strain of the film. Above a certain thickness d_c specific to the film-substrate system, the film is relaxed, and additional layers are generally unstrained, excepting sources of local strain such as misfit and threading dislocations. Each of these cases is illustrated schematically in Figure 2.13.

FIGURE 2.14: The hematite hexagonal unit cell. Red atoms represent oxygen, and brown atoms represent iron. The structure is formed by hexagonal close packed oxide ions stacked along [0001] with ferric ions in two thirds of the octahedral interstices.

In this document, the nature of epitaxy for hematite film growth on various oxide substrates is explored. Initially, epitaxial growth was obtained on favorable substrates such as Al_2O_3 or (111)-oriented $SrTiO_3$ which are isostructural or have an isostructural surface lattice respectively. Then film growth, epitaxy and orientation relationships were observed for more unconventional substrates, including (001)-oriented $SrTiO_3$, which has a different surface structure than Fe_2O_3 or polycrystalline substrates, which expose complex high index surface planes. Film growth on these high index planes, and the resulting orientation relationships are reported in this document.

2.4   CRYSTALLOGRAPHY

Crystal structure plays an important role in the photochemical reactivity and epitaxy of oxide materials. The following sections give a brief overview of the crystallographic properties of the materials mentioned in this document.

Hematite

Hematite, α-Fe_2O_3, is a promising material for use as a photolysis catalyst because it has a band gap of about 2.2 eV, which lies well into the visible spectrum. [33] This band gap is also larger than the minimum required to split water, 1.23 eV. Additionally, Fe_2O_3 is inexpensive, readily available, chemically stable in aqueous environments, and doesn't contain environmentally hazardous elements. Hematite has been widely studied for photochemical purposes, [34] including as powders, [35] thin films, [36] and as a heterojunction component. [37,38] However, the efficiency of Fe_2O_3 as a photocatalyst is thought to be limited by low hole mobility and short carrier lifetimes. [34] Incorporating semiconductors in heterostructures to improve photochemical activity is widely reported. [39]

In this document, the photochemical behavior of Fe_2O_3 films on single crystal and polycrystalline substrates is discussed. Details of Fe_2O_3 film growth on these substrates are also reported, including the orientation relationships between Fe_2O_3 films and perovskite substrates. The corundum type structure of the hematite unit cell is shown in Figure 2.14. The structure is formed by layers of hexagonal-close-packed oxygen ions stacked along the [0001] direction, with iron(III) ions in two-thirds of the octahedral interstices. This arrangement is of importance when considering the heteroepitaxy of Fe_2O_3 films on perovskite substrates, presented in this document.

FIGURE 2.15: The cubic SrTiO3 unit cell. The cell takes the form of a cubic cell with the larger Sr cation (green) sitting on the cubic P lattice sites. The smaller Ti cation (blue) occupies the body centered position of the cubic cell, while the O anions (red) occupy the face centers of the unit cell.

Perovskites

The perovskite structure is formed by many materials with the formula ABO_3, where A and B are metal cations, and the A cation is significantly larger than the B cation.[40] The cell takes the form of a cubic cell with the larger A cation sitting on the cubic P lattice sites. The smaller B cation occupies the body centered position of the cubic cell, while the O anions occupy the face centers of the unit cell. This configuration can be described as AO_3 forming a cubic close packed network with B cations in one quarter of the octahedral interstices.

In addition to the prototypical cubic structures, perovskites are also found in a variety of distorted cubic lattices. Common perovskite distortions give rise to tetragonal, orthorhombic, and rhombohedral unit cells. The distortion of the unit cell gives rise to materials with many interesting properties, including ferroelectricity and ferromagnetism. Perovskite materials are widely studied[40] for applications in electronic devices,[41] fuel cells,[42,43] gas sensors,[44] superconductivity,[45] and catalysis.[46]

Strontium Titanate

Strontium titanate, SrTiO3, is a cubic perovskite at room temperature. It has a lattice parameter 3.905 Å. The unit cell of SrTiO3 is depicted in Figure 2.15. At room temperature, SrTiO3 takes the form of the prototype cubic perovskite described in Section 2.4, with Sr atoms on the primitive lattice sites, Ti atoms at the body center, and O atoms on the face centers of the cubic cell. The band gap of strontium titanate is 3.2 eV,[47] corresponding to the ultraviolet range of the electromagnetic spectrum. In this work, SrTiO3 was selected as a material for Fe2O3 film growth on single crystal substrates.

Depending on orientation, ideal SrTiO3 surfaces can be polar or nonpolar. The (001) face of strontium titanate is nonpolar, existing as neutral planes of either SrO or TiO2. The (110) and (111) surface are polar. In the case of (110) oriented planes, possible surface terminations are SrTiO4+ and O24-. For (111) oriented surface, surface terminations are SrO34- and Ti4+. Projections of the (001), (110), and (111) surfaces are shown in Figure 2.16. The effect of substrate surface polarity on photochemical behavior of supported films is discussed later in this document.

Bismuth Ferrite

Bismuth ferrite, BiFeO3, is ferroelectric, rhombohedrally distorted perovskite with a Curie temperature of ~830-850 °C.[48–51] The perovskite unit cell has the lattice con-

FIGURE 2.16: Models of the SrTiO3 (001), (011), and (111) surface. Red, green, and blue represent oxygen, strontium, and oxygen atoms respectively. The (001) surface is terminated by neutral TiO2 and SrO terminations. The (011) and (111) terminations are polar. The (011) surface is either SrTiO or O$_2$ terminated and the (111) surface is terminated by either Ti or SrO3 layers.

FIGURE 2.17: Pseudo-cubic BiFeO3 unit cell, showing rhombohedral [111] distortion and resulting ferroelectric polarization.[48]

stants a_{Rh} = 3.965 Å and α_{Rh} = 89.4°.[52] Because the rhombohedral distortion is so small (α_{Rh} = 89.4° versus 90° for a cubic cell), crystal directions and planes are typically referenced using the pseudocubic perovskite cell rather than the more complex rhombohedral or hexagonal systems. The pseudocubic unit cell is depicted in Figure 2.17. Bulk BiFeO3 is a p-type oxide semiconductor with reported band gaps of 2.3 eV to 2.8 eV.[53–55] The p-type conductivity arises from the loss of volatile bismuth during synthesis, resulting in cationic vacancies in the crystal lattice.

The ferroelectric polarization vector is observed along the pseudocubic <111> family of directions.[48] This gives rise to three possible types of domain walls: 180°, 109°, and 71°. 180° walls separate domains with antiparallel polarization vectors, for example, [111] and [$\bar{1}\bar{1}\bar{1}$]. If two of the components of the polarization vector are reversed across the boundary, it is a 109° wall, and if only one component is reversed, the boundary is a 71° wall. Equilibrium domain walls are constrained to certain orientations. 71° walls exist parallel to 110 planes, 109° walls parallel to {100} planes, and 180° walls on any plane containing the polarization vectors separated by the boundary.[56]

In contrast to BaTiO3, for which spatially selective reactivity has been observed and characterized, BiFeO3 has a band gap in the visible spectrum, is a p-type semiconductor, and has <111> type ferroelectricity. The spatially-selective photochemical properties of BiFeO3, taking into account these differences, were studied and are reported in this document.

Chapter 3

Experimental Overview

The purpose of this section is to provide an overview of the fabrication and characterization methods presented in this document. The main methods of sample fabrication covered in this chapter are solid state synthesis of polycrystalline ceramics and pulsed laser deposition of thin films. Characterization methods include microscopy, thin film phase and orientation characterization, and characterization of photochemical activity.

3.1   FABRICATION METHODS

Solid State Synthesis

Ceramic pellets were fabricated for use as polycrystalline substrates for film deposition. By using polycrystalline substrates, photochemical properties and film growth could be examined as a function of substrate orientation. In many cases, film growth occurs epitaxially across the entirety of a single substrate grain. The random texture of the substrate allows for measurement of properties across all possible orientations. As compared to growth on single crystals, where only low index orientations are typically available, this provides a much more diverse set of orientation conditions for examination.

All polycrystalline substrates and deposition targets were fabricated using a conventional solid state synthesis route. Starting powers of metal oxides or carbonates were measured in the correct stoichiometric proportions for the desired ceramic phase. Specific powders and purities are listed in the sintering recipes contained in Table 3.1.

These powders were ball milled in ethanol using yttria-stabilized zirconia (YSZ) grinding media (Inframet Advanced Materials, Manchester, CT). The powders were typically ball milled overnight to ensure complete mixing of the starting powders. The slurry was placed in a drying oven to drive off ethanol. The dry powders were placed in an alumina crucible and calcined to promote reaction of the starting powders into the desired final phase. After this reaction step, the powders were ball milled overnight in

Material	Starting Powder		Reaction Step		Burnoff		Densification		Grain Growth	
Fe_2O_3	Fe_2O_3	99.945%	—		600 °C	12 h	1200 °C	12 h	—	
$SrTiO_3$	$SrTiO_3$	99.97%	—		900 °C	10 h	1360 °C	10 h	1470 °C	3 h
$BiFeO_3$	Bi_2O_3	99.99%	650 °C	6 h	600 °C	12 h	750 °C	12 h	850 °C	3 h
	Fe_2O_3	99.945%								

TABLE 3.1: Sintering recipes for polycrystalline pellets used in this work. All starting powders were purchased from Alfa Aesar (Ward Hill, MA).

ethanol again. Before ball milling, a small amount (typically 1-2 wt%) of polyethylene glycol (PEG, MW8000,) was added to act as a binder. After ball milling, the powders were dried as before.

Pellets were formed of the dried powders under uniaxial loads in a stainless steel die. The diameter of the die was approximately 1 cm for polycrystalline substrates and 2.5 cm for film growth targets. The sides of the die were coated with a saturated solution of stearic acid in ethanol to act as a lubricant. A small amount of powder was added to the die. The die was placed on a manual hydraulic press and subjected to a load of 5000 pounds. The applied load was immediately released, and the pellet was ejected from the die. Pellets were placed in an alumina crucible, with a small amount of excess powder forming a barrier between the crucible and the pellets. Additional pellets were stacked, until the crucible was full or the desired number of pellets was reached. Any excess powder was loosely poured on top of the pellets to reduce loss of volatile elements to the atmosphere during sintering.

The crucible was placed in the furnace, and heated in air according to the desired sintering program. The same furnace was used to fabricate all specimens in this work. The furnace allows a programmable series of sintering steps. Typically, the furnace was held first at a low temperature to burn off organic materials in the pellet. Next, the temperature was increased to a point where densification and sintering occur. Finally, the temperature was increased to promote grain growth. Depending on the material, one or more of these steps may be omitted from the synthesis procedure.

After the samples were cooled to room temperature, they were removed from the crucible. Substrates were lapped flat and polished to provide a high quality surface for film growth, electron backscatter diffraction analysis, and photochemical reaction. All polishing was done using an autopolisher (Logitech, UK Scotland). Samples were affixed to glass substrates using melted wax (Logitech), which were held to a polishing jig with a vacuum. Lapping was performed using a steel plate and 9 μm alumina slurry (Buehler, Lake Bluff, IL). Both sides of each sample were lapped flat, ensuring that the sides were parallel and had a uniform flat surface. Deionized water was used to remove lapping residue. After both sides were flat, one side was polished. For final polishing, 0.01 μm colloidal silica (MasterMet 2, Buehler) was used with a polyurethane plate. The slightly basic nature of the colloidal silica results in a chemomechanical polishing

process, ensuring a smooth, flat surface. Polishing times varied for each material, but were on the order of ~30 minutes for each sample. Each sample was examined using optical microscopy to verify the removal of surface scratches and roughness. After polishing, the pellets were annealed a final time to heal surface damage from polishing and thermally etch the grain boundaries.

Pulsed Laser Deposition

Pulsed laser deposition (PLD) was used to fabricate the thin films discussed in this document. Benefits of PLD benefits include the ability to deposit stoichiometric oxides, rapid and simple changeout of target materials, precise control of film thickness, and easy control of deposition conditions.[57] A pulsed laser deposition system consists of a high power pulsed ultraviolet laser, a focusing optic system, and a vacuum chamber including an optical window for the laser, a target holder, and a substrate holder and heater. A schematic of the system used in this work is presented in Figure 3.1. The laser beam enters the vacuum chamber through the quartz optical window. The beam is aligned at a 45° angle from the target surface. The focused beam rapidly heats the target material in a process called ablation. The high incident flux and energy of the laser causes the formation of a plasma plume. The plume forms in a direction normal to the surface of the target. The plume expands in the chamber, its shape and size dependent on the energy of the laser pulse and the pressure of the process gas inside the chamber. The substrate is affixed to a heater located parallel to the target material. As the plume reaches the substrate, film nucleation and growth occurs. Each laser pulse delivers a relatively consistent amount of film material to the substrate, and resulting in typical growth rates on the order of 0.01 nm pulse^{-1}. By determining the growth rate via measurements of film thicknesses for films deposited with known numbers of pulses, accurate values of film thicknesses can be obtained.

The key parameters controlled during pulsed laser deposition are the substrate temperature, the pressure and composition of the process gas in the chamber, the target-substrate distance, the laser energy, and the laser repetition rate. The substrate temperature can strongly affect the crystallinity and phase of the resultant film. Higher substrate temperature increases the crystallinity of the film, and increases the likelihood of epitaxial growth.[58] The laser energy and repetition rate combine to affect the rate of arrival of material to the substrate. At higher laser energies, a greater amount of material is ablated from the target. If the laser repetition rate is increased, the time between pulses is reduced, and the rate of ablated material reaching the substrate is increased. By increasing or decreasing these values, kinetically or thermodynamically stabilized film phases can be deposited. The substrate-target distance affects the growth

FIGURE 3.1: Schematic of the pulsed laser deposition apparatus used in this work, showing the location of the substrate and target, and their relation to the pulsed laser beam.

rate of the material. If the substrate is placed closer to the target, a larger portion of the plasma plume is directed at the substrate, increasing the growth rate.

The process gas in the chamber during deposition and cooling affects film phase, composition, and growth rate. A dynamic oxygen atmosphere is commonly used during deposition to ensure the formation of oxide films. By varying the pressure of the oxygen during deposition, various stoichiometric oxide compositions can be created from a single metal or metal oxide target. Under high oxygen partial pressures, the formation of the more highly oxidized material is favorable. The reverse is true under vacuum or low oxygen pressures. In the scope of this work, a higher oxygen pressure during deposition creates favorable conditions for the formation of the desired Fe_2O_3 phase rather than FeO or Fe_3O_4. The atmosphere during post deposition annealing and cooling also can affect the phase of the resulting film.

A commercially available pulsed laser deposition system from Neocera (Beltsville, MD) was used for all film growth presented in this document. A KrF excimer laser (Coherent, Santa Clara, CA) with a wavelength of 248 nm was used for ablation. Unless otherwise noted, substrates were cleaned ultrasonically in acetone and then methanol. Substrates were affixed to the substrate heater with silver paint. The substrate-target distance was fixed at 6 cm for all depositions. The chamber was evacuated to a base pressure of 10^{-5} Torr before substrate heating began. Substrate heating and cooling rates were in the range of 20-30 °C min^{-1}, as regulated by a programmable temperature controller. While the substrate was heating, the target surface was cleaned by ablating it with the laser. During target cleaning, a shield was kept in between the target and the substrate to block the plume from reaching the substrate. Once deposition temperature was reached, a dynamic oxygen atmosphere was established by flowing oxygen through the chamber with the vacuum pump in operation. The shield between the target and substrate was removed, and the target was hit with a predetermined number of laser pulses to deposit the film. Immediately after deposition was completed, the chamber was sealed, and a static oxygen atmosphere was introduced into the chamber while the substrate cooled. Growth rates, laser energy, repetition rate, substrate temperature, and oxygen pressures were controlled across all film depositions in this document. Table 3.2 lists the values used.

The values used reflect conditions that produced the desired film results. Initial values were selected based on typical values for users of this PLD chamber. Once films of the desired phase were obtained, growth parameters were not further optimized. The only variable altered from film to film was the numbers of pulses, which was varied to control the resulting thickness of the deposited film.

Parameter	Typical Value
Substrate Temperature	800 °C
Laser Energy	160 mJ pulse^{-1} (2 J cm^{-2})
Laser Rep Rate	10 Hz
Deposition Gas Pressure	200 mTorr
Annealing Gas Pressure	200 Torr
Target Composition	α-Fe2O3
Growth Rate	0.01 nm s^{-1}

TABLE 3.2: Experimental parameters for the deposition of Fe2O3 films. These parameters were consistant across all depositions in this document.

FIGURE 3.2: Experimental setup for performing photochemical marker reactions. AgNO3 reaction solution is held in an O-ring under a quartz cover slip and the light source is positioned directly above the assembly.

3.2 CHARACTERIZATION METHODS

Marker Reactions

The established photochemical marker reaction of the reduction of silver ions in solution to solid silver on the sample surface was used to study the photochemical reactivity of the samples in this document.

$$Ag^+ + e^- \longrightarrow Ag_{(s)} \qquad (3.1)$$
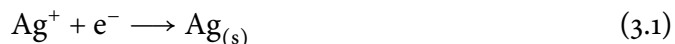
This reaction deposits insoluble silver on the surface, marking the locations where oxidation or reduction occurred.[20,21,23,28,59–62] The reaction product can subsequently be observed using conventional atomic force microscopy methods.

For all marker reactions performed in this document, aqueous solutions of 0.115 MAgNO3 (Fisher Scientific, 99.96%) were prepared. This specific concentration was established by earlier researchers,[20,21,23,28,59–62] and results in an easily observable reaction product on the surface after short illumination times. Figure 3.2 schematically illustrates the setup for performing photochemical reactions. A rubber O-ring was placed on the sample. A few drops of one of the solutions were added into the O-ring. A quartz cover slip (0.2 mm thick) was placed on top of the O-ring, held in place by surface tension. The cover slip creates a surface perpendicular to the incident light, ensuring the same volume of solution and setup geometry for all trials. The assembly was illuminated by commercially available blue LED (λ_{peak} = 470 nm, Philips Lumileds, San Jose, CA) or 300 W mercury arc lamp (Newport, Irvine, CA). The LED was powered by a DC supply,

set to deliver a constant current. Specific current and power values for illumination are given along with corresponding experimental results in later chapters.

The duration of illumination varied, depending on the material and light source. The reaction times used for collecting the data in this document were determined through multiple trials, varying the reaction time in each trial. If the samples are allowed to react for too long a duration, a the high amount of deposited solid makes characterization difficult. Conversely, if the samples aren't reacted for a long enough time, the amount of deposition is too low for observation. The times were selected because they resulted in an observable and quantifiable amount of reaction product on the surface. Times for individual photochemical experiments are listed in relevant sections of this document, along with their corresponding results. After reaction, the samples were rinsed with deionized water and dried with forced air.

To clean the surface of deposited products after reaction, the sample was wiped with a cotton swab, then cleaned ultrasonically, first in methanol and then acetone. The acetone was removed from the surface with a cotton swab. Subsequent microscopy demonstrates that reaction products can be completely removed from the sample surface.

For all results presented in this document, it was assumed that mass transport of species in the solution did not play a major role in interpreting the results from marker reactions. The results from marker reactions presented in this document are all comparable among experiments performed under the same conditions. For example, Chapter 5 compares the relative reactivity of three structures of Fe_2O_3 and Chapter 4 compares the relative reactivity of different Fe_2O_3 grains on the same polycrystal. In these cases, certain structures or grains were more reactive than others. It is possible that the rate of reaction of the most reactive grains or structures was rapid enough that mass transfer would be the limiting factor of reaction rate. However for each experiment, a comparison between the most reactive and the least reactive structures could be made. Mass transfer was not the limiting factor in the reactivity of the nonreactive or moderately reactive cases, as under the same experimental conditions, other samples exhibited much higher levels of reactivity.

Reaction solution pH can potentially exert a significant effect on photochemical properties of semiconductor photochemical systems. The pH of the solution affects the nature of adsorbed species (typically, though not exclusively, H^+ and OH^-) on the semiconductor surface, which in turn affect band bending within the space-charge region of the semiconductor. The isoelectric point pH_{iep} is defined as the pH level at which the no net charge exists on the surface. A solution pH level higher than this point causes a net negative charge on the surface, and a pH lower than the pH_{iep} causes a net positive charge on the surface. The effect of a solution pH on the band edges of the semiconductor is given by

$$E_{CB} = E_{CB}^{\circ} + 2.3k\text{T}\ln(pH - pH_{iep}), \hspace{2cm} (3.2)$$

where E°_{CB} is the band edge position at the isoelectric point. At room temperature, this results in a band edge shift of 60 mV with each increasing pH unit. In the results

presented in this document, pH effects are generally not considered to have a major effect on the interpretation of activity results. The reasoning for this is similar to that used for mass transfer effects. In the case of reactivity on Fe_2O_3 films, interpretations of results were comparative, with factors affecting pH controlled across all experiments. As all films on single crystals were of the same phase and orientation, negligible differences in pH effects between samples would be expected. In the case of bulk Fe_2O_3 and Fe_2O_3 films on polycrystalline substrates, in which the orientation of Fe_2O_3 is not controlled, differences in pH could affect the reactivity of the individual film grains. The effect of surface orientation on the isoelectric point varies depending on material. For example, the isoelectric point of rutile TiO_2 ranges between 3.2-3.7 for (100) faces and 5.5-5.8 for (001) faces, [63] while the range of isoelectric points reported for α-Fe_2O_3 is 6.3-8.5. [64–67] This variance is somewhat significant, and can result in a band edge shift on the order of 100 mV. For the scope of the work presented in this document, that shift is expected to be similar for all films, as preparation methods were consistent for all samples, and reaction conditions were the same.

A last point to consider regarding the photochemical marker reactions used in this work is differences in reactivity at various time scales. As the reaction proceeds, the potential for changes in reaction conditions affecting reactivity exists. The presence of silver on the surface immediately after the beginning of silver deposition changes the overall band structure of the system. Early on in the reaction, most of the surface is not covered by silver, but over longer timeframes, the affect of silver on the band structure is no longer negligible. Once again, the comparative nature of the interpretation of results should render negligible any affects from the change in the electronic properties of the system from the deposition of silver. These effects would be observed in all samples. Additionally, studies of the formation of silver nanoparticles in aqueous solutions suggest that silver particles may grow autocatalytically; [68,69] after the first silver atom forms, additional silver atoms are easier to reduce and the rate of particle growth increases. For the silver reaction product observed in the work presented in this document, distinct silver particles are observed. Surfaces classified as more reactive in this work have more individual particles on the surface. Thus the autocatalytic effects are not expected to be responsible for the increased reactivity, as this would only expand already nucleated particles.

EBSD

Electron backscatter diffraction (EBSD) was used as a primary tool for local determination of film phase, orientation, and film|substrate orientation relationships. Electron backscatter diffraction is a scanning electron microscopy technique that can probe the local orientation and microstructure of a material. [70,71] The technique relies on the interpretation of an electron backscatter pattern. This pattern is generated when an electron beam interacts with a flat surface, tilted at an angle of ~70°. The high angle increases the intensity of backscattered electrons escaping from the sample. As backscattered electrons are generated in the electron beam interaction volume, they exit the

FIGURE 3.3: Schematic showing the interior arrangement of a scanning electron microscope equipped with an EBSD detector.

FIGURE 3.4: Unindexed (a) and indexed (b) electron backscatter patterns for a (111) oriented BiFeO3 grain.

solid in patterns corresponding to the Bragg condition, a result of diffraction by atomic planes within the material. The result is a pattern of intersecting bands of high intensity when the diffracted backscatter electrons reach a phosphor screen in the SEM chamber. The phosphor screen is coupled to a CCD camera, which in turn captures an image of the pattern. A schematic of this arrangement is depicted in Figure 3.3.

Computer software (TSL, EDAX, Mahwah, NJ), is used to then analyze the location, intensity, and width of the bands. From this information, a set of Euler angles is obtained that describes the orientation of the crystal. The Euler angles represent the rotations that would rotate a crystal of a reference orientation to the sample orientation. From the Euler angles, a set of Miller indices are generated describing the local surface orientation in the crystal reference frame. A sample pattern for a (111)-oriented BiFeO3 grain and the computer-generated band indexing is shown in Figure 3.4.

This procedure, if repeated across a raster pattern of points, can be used to map orientations across a wide area of the sample. A computer can automate electron beam and stage control, pattern acquisition, and pattern indexing. This technique has a benefit of particular importance over other texture analysis techniques such as X-ray pole figures. Orientation data is locally determined at each point, rather than over a wide area of the sample simultaneously. This grants a great deal of flexibility when analyzing the orientation data. Maps of grains, grain boundaries characterization, pole figures, and inverse pole figures can be generated not just for the entirety of the dataset, but also for partitioned data of interest to a particular experiment. A representative map of grain orientations for a SrTiO3 polycrystal is presented in Figure 3.5.

EBSD was used in this work for analysis of Fe2O3 films grown on single crystal and polycrystalline substrates. It was used for film phase identification, film orientation measurement, and determination of epitaxial relationships between the film and substrate. All electron backscatter experiments were performed in a Quanta 200 FE-SEM (FEI Company, Mahwah, NJ) equipped with and EBSD detector using TSL software (EDAX) for pattern acquisition and data analysis. All experiments were performed in a low-vacuum atmosphere in the presence of water vapor. This allows for analysis of

FIGURE 3.5: Representative EBSD inverse pole map. This map depicts the microstructure of a SrTiO3 polycrystal.

weakly conducting samples such as those used in this experiment without the complications of sample charging from the electron beam. In all cases, clearly indexable electron backscatter diffraction patterns were obtained, even under low-vacuum conditions. The working distance was 15 mm. The tilt angle was always within 0.1° of of 70° from horizontal. Accelerating voltage was 20.0-25.0 kV. Exposure parameters for the CCD camera were adjusted as needed for each scan. Generally, the exposure time was adjusted to achieve a frame rate of 50-100 frames per second. Other parameters were then adjusted to obtain diffraction patterns with good contrast and accurate indexing of diffraction bands, as determined by manual inspection and computer-generated confidence index (CI). Computer image processing was used to improve the pattern quality. An average background signal was collected while scanning the beam over the sample. This background is subtracted by the computer for all collected patterns, to increase the contrast of the pattern. In some cases, additional processing such as dynamic background subtraction and normalizing of the intensity histogram were required to obtain good patterns. Scan parameters such as the scan area and distance between points were changed from sample to sample, and were dependent upon grain size, frame rate, and available microscope time.

X-ray

Conventional X-ray diffraction (XRD) characterization was used to verify the phase of polycrystalline samples and to determine the phase and orientation of thin film samples. In the experiments presented in this document, X-ray diffraction was used to verify the presence of a desired phase in synthesized materials. X-ray scans were performed using a Panalytical X'Pert Pro MPD diffractometer (Panalytical, Westborough, MA). After the diffraction pattern was collected, the results were compared with tabulated diffraction data from the International Center for Diffraction Data database.

X-ray reflectometry[72] was used to measure film thickness and calibrate growth rate. X-ray reflectivity relies upon interference between reflected beams from layers of material with different density. In this technique, the incident angle of the X-ray beam is slowly varied. As the reflected angle is changed, interaction between the reflected beam switches between constructive and destructive interference, causing fringes in the collected intensity data. Software is then used to calculate film thickness, given information about the composition and density of the materials under investigation. X-ray reflectometry scans were carried out on a Panalytical diffractometer. Using this data, the growth rate for films under the deposition conditions used in this document was determined. This growth rate was then used to select the appropriate deposition duration to deposit films of desired thicknesses.

Scanning Probe Microscopy

Sample surface profiles before and after photochemical reaction were examined using contact mode atomic force microscopy (AFM). AFM determines nanoscale displacements by measuring the deflection of a laser beam reflected off a microscopic cantilever.[45] Attached to the cantilever is a tip that moves along the surface of the sample. Piezoelectric elements are used to scan the tip across the sample. As the height of the sample changes, the tip is deflected, changing the measured intensity of the reflected beam. The microscope adjusts the height of the tip to account for the deflection, recording the magnitude of the adjustment. The records for the entire scanned area are constructed into an image corresponding to the topography of the sample.

AFM micrographs of sample surfaces were recorded before and after photochemical marker reactions. Conventional contact and semicontact methods were used.[73] All scans were collected on either an NTegra or Solver Next AFM (NT-MDT, Moscow, Russia). For contact mode images, aluminum coated silicon tips with a force constant of 0.11 N m^{-1} were used (CSG10, NT-MDT). For semicontact images, aluminum coated silicon tips with a rated resonant frequency of 240 Hz were used (NSG10, NT-MDT). Scan rates were chosen based on the size of the scan area, and were in the range of 0.5-2 Hz.

The local surface polarization of BiFeO3 was examined using piezoresponse force microscopy (PFM). Piezoresponse force is a contact mode technique used to determine the local polarization direction of ferroelectric materials.[74–77] While scanning the surface in contact mode, an AC bias is applied to the tip. Because ferroelectric materials are also piezoelectric, the applied bias causes a local expansion or contraction of the material. A lock-in amplifier is used to measure the phase of the expansion and contraction. From this data, the out of plane direction of polarization of the surface is determined. PFM measurements were collected using a SolverNEXT AFM. Titanium nitride coated tips with a force constant of 11.8 N m^{-1} were used (NSG10/Au, NT-MDT).

PART II

EXPERIMENTS ON PHOTOCHEMICAL
ACTIVITY

Chapter 4

Orientation Dependent Hematite Reactivity

Bulk and surface orientation have been shown to affect the photochemical reactivity of semiconductor surfaces. Orientation dependent photochemical reactivity has been observed for oxide semiconductors. For example, rutile and anatase TiO_2 microcrystals,[78] thin film rutile TiO_2,[79] and polycrystalline rutile TiO_2[61] have been shown to exhibit anisotropic activity. Microcrystals of $BaTiO_3$,[60] $SrTiO_3$,[80] and $Sr_2Nb_2O_7$[60] also exhibit different levels of reactivity for different crystal faces, as does bulk $SrTiO_3$ single crystals[29] and polycrystals.[81] Existing literature on the anisotropic photochemical activity of hematite differentiates between the basal and prismatic faces of hematite crystals.[82] There are no reports that differentiate the properties of various prismatic faces and high index orientations. The results presented in this chapter further our understanding of the anisotropic photochemical properties of Fe_2O_3, including high index orientations. In order to accurately decouple effects reported in subsequent chapters from microstructure, substrate charge, and film orientation on photochemical activity, the dependence of photochemical activity on crystallite orientation was examined. These results provide the baseline information for interpretation of other photochemical experiments on Fe_2O_3 presented in this document.

4.1   EXPERIMENTAL DETAILS

Electron backscatter diffraction (EBSD) was used to determine grain orientations of a polycrystalline α-Fe_2O_3 pellet. By using a polycrystalline sample, a wide variety of orientations, covering the entire range of the standard stereographic triangle representing all possible surface orientations, can be examined in a single experimental run.

A polished Fe_2O_3 pellet was prepared as described in Chapter 3. To promote grain growth, the pellet was sintered for at 1200 °C for 48 h in air, rather than the sintering procedure in Chapter 3. No other changes from the established sample synthesis procedure

Characterization Method	Xe Lamp	Blue LED
Optical	5 min	15 min
SEM	5 min	–
AFM	30 s	–

TABLE 4.1: Reaction times for photochemical experiments presented in this chapter. Reaction time varied depending on illumination source and observational technique. These times were selected to provide optimal imaging conditions for each technique.

were made. An orientation map of the sample was obtained using electron backscatter diffraction. Backscatter patterns were of consistent high quality over the entire examined area. Acquisition was performed under high vacuum with an accelerating voltage of 20 kV.

Photochemical activity was measured using the established reaction of the reduction of aqueous silver ions to neutral solid silver. Reactions were carried out under illumination from a narrow spectrum blue LED (Philips Lumiled, λ_{peak} = 470 nm and broad spectrum Xe arc lamp (150 W, Newport, Bozeman, MT). The reaction time was varied depending on the light source and characterization technique. Table 4.1 lists the reaction times used for this work. Reaction times were chosen to provide the best level of reaction product for the respective observation technique. For example, for optical microscopy, a large amount of reaction product will provide maximum contrast, but for atomic force microscopy, too many solid silver particles on the surface will cause difficulty in accurately measuring the topography of the surface.

The surface of the sample was examined before and after photochemical reaction with scanning electron (SEM), atomic force (AFM), and Kelvin probe force (KFM) microscopy. Scanning electron microscopy allow for rapid analysis of many grains simultaneously, but grains that have low (but nonzero) levels of reactivity may be missed. Atomic force measurements provide extremely accurate measures of reactivity, including low and moderate levels of reaction product, but are comparatively time consuming and difficult to obtain. All methods were used to verify the presence of reaction product on a wide range of crystallite orientations. Kelvin probe force microscopy was used to examine the local surface potential of reactive and nonreactive grains.

Scanning electron microscopy was performed using a Quanta 200 FE-SEM (FEI Company, Mahwah, NJ) with an accelerating voltage of 5.0 kV. AFM images were collected using an NTegra AFM (NT-MDT, Moscow) using standard semicontact techniques. KFM images were obtained using a SolverNEXT AFM (NT-MDT).

FIGURE 4.1: Representative SEM micrographs of Fe_2O_3 polycrystals taken after photochemical reaction showing reactive and nonreactive grains. Grains were identified as reactive by manual inspection. Reaction product appears as bright white areas within a grain. Reactive grains are outlined in red in these micrographs. Other sources of white contrast include grain boundaries and pores.

FIGURE 4.2: Electron backscatter diffraction inverse pole maps of the observed area of the Fe_2O_3 surface. (a) Map including all grains in the observed area. (b) The subset of grains identified as reactive during SEM analysis of the surface after photochemical reaction with $AgNO_3$. These grains correspond to the points on the standard stereographic triangle in Figure 4.3. The similar color of these grains in the inverse pole map suggests that the majority of active grains are similarly oriented.

4.2 RESULTS

Scanning Electron Microscopy

Figure 4.1 shows SEM micrographs of the Fe_2O_3 surface after reaction. Reaction product appears as bright areas within grains in the SEM micrographs. Additional white contrast appears in the form of grain boundaries and pores, presumably arising from charging of the weakly conducting sample. Reactive grains are outlined on the micrographs in Figure 4.1. Grains were manually identified as reactive or nonreactive. SEM images were collected to cover a large area of the sample. The images in Figure 4.1 are representative of all collected micrographs.

Figure 4.2 shows the complete inverse pole map collected via EBSD and a subset of the map corresponding to the grains marked as reactive during SEM observation. The grains identified as reactive generally fall within a similar color range, suggesting strong orientation effects on photochemical activity. The difference between reactive and nonreactive grains was very obvious for most grains; reactive grains were generally completely or mostly covered with bright reaction product, while nonreactive grains were completely devoid of any contrast from solid silver on the surface. The points identified as reactive were plotted on the standard stereographic triangle for hexagonal crystal systems, presented in Figure 4.3. This triangle represents the entire possible set of orientations. Points on the triangle represent observed reactive grains. With four exceptions, all points lie within about 10-15° from the $(1\bar{2}10)$ pole.

FIGURE 4.3: Reactive grains from Figure 4.2 plotted on the standard stereographic triangle for hexagonal crystals. Each point in the triangle represents the orientation of a grain identified as reactive. The blue shaded area outlines the cluster of highly reactive grains near the $(1\bar{2}10)$ orientation. With four exceptions, all observed reactive grains were oriented near this orientation.

FIGURE 4.4: Inverse pole map showing the portion of grains observed using atomic force microscopy. This source data for this figure is the same as for Figure 4.2.

Atomic Force Microscopy

To verify the rapid but imprecise classifications of reactivity obtained via scanning electron microscopy, the reacted sample was examined using atomic force microscopy. The results from the SEM images were used to determine appropriate locations for study. To increase the amount of data obtained through AFM, scan locations were selected that contained multiple grains, including both reactive and nonreactive grains as identified in SEM images. Six scan areas were selected, comprising a total of approximately 60 grains of varying orientation. Figure 4.4 shows an inverse pole map displaying which grains were observed using AFM.

Figures 4.5(a)-(c) show the representative AFM scans of the sample surface after reaction under illumination from a Xe arc lamp for 30 s. All scans have dimensions of 50 µm × 50 µm. Three levels of reactivity were manually assigned to each grain. Grains that were entirely covered in reaction product were labelled highly reactive. In Figure 4.5, these grains are outlined in blue. Grains with partial reactivity, such as reactive areas or grain edges were labeled moderately reactive. Figure 4.5(c) contains a moderately reactive grain, outlined in green.

After classifying all grains contained in the full set of AFM scans, each point was plotted on the standard stereographic triangle for hexagonal crystal systems, similar to Figure 4.3. The resulting triangle for AFM classification is depicted in Figure 4.6. As compared to Figure 4.3, the including of nonreactive and moderately reactive points provides additional information. Similar to the triangle constructed for the SEM results, all highly reactive grains are clustered near the $(1\bar{2}10)$ orientation. However, some moderately reactive or nonreactive grains are observed in this area as well. The data presented here suggest that not all grains oriented near $(1\bar{2}10)$ are highly reactive. At the same time, no highly reactive grains are observed far away from the $(1\bar{2}10)$ orientation. In summary, the data in this figure suggests that a reactive grain is likely near the $(1\bar{2}10)$ orientation, but that a grain having this orientation is not a guaranteed to exhibit high reactivity. It is proposed that this is a result of the symmetry of hematite. While not unusual to treat hematite as hexagonal, it is actually trigonal. For trigonal crystals, there

FIGURE 4.5: Representative AFM scans of three examined areas. Highly reactive grains are outline in blue. Moderately reactive grains are outlined in green. These scans are representative of all scans obtained via AFM. The size of each image is 50 µm × 50 µm.

FIGURE 4.6: All grains from Figure 4.5 plotted on the hexagonal standard sterographic triangle. Highly reactive grains are dark blue, moderately reactive grains are light blue, and nonreactive grains are open circles. All highly reactive grains are located near the $(1\bar{2}10)$ orientation.

FIGURE 4.7: Two representative KFM scans. Each row shows an optical micrograph of the scan area, from which grain reactivity was determined. Also depicted in each row are the simultaneously acquired topography and surface potential micrographs. Bright areas in the surface potential image correspond to higher surface potential. The topography image is included to demonstrate that contrast in the surface potential image is not an artifact of topography. The surface potential shows some features not present in topography and also omits features such as certain grain boundaries.

FIGURE 4.8: Plots of the average surface potential for each grain within each scan, as well as the amalgamated data from all scans. Reactive grains appear as blue boxes and nonreactive grains appear as read circles on the plots. With two exceptions, the grains with the highest surface potential in each scan were the most reactive. The average difference in surface potential between reactive and nonreactive grains was 70 mV.

are only three indistinguishable ($1\bar{2}10$) surfaces, rather than six. This difference may explain why on a subset of grains near the hexagonal ($1\bar{2}10$) orientation are reactive.

Kelvin Probe Force Microscopy

The local surface potential of reactive and nonreactive grains was obtained using Kelvin probe force microscopy (KFM). KFM is a two-pass semicontact mode technique. The first pass acquires the sample topography. During the second pass, the tip is lifted a user-defined distance above the sample surface. Using the topography data acquired during the first pass, the tip is kept at this same distance from the surface during the entire pass. An ac-bias is applied to the tip, causing it to oscillate. A dc-bias is then applied until the oscillations cease; this dc-bias corresponds to the local potential of the sample surface.

Figure 4.7 shows representative KFM scans of the Fe_2O_3 surface. Scan areas were selected to include both reactive and nonreactive grains, as determined in Section 4.2 and Section 4.2. Five total scans were obtained, comprising 29 identified grains. The simultaneously acquired topography and surface potential images are shown. Brighter contrast in the surface potential image represents higher surface potential. Consistently across all scans, reactive grains had a higher surface potential than nonreactive grains. Figure 4.8 plots the surface potentials of the grains within each scan, as well as one plot of all combined data. The surface potential for each grain was calculated using the average potential with a 10×10 pixel box at the center of each grain. Previously obtained optical images, also included in Figure 4.7 were used to categorize each grain as reactive or nonreactive. This classification is reflected in the plots in Figure 4.8. On average, reactive grains had a surface potential 70 mV higher than nonreactive grains. The correlation between highly reactive grains and a higher surface potential was clear for all scans. With only a few exceptions, the grains with the highest surface potential within each scan were the reactive grains.

4.3   DISCUSSION

The data show that hematite polycrystals exhibit extremely anisotropic photochemical activity. Grains oriented near the ($1\bar{2}10$) orientation are significantly more reactive than other grains at the surface. This remains true both under ultraviolet and visible light illumination. AFM images suggest that this is unrelated to the presence of facets at the surface. Both faceted and nonfaceted grains were observed to be reactive or nonreactive.

Earlier studies of photochemical anisotropic behavior of oxide polycrystals have attributed the effect to both surface and bulk properties. For example, Giocondi et al.[80] attributed the photochemical activity of SrTiO3 polycrystals to differences in the energy levels of the band dispersion. The authors suggested that higher rates of reactivity were the result of an increased generation of carriers with momentum along certain crystal directions. On the other hand, Lowekamp et al.[61] suggest that the increased reactivity of TiO2 polycrystals arises from the presence of highly active surface planes, rather than from a bulk property. Because of the lack of conclusive evidence supporting the bulk or surface cause of anisotropic photochemical reactivity for oxide polycrystals, both possibilities will be examined here.

For hexagonal crystal systems, studies of anisotropic properties often focus on property differences between basal and prismatic planes. The basal plane is defined as the plane perpendicular to the c-axis of the unit cell. The prismatic planes are the set of planes parallel to the c-axis, intersecting the a-axis directions of the unit cell. For example, in corundum-type materials, which includes α-Fe2O3, the structure consists of close-packed oxygen planes stacked along the c-axis, with Fe^{3+} ions filling two thirds of the interstitial sites. As a result, electron travel within the basal plane occurs within planes of iron ions, while travel perpendicular to the plane results in traversing layers basal layers of oxygen ions.[83] As a result, anisotropic electrical properties have been observed when comparing these directions.[84]

For Fe2O3, differences in electron conductivity between the basal plane and the prismatic planes are observed. Conductivity along the c-axis direction in Fe2O3 is lower than along perpendicualr directions.[83,85] Photochemical experiments determined that the onset of photocurrent for hematite basal planes is different than that of prismatic planes.[82] Prismatic faces of the crystal showed an earlier onset of photocurrent than basal planes. That study only differentiated between properties of the basal plane and the prismatic planes, and did not study differences in properties between the prismatic faces. The work presented here shows a strong difference in photochemical properties not only between the basal and prismatic orientations, but also determined that one prismatic orientation is significantly more reactive than the others.

The two low-index prismatic orientations of Fe2O3 are (in 4-index notation) the {$1\bar{2}10$} and the {$10\bar{1}0$} families. These planes are depicted in Figure 4.9. Polycrystalline grains near the ($1\bar{2}10$) orientation were significantly more reactive than all other orientations, including the ($10\bar{1}0$) orientation. The data acquired from Kelvin probe force microscopy show that the reactive orientation are associated with a higher surface potential than the surrounding nonactive grains. It is logical that grains with a higher

FIGURE 4.9: Schematic showing the (1$\bar{2}$10) and (10$\bar{1}$0) planes in relation to the in-plane hexagonal crystal axes. Also shown are the close-packed directions of the close packed oxygen network of the basal plane. These close packed directions are located 30° from the in-plane crystal axes. The (1$\bar{2}$10) planes are perpendicular to the axes of the unit cell, while the (10$\bar{1}$0) planes are perpendicular to the close packed directions.

surface potential correspond to a higher reactivity for photochemical reduction reactions, which includes the reduction of aqueous silver in this work. A more positive potential at the surface would decrease upward or increase downward band bending at the surface. In this case, reactive grains were an average of 70 mV more positive than nonreactive grains.

An examination of the possible surface terminations of prismatic hematite orientations gives a possible explanation for the increased reactivity. Figure 4.10 shows atomic models of the (1$\bar{2}$10) and (10$\bar{1}$0) planes of Fe_2O_3. The (10$\bar{1}$0) is neutral, terminated by a

FIGURE 4.10: Depiction of the (a) (10$\bar{1}$0) and (b) (1$\bar{2}$10) terminations of hematite. The (10$\bar{1}$0) surface is terminated by a neutral formula unit. Outlined atoms in (a) represent the neutral repeating 2D unit cell. The (1$\bar{2}$10) surface is terminated by a polar termination of either a layer of iron atoms or oxygen atoms. (c) Side view of the (1$\bar{2}$10) surface, showing alternating layers of O or Fe atoms.

formula unit of Fe^{3+} and O^{2-} ions. On the other hand, the (1$\bar{2}$10) surface is terminated by alternating layers of O^{2-} and Fe^{3+}. For Fe_2O_3 films on single crystal substrates presented in the following chapter, polar surface terminations are present in the more reactive case. The basal plane is also terminated by polar planes, but as already stated, mobility along the c-axis is low, which would account for lack of active orientations along this direction.

Giocondi et al.[80] hypothesized that differences in photochemical reactivity of $SrTiO_3$ arise from preferred charge carrier generation along certain crystallographic directions. Figure 4.11 presents a calculated band dispersion for hematite Fe_2O_3. For hexagonal crystals, Γ represents the center of the Brillouin zone. Γ→A represents charge carriers generated along the c-axis direction (parallel to the [0001] direction). Γ→M represents carriers generated perpendicular to the (1$\bar{2}$10) plane (parallel to a prismatic axis). Γ→K represents the generation of carriers perpendicular to the (10$\bar{1}$0) orientation,

FIGURE 4.11: Calculated hematite band electronic band structure. The bands were reproduced from Huda et al.,[85] but have been rigidly shifted to reflect the experimentally observed band gap. The shaded region represents the momentum states where vertical transitions are possible with the energy of light from the blue LED used in these experiments.

traveling in a direction 30° offset from a prismatic axis, along a close packed oxygen direction.

The band structure gives another explanation for the low reactivity of (0001) faces of bulk hematite. The direct band gap for electrons traveling perpendicular to this face is on the order of 0.3-0.5 eV larger than for electrons traveling toward the prismatic faces. The larger band gap is expected to result in fewer charge carriers generated in that direction than for the other faces. This is particularly true in the case of illumination by the wide spectrum Xe lamp, which generates more low energy photons than the blue LED. However, the band dispersion shows little difference in the band gap when comparing the M and K points, which correspond to the $(1\bar{2}10)$ and $(10\bar{1}0)$ zones respectively.

4.4   CONCLUSIONS AND CONTEXT

The $(1\bar{2}10)$ orientated grains of polycrystalline Fe_2O_3 are significantly more reactive than all other orientations, including other low index prismatic orientations. Reactive grains correspond to grains with a higher surface potential, as determined through Kelvin probe force microscopy. The anisotropy in photochemical activity is the same for reactions performed under wide spectrum light including ultraviolet light as well as for narrow spectrum visible light from a blue LED. The reactive orientation corresponds to a prismatic direction terminated by polar surface planes with a significant number of low energy electrons having momentum in that direction.

In the context of the other work presented in this document, these results serve to clarify some of the complicated results presented in later chapters and introduce the effect of polar surface terminations on photochemical reactivity. This work provides information on base reactivity of bulk, polycrystalline hematite. It also correlates reactivity with grain orientation. These results provide a context for future results. For example, for bulk hematite, the c-axis (0001) orientation is consistently not as reactive as the $(1\bar{2}10)$ face, and orientation is not a key factor driving the results for films on single crystals presented in Chapter 5. Similar interpretations can be applied to the results for films on polycrystalline substrates presented in Chapter 6.

Chapter 5

Hematite Reactivity on Single Crystal Substrates

The majority of the text in this chapter appears in *Chemical Communications*, 2012, 48 (14), 2012-2014.[86] This chapter describes the reactivity of thin films of α-Fe2O3 on various single crystal substrates. The key discovery reported in this section is that thin films of α-Fe2O3 show drastically differing levels of photochemical reactivity when supported on different substrates. (0001)-oriented Fe2O3 on (111)-oriented SrTiO3 substrates are significantly more reactive than films supported on (0001)-Al2O3 or even bulk polycrystalline Fe2O3. Previous work in the SrTiO3/Fe2O3 system has focused on improving the activity of SrTiO3 through the incorporation of Fe2O3 as an electron scavenger.[37,38] Those experiments tested the activity of the heterostructures towards photochemical oxidation (with SrTiO3 acting as a photoanode). Here, the behavior of Fe2O3/SrTiO3 heterostructures is tested in the reverse configuration. Fe2O3 is the active material, supported on SrTiO3, and acts as a photocathode for reducing aqueous Ag^+ to solid Ag.

5.1 EXPERIMENTAL DETAILS

Fe2O3 films were deposited on various substrates using pulsed laser deposition. Basic procedures outlined in Chapter 3 were followed for pulsed laser deposition and synthesis of a polycrystalline hematite target. Films were deposited on single crystal SrTiO3 (111) and Al2O3 (0001) substrates. Both films were verified as (0001) oriented via X-ray diffraction. Bulk Fe2O3 was prepared as described in §3.1.

5.2 RESULTS

Figure 5.1 shows AFM images of the film surfaces before and after reaction with the AgNO3 solution. Figure 5.1(a) and Figure 5.1(b) show the clean surface of the Fe2O3

FIGURE 5.1: Topographic AFM images of sample surfaces before (a-c) and after (d-f) the photochemi-cal reduction of Ag from an aqueous AgNO3 solution. (a) and (d) show the surface of the Fe2O3 film supported on Al2O3, (b) and (e) show the Fe2O3 film on SrTiO3, and (c) and (f) show bulk polycrys-talline Fe2O3. The arrows next to the micrographs in (d-f) indicate the location of the horizontal line used for Figure 5.2.

FIGURE 5.2: Topography along lines from the AFM micrographs in Figure 5.1.
The arrows next to the micrographs in Figure 5.1(d)-(f) indicate the location of the horizontal line used for Figure 5.2.

films on SrTiO3 and Al2O3, respectively. Figure 5.1(c) shows the clean surface of bulk Fe2O3. The corresponding surfaces after reaction are shown in Figures Figure 5.1(c)-(e). All areas are 10 μm x 10 μm, but the vertical scales differ. After reaction, the surface of the film on alumina, Figure 5.1(d), shows occasional small silver deposits, visible as bright spots on the micrograph. The surface of the film on the SrTiO3(111) substrate, shown in Figure 5.1(e), is covered in a thick, inhomogeneous layer of reaction product. The amount of silver present after reaction on the film supported on the SrTiO3 substrate is much greater than for the film on alumina or for the bulk sample in Figure 5.1(f). Of particular note is the difference in vertical scales for the micrographs after the photochemical reduction of Ag. The vertical scale for the reaction on the SrTiO3 supported film is 290 nm, as compared to 100 nm and 68 nm for the film on alumina and the bulk hematite, respectively. The (0001) oriented film on SrTiO3 is significantly more reactive than the (0001) grains observed for bulk Fe2O3, reported in Chapter 4.

Figure 5.1. The differences in the heights of the Ag on the three surfaces are shown quantitatively in Figure 5.2, which compares the topography along lines from the three micrographs in Figure 5.1(d)-(f). The heights of the Ag deposits on the α-Fe2O3/SrTiO3(111) heterostructure range from 100 to 250 nm. On the other two surfaces, all of the deposits are less than 100 nm. The images in Figure 5.1 are characteristic of all areas that were examined.

The results presented in this chapter were consistently observed over multiple sam-ples. In all cases, the film on SrTiO3(111) was significantly more reactive than the film on alumina. The reactivity difference was so extreme that it could be used to visually distinguish the films after reaction. After longer reaction times (on the scale of minutes to an hour), the entire surface of the film supported on SrTiO3(111) was covered with silver reaction product, and excess silver was visible floating in the reaction solution. On the film on alumina after the same reaction time, little to no reaction product could be observed with the naked eye.

5.3 DISCUSSION

The results presented in Figure 5.1 and Figure 5.2 demonstrate that the α-Fe2O3 film on SrTiO3(111) has a much higher photochemical reactivity for the reduction of silver ions than a comparable film on Al2O3 and even bulk hematite. The images in Figure 5.1 reveal that the film on SrTiO3 has the greatest silver surface coverage. The data in Figure 5.2 show that the silver deposits are larger for films on SrTiO3 than for films on alumina or for bulk Fe2O3.

This result is surprising for multiple reasons. The structure of both films does not vary enough to cause the marked difference in reactivity. Both films are (0001)-oriented α-Fe2O3 of nominally equal thickness. AFM scans show that the morphology of the films is similar. The thickness of the films used in this experiment was ~50 nm. Based solely on the depth of light absorption in Fe2O3, one could expect the bulk sample to be much more reactive than the films. The penetration depth of 470 nm photons in hematite reported to be approximately 450 nm.[16] The films were of a sufficient thickness to absorb only a fraction of the incident light, in contrast to the bulk sample, which was much thicker than the absorption depth. Furthermore, based on the index of refraction mismatch, the Al2O3/Fe2O3 interface is more reflective than the SrTiO3/Fe2O3 interface, so internal reflection leading to an increase in path length in the film cannot account for the difference in reactivity. In both cases, the band gap of the substrate (> 8 eV for Al2O3,[87] and 3.2 eV for SrTiO3[47]) is too large for the light used in this experiment to generate a significant number of electron-hole pairs. We can therefore conclude that the majority of the electron hole pairs were generated in the films. Neither substrate was able to participate in photochemical reactions by absorbing light and shuttling generated charge carriers to the surface of the film, as seen in previous experiments with UV light and TiO2/BaTiO3 heterostructures.[21,28] Despite the fact that it absorbs less light, the film supported by SrTiO3 was more reactive than the bulk sample.

One possible explanation for the increased reactivity of the film supported on SrTiO3 lies in the band structure of the substrate materials. Previous authors investigating the SrTiO3/Fe2O3 system have suggested that the Fe2O3 layer acts as an electron acceptor transferring holes to the active SrTiO3 photoanode.[38] If Fe2O3 acts as a sink for electrons at the back of the active layer, more holes can reach the surface without recombining. One could make the reverse argument here to explain the current observations. In this case, the SrTiO3 layer can act as a hole acceptor, increasing the number of photogenerated electrons that reach the Fe2O3 surface to participate in the photocathodic reaction. This could explain why the thin film sample has a much higher reactivity than the bulk material, even though less light is absorbed. Because the band gap of alumina is significantly larger than that of the Fe2O3 film, there exists a significant barrier to charge transfer across the interface. As a result, the alumina substrate cannot accept holes, and the recombination rate within the film is not decreased.

Assuming SrTiO3 acts as a hole acceptor and this is responsible for the increased reactivity, we must also consider what happens to these holes. In our experimental set-up, there is no path to ground or to complete the circuit with the solution. If the

FIGURE 5.3: Schematic depiction of the charges at the internal interface between SrTiO3(111) and α-Fe2O3. There are alternating planes of charge along the [111] direction and some areas are positively terminated (upper) and others have a negative termination (lower). The charged termination will cause the bands in the film to bend in a way that will move carriers in opposite direction. E_C and E_V label the conduction and valence band edges, respectively.

holes were to build up in the substrate, the heterostructure would become charged and the reaction would stop.

A second explanation is that uncompensated charge at the SrTiO3(111) acts to separate electrons and holes, reducing recombination. The individual (111) atomic planes in the SrTiO3 structure have alternate positive (Ti^{4+}) and negative charges (SrO_3^{4-}). Terminating the surface in a single charge is energetically costly, so the surface breaks up into positive domains with Ti termination and negative domains with SrO3 termination. Giocondi[29] has shown that the oppositely charge surface domains have different photochemical properties, with one favoring reduction and the other favoring oxidation. Note that α-Fe2O3 also has planes of alternating charge parallel to the interfaces plane. However, the trivalent charges of the (0001) planes cannot completely compensate the charge from the SrTiO3(111) surface. These charges can, however, exactly compensate the charges on the isostructural, isoelectronic Al2O3(0001) surface. Figure 5.3 illustrates a schematic view of our proposed explanation for the enhanced reactivity of α-Fe2O3/SrTiO3(111) heterostructures. In the hematite film above positively terminated domains, bands bend downward and draw photogenerated electrons to the internal interface while holes are drawn to the hematite/solution interface. The opposite occurs in negative domains and this is where the reduction of silver occurs. In each case, the complementary carriers can recombine within SrTiO3, so there is no charge accumulation. Note that the previous work showed that charged domains on the SrTiO3(111) surface have dimensions on the order 1-2 μm (refer to Figure 2.10). This may account for the highly heterogeneous distribution of Ag on the surface of the heterostructure in Figure 5.1(e).

Finally, it is noted that the lattice parameter mismatch is significantly larger for films on alumina than films on SrTiO3. The mismatch between the a-axis lattice parameter for Fe2O3 and the atomic spacing of (111)-SrTiO3 is 3.2%. The mismatch between alumina and hematite is ~20%. As a result, the films on alumina are expected to have a much higher defect concentration than films on SrTiO3. Defects are known to act as recombination sites for charge carriers. The higher concentration of defects in the film on alumina could help explain the low activity of this film.

5.4   CONCLUSIONS

In summary, Fe2O3 films on SrTiO3 substrates show greatly enhanced reactivity when compared to films on Al2O3 substrates. The reactivities of SrTiO3 supported films are

also greater than the reactivity of bulk Fe_2O_3 samples. The results show that the visible light photochemical activity of hematite, α-Fe_2O_3, can be enhanced through the proper choice of substrate material. If polar terminations of the $SrTiO_3$(111) surface are responsible for the increased reactivity, then the enhanced reactivity of the heterostructure should not occur on nonpolar substrate orientations. For example, the $SrTiO_3$(100) surface is nonpolar and does not have charged domains or spatially selective reactivity.[29] Results of photochemical activity of Fe_2O_3 films on polycrystalline perovskite substrates are included later in this document.

Chapter 6

Hematite Film Reactivity on Polycrystalline Substrates

This chapter reports on the photochemical activity of the hematite films supported on polycrystalline SrTiO₃ substrates.* The area examined for reactivity experiments was the same area used to determine the orientation relationships, discussed later in Chapter 8. After reaction with the silver nitrate solution, the reactivity of film grains was correlated to substrate and film reactivity. The films on polycrystalline substrates present a much wider array of orientation conditions when compared to films on single crystal substrates. This allows for the study of the interaction between film orientation and the substrate effects observed in Chapter 7.

6.1   EXPERIMENTAL DETAILS

The photochemical activity of Fe_2O_3 films grown on polycrystalline SrTiO₃ substrates is reported in this chapter. An analysis of film growth and orientation relationships is reported later in Chapter 8. Details on film growth can be found in § 8.1 (p. 69). Electron backscatter diffraction (EBSD) data from Figure 8.1 was used to correlate reactivity with orientation. Details for data collection can be found in § 8.1 (p. 69). Before the removal of the film to analyze substrate grain orientations, the photochemical marker reaction was performed on the film and analyzed using optical and atomic force microscopy (AFM). Marker reactions were performed as described in § 3.2 (p. 25). The light source was a blue LED, and the reaction time was one minute. This time was selected after trials with reaction times, and was found to result in some grains that were bare, while other grains were highly reactive. Longer reaction times resulted in the entire surface

---

*Originally, films on polycrystalline BaTiO₃ substrates were examined. After discussions with the thesis committee, work on polycrystalline substrates was repeated on SrTiO₃ substrates. The original results for films on BaTiO₃ substrates are presented in the appendix to this document.

FIGURE 6.1: Surface of Fe2O3 film on polycrystalline SrTiO3 substrate after marker reaction. Areas of dark contrast correspond to portions of the surface covered with a large amount of reaction product. Bright areas are bare areas, with little reaction product. The outlined boxes correspond to the areas presented in the AFM micrographs in Figure 6.6.

FIGURE 6.2: Surface of Fe2O3 film on polycrystalline SrTiO3 substrate after cleaning. The surface shows uniform contrast, exception pores, cracks, and the affect of light polarization, supporting the interpretation of contrast in Figure 6.1.

covered in reaction product. After these longer reaction times, silver colored material visibly coated the reaction surface, without the aid of microscope analysis. Because the light source was the LED, only visible light was available to excite electrons to the conduction band. Because the band gap of SrTiO3 requires ultraviolet light to generate charge carriers, all photochemical activity was attributed to the film. It was assumed that a negligible number of charge carriers were generated in the substrate.

6.2   RESULTS

After reaction with the silver nitrate solution, the film was examined using optical and atomic force microscopy. Optical microscopy provided a rapid, high throughput classification of the entire area. AFM then confirmed the interpretation of the optical micrograph, and provided a detailed look at small subsections of the examined area.

Optical Microscopy

Figure 6.1 shows an optical micrograph of an area of the sample surface after reaction. Dark areas on the micrograph generally indicate areas with a large amount of reaction product. Pores are also responsible for some areas of dark contrast. Any pores could be identified by comparison with an image of the clean sample surface. The image of the clean surface also served as a reference, verifying that dark contrast was not present. The clean surface is uniformly bright, with the exception of pores, cracks, and grain boundaries. These areas appear as dark spots on the micrograph. Some grains appear slightly darker than others. This is a result of differing interaction with the polarized light, and does not represent reaction product on the surface. Figure 6.2 shows the surface after reaction product was cleaned, for comparison with the image in Figure 6.1.

Using the electron backscatter diffraction maps in Figure 8.1 as a guide, each individual film grain was identified in the optical image in Figure 6.1. The identified grains

FIGURE 6.3: Grain boundary network taken from EBSD data in Figure 8.1(b) with assignments of reactivity observed in Figure 6.2. Dark blue represents highly reactive grains, medium blue represents moderately reactive grains, and light blue represents nonreactive grains. White grains are those that were not assigned a reactivity level.

FIGURE 6.4: Standard cubic stereographic triangle showing the orientation of substrate grains classified in Figure 6.3. Dark points are highly reactive grains, light points are moderately reactive grains, and empty points are nonreactive grains.

were manually classified as highly reactive, moderately reactive, or nonreactive. Grains that were uniformly dark were classified as highly reactive. Conversely, grains that were uniformly bright were nonreactive. Grains that appeared a medium gray color, or were otherwise not uniformly covered by reaction product were labelled moderately reactive.

Figure 6.3 shows a digram of the resulting classifications. The grain boundaries were taken from the EBSD map of the substrate. Dark blue portions of this map correspond to highly reactive grains, medium blue to moderately reactive grains, and light blue areas are nonreactive grains. White corresponds to areas where no assignment was made. This occurred when it was unclear the reactivity level of a grain, owing to image artifacts or difficulty distinguishing grains. Also, some white grains in Figure 6.3 were outside the field of view of the microscope image in Figure 6.2.

The orientation of the substrate and film grains was plotted on the standard stereographic triangles for cubic and hexagonal crystal structures respectively. These plots are depicted in Figure 6.4 and 6.5. Both film and substrate orientations were examined to determine whether any reactivity differences were a result of substrate or film orientation alone, or a combination of the two.

In the plot of the substrate grains in Figure 6.4, highly reactive grains are represented by dark points, moderately reactive grains by light points, and nonreactive grains by empty points. The figure doesn't show a strong relation between substrate orientation and grain reactivity. Highly reactive and moderately reactive points are spread throughout the standard stereographic triangle. Nonreactive grains are weakly clustered near the (111) orientation and along the axis between the (001) and (101) orientations.

The reactivity of the film grains are plotted on the three hexagonal triangles in Figure 6.5. The points are plotted in separate triangles to better illustrate trends in the data. Because of the large number of film grains, with each substrate grain supporting

2

FIGURE 6.5: Standard stereographic triangles showing the orientation of (a) highly reactive (dark points), (b) moderately reactive (light points), and (c) nonreactive grains (empty points).

FIGURE 6.6: Representative AFM images of the film surface after reaction, showing highly reactive and nonreactive grains. The areas corresponding to these micrographs are outlined in Figure 6.1.

multiple film grains,[†] plotting all data on the same triangle obscures analysis. When all points are on the same triangle, it becomes difficult to observe individual points. The range of orientations contained in this film does not cover the entire stereographic triangle. Figure 6.5 shows the entire range of orientations for the film grains on this sample. Grains that were labeled moderately reactive are scattered throughout the entire orientation spread. No clear orientation preference is observed. When examining the plots for highly reactive and nonreactive grains, the situation becomes more complicated. Highly reactive grains are clustered along axis between the (0001) and $(1\bar{2}13)$ orientations. Conversely, nonreactive grains are clustered near the (0001) orientation and near the axis between $(0\bar{1}12)/(10\bar{1}2)$ orientations. This suggests an orientation preference for Fe_2O_3 films on polycrystalline $SrTiO_3$ substrates. This is discussed further in Section 6.3.

Atomic Force Microscopy

After optical microscopy, AFM was then used to confirm the interpretation of the optical image. Five individual areas of the sample surface were scanned, each comprising multiple substrate grains. These areas were selected to contain all reactivity classes and a variety of substrate orientations. Representative AFM micrographs of the examined areas are shown in Figure 6.6. Reaction product appears as bright contrast in the AFM images. Varying levels of reactivity are seen in each of the micrographs. In Figure 6.6(a), grains identified as highly reactive are outlined.

The AFM micrographs verify the interpretation of the optical images. Grains that were dark on the optical micrograph were the grains with the largest amount of silver product on the surface. Grains that were bright on the optical image had the least amount of reaction product. These results verify the broader but less detailed results from the optical micrograph, and give increased reliability to the reactivity assignments in Figure 6.3. AFM analysis did not show a difference in roughness between grains to account for the order of magnitude reactivity difference observed in these results.

6.3   DISCUSSION

Overall, the film is more reactive than the bulk hematite. Grains with orientations that demonstrated low reactivity in the bulk were highly reactive in the film. For similar

---

[†]For more information on film growth, see Chapter 8 (p. 69).

reaction times, the film showed more reactive grains than the bulk, as well as more reaction product on the surface. Especially considering that the film is only 50 nm thick, and so is only absorbing a small portion of the incident light before the interface with the substrate,[‡] the film exhibits high reactivity when compared to bulk Fe_2O_3. Once again, the $SrTiO_3$ substrate improves the photochemical activity of hematite films when compared to the bulk material.

The observed trends in photochemical reactivity in this chapter represent combined effects from Fe_2O_3 orientation and substrate/film interaction, each presented the previous to chapters. In Chapter 4, it was observed that Fe_2O_3 reactivity is highly anisotropic, with c-axis oriented crystallites showing low reactivity. Conversely, the c-axis oriented films on $SrTiO_3$ substrates presented in Chapter 5 were highly reactive. The films on polycrystalline substrates observed here expose varying film orientations while retaining the orientation relationship between film and substrate observed for the films in Chapter 5.[§]

The optical micrograph presented in Figure 6.1 shows clear signs of reactivity differences between grains. Some grains are dark, completely covered in silver reaction product. Other grains are completely devoid of reaction product. The boundaries between areas of high reactivity and low reactivity correlate with EBSD maps of the substrate grains. Qualitatively, the Fe_2O_3 film on the $SrTiO_3$ substrate is overall significantly more reactive than the polycrystalline sample discussed in Chapter 4.

The results presented in Figures 6.4 and 6.5 suggest that while the film orientation has an effect on reactivity, the substrate orientation does not. Only the mild clustering of non reactive grains found along the axis between (001) and (101) oriented grains suggests any direct affect of substrate orientation on reactivity. On the other hand, the plots for highly reactive, moderately reactive, and nonreactive films differ from each other. Highly reactive grains are clustered along the center of the standard stereographic triangle, along the axis between (0001) and ($1\bar{2}10$). Areas along the edge of the triangle, located at orientations between (0001) and ($10\bar{1}0$) do have few active grains. The reverse distribution is seen for the nonreactive grains. Nonreactive grains are clustered near the (0001) orientation, and along the axes between (0001) and ($0\bar{1}10$)/($10\bar{1}0$). Grains described as moderately reactive were spread over the entire space of film orientations.

The results here show similar trends to the anisotropic behavior of bulk hematite crystallites.[¶] It is shown in this document that bulk Fe_2O_3 grains located near the ($1\bar{2}10$) orientation are the most reactive. Grains far away from this orientation exhibited negligible reactivity. This includes (0001) (c-axis) oriented grains, and also grains at any degree of tilt away from (0001) orientation with the [$10\bar{1}0$] direction located out of the sample plane.

[‡]The penetration depth of the light in this experiment (λ= 470nm), reported in Section 5.3, is ~450 nm, significantly larger than the thickness of the film in this experiment.

[§]A complete description of the orientation relationship for Fe_2O_3 films on polycrystalline $SrTiO_3$ substrates can be found in Chapter 8 (p. 69).

[¶]The discussion in this chapter is a brief overview of the results for photochemical activity of bulk hematite polycrystals. See Chapter 4 (p. 33) for a detailed description of the results of this experiment.

For bulk hematite, the grains that were the most reactive were located relatively near to to the ($1\bar{2}10$) orientation. The reactive grains in Figure 6.5(a) are tilted considerably closer to (0001) than any of the reactive grains in that study. However, the results here do follow the general trend observed for that work; hematite grains become reactive as they tilt away from the (0001) orientation, *so long as the [$1\bar{2}10$] direction is pointing out of the surface.* In other words, if the axis of rotation away from (0001) is a [$10\bar{1}0$] direction, the [$1\bar{2}10$] direction will be pointing out of the surface, and the grain is likely to be reactive.‖ If the tilt axis is the [$1\bar{2}10$] direction, the grain is not likely to be reactive, as the orientation will lie along the nonreactive region between (0001) and ($10\bar{1}0$). The results for the film materials show the same trend, however the film becomes reactive and a much lower tilt away from (0001). Compare the distribution of reactive grains in Figure 6.5 to the distribution in Figures 4.3 or 4.6 in Chapter 4. It is important to note that the higher symmetry of the cubic substrate limits the range of possible orientations for the hexagonal film. The most highly reactive bulk orientations are not present in this film, and yet many film grains are highly reactive.

For the films on single crystal substrates in Chapter 5, (0001)-oriented films on (111)-oriented substrates were highly reactive. Here, many grains close to this substrate orientation were marked as nonreactive or moderately reactive. The contradictory results can be understood through the anisotropic reactivity of hematite. For all Fe_2O_3 films on $SrTiO_3$ substrates, the reactivity of the film was improved compared to the bulk material. When grown on single crystal substrates, the only film orientation observed is (0001) basal plane oriented Fe_2O_3. This orientation is nonreactive for bulk crystals. When films are grown on polycrystalline substrates, more reactive Fe_2O_3 orientations are exposed to the surface. If single crystal substrates existed that could be used to stabilize the reactive faces of Fe_2O_3, it is expected that those films would be even more reactive than the films in the previous chapter. However, the low-index orientations available for $SrTiO_3$ substrates do not stabilize such films. The results in this chapter suggest that the anisotropic reactivity of Fe_2O_3 persists, but is less severe as a result of substrate/film interactions.

An interesting phenomenon observed for this experiment is that reactivity in some cases appears to be different between film grains on the same substrate. One set of grains is sometimes more reactive than the other. Reactivity following the lamellar structure of the film grains is observed in multiple instances in Figure 6.1. These cases were generally those of moderate reactivity, and all film grains on that substrate grain were plotted as mildly reactive in Figure 6.5. It may be that further refinement in the orientation depends of hematite reactivity could be observed through an analysis of these grains. However the detail of the optical image was not sufficient to accurately determine which grains followed this reactivity pattern. Additionally, Figure 6.3 suggests that grains with similar levels of reactivity are clustered near each other. The highly

---

‖Figure 4.9 (p. 39) provides a helpful schematic of the relative orientation of the [$10\bar{1}0$] and [$1\bar{2}10$] directions and planes in the hematite crystal system.

reactive grains are all located near each other, as are many of the nonreactive grains. This could suggest that the high reactivity on some parts of the sample is not directly related to individual crystallite orientation. However, the boundaries between highly active grains and nonreactive grains do sharply follow the grain boundaries identified using EBSD. The results presented in this document do not entirely support the assertion that another affect could be responsible for the high reactivity and resulting clustering of reactive grains. However, the clear demarcation in reactivity across grain boundaries suggest that there is some effect related to individual crystallite properties.

6.4 CONCLUSIONS

Hematite films on polycrystalline substrates showed clear signs of reactivity differences between grains. Substrate orientation does not appear to drive this reactivity difference, except in that it also is responsible for resulting film orientation. The film orientation shows a correlation between orientation and high and low reactivity. Highly reactive grains were found in the region between (0001) and ($1\bar{2}13$) on the standard stereographic triangle. Nonreactive grains were clustered near (0001) and in the region between (0001) and ($10\bar{1}2$)/($01\bar{1}2$). This pattern is similar to the orientation dependent reactivity observed in Chapter 4. Additionally, the film on average was significantly more reactive than bulk hematite.

PART III

EXPERIMENTS ON FILM GROWTH

Chapter 7

Hematite Film Growth on Single Crystal Substrates

This section describes the results for studies of Fe_2O_3 film growth on single crystal substrates. Film orientation and phase determination was carried out using electron backscatter diffraction analysis and x-ray diffraction. Films were grown on Al_2O_3 (0001), $SrTiO_3$ (111), and $SrTiO_3$ (001) substrates. The films were epitaxial on Al_2O_3 and $SrTiO_3$ (111). The films on $SrTiO_3$ (001) were polycrystalline, but show significant texture. Film grains on these substrates fall into five distinct groupings. The orientation relationship between substrate and film for each orientation group was determined.

7.1 FILM GROWTH ON STRONTIUM TITANATE (111) SUBSTRATES

Figure 7.1 shows EBSD maps of a film grown on $SrTiO_3$ (111) substrate. Figure 7.1(a) is a phase map of all recorded points in the scan. During the automated scan, the EBSD software was allowed to assign either magnetite or hematite phase for each recorded pattern. In this map, points indexed as hematite phase appear red, while points indexed as magnetite are green. The red points (hematite) comprise 97.5 percent of the total data, while only 2.5 percent of points were indexed as magnetite (green). Additionally, the points indexed as magnetite don't appear in any perceivable pattern. Instead, they appear to be distributed randomly over the scan area. These two facts together suggest that the magnetite points can be attributed to errors in the EBSD process, such as poor pattern quality, surface contamination, or areas of poor film quality, such as the

FIGURE 7.1: (a) EBSD phase map for an Fe_2O_3 film on $SrTiO_3$ (111). Red points represent hematite grains and green points represent magnetite. (b) An inverse pole map of the same area of the sample, showing only hematite grains. (c) The selection of points used for the generation of pole figures.

FIGURE 7.2: Pole figures for the data represented in Figure 7.1. (a) (0001) reflection showing c-axis out of plane. (b) (10$\bar{1}$0) reflection showing 6-fold symmetry in the plane. (c) (1$\bar{2}$10) reflection showing 6-fold symmetry in the plane.

macroscopic particles resulting from the pulsed laser deposition process. Within the experimental limit, the film is considered to be comprised of solely hematite phase.

Figure 7.1(b) depicts an inverse pole map of the same dataset, with the exception that all magnetite points (green in Figure 7.1(a)) have been removed from the set. An inverse pole map depicts the crystallographic direction normal to the sample surface at each measured point. A color gradient is assigned to the stereographic unit triangle, which through symmetry represents all possible surface orientations for a given crystal system. Each point in the inverse pole map is colored according to its surface normal's position in the crystallographic triangle. A point with a surface normal of (0001) would appear as red on this map, while a point with (1$\bar{1}$00) appears as blue. The majority of points in this scan lie near the (0001) orientation, appearing red on the map. The remaining points are randomly distributed across the surface and in orientation space. As a result, the same factors that result in magnetite points are assumed to be responsible for these points on the inverse pole map. Even if this attribution is incorrect, and small portions of magnetite phase or non-epitaxial hematite exist in the film, a large majority of the points were indexed as hematite. Further optimization of the deposition parameters could improve film quality and reduce these undesired portions. Figure 7.1(c) depicts in inverse pole map containing only the points within 15° the (0001) orientation. This data was used to generate the following pole figures for analysis of film/substrate orientation relationships.

Pole figures represent a distribution of specific crystal orientations in the reference frame of the sample. The center of the pole figure represents the direction normal to the sample surface. Points on the edges are directions in the plane of the sample. A crystallographic plane is chosen, and the distribution of that direction in space is plotted on the pole figure. A color gradient is used to depict which directions in the sample reference frame that crystallographic plane normal is most prevalent. For the data plotted in Figure 7.2, red represents sample directions with high population of the chosen crystal orientation. Blue represents sample directions with a low population. Units on pole figures are multiples of random density (MRD), representing the texture of the examined sample compared to that of an untextured sample. These pole figures allow for the examination of both in plane and out of plane crystal orientation relationships. For all pole figures presented in this document, texture calculations were performed using the built in discrete binning method with a bin size of 5.0°.

Figure 7.2(a) is the pole figure for the (0001) plane (the hexagonal c-axis). As might be guessed from the inverse pole maps, the (0001) zone is only found directly out of plane of the sample. From this, the out of plane orientation can be determined to be $Fe_2O_3(0001)||SrTiO_3(111)$. Figures 7.2(b) and 7.2(c) are pole figure for (10$\bar{1}$0) and (1$\bar{2}$10) planes (prismatic directions in the hexagonal unit cell, orthogonal to the c-axis). These

FIGURE 7.3: X-ray diffraction pattern for Fe_2O_3 film grown on $SrTiO_3$ (001) substrate. Points marked with a blue square are substrate peaks. Points marked with a red circle are film peaks.

FIGURE 7.4: Inverse pole EBSD map of an Fe_2O_3 film on $SrTiO_3$ (001) substrate. Five distinct color bins, labeled red, purple, white, cyan, and yellow, are observed.

pole figures show that the prismatic directions are parallel to the sample surface. They also show 6-fold symmetry. This suggests that the in a-axis directions are preferentially lining up with specific substrate directions. In this work, the orientation of the sample in the EBSD chamber was not tracked. It is not known which direction the $<1\bar{1}0>$ substrate directions lie in the sample reference frame. The 6-fold symmetry suggests the $<1\bar{1}0>$ family of substrate directions as a likely candidate for determining the in plane orientation of the Fe_2O_3 film. The set of substrate $<1\bar{1}0>$ directions that lie in the (111) plane shows 6-fold symmetry around the [111] direction. A comparison of the lattice parameters for the film and substrate gives further support to this hypothesis. The lattice parameter for the a-axis of Fe_2O_3 is 5.035 Å. The length of the $<1\bar{1}0>$ direction in the cubic substrate is 5.225 Å. This gives a lattice mismatch of 3.8%. From this analysis, it is proposed that the in-plane orientation relationship for Fe_2O_3 films on $SrTiO_3$ (111) substrates is $Fe_2O_3[100]||SrTiO_3[1\bar{1}0]$.

The pole figures presented in Figure 7.2 have allowed for the determination of the orientation relationship for epitaxial films of Fe_2O_3 on $SrTiO_3$ substrates. It is determined that for the out of plane relationship, $Fe_2O_3(0001)||SrTiO_3(111)$. For the in plane relationship, $Fe_2O_3[100]||SrTiO_3[1\bar{1}0]$.

7.2 FILM GROWTH ON STRONTIUM TITANATE (001) SUBSTRATES

EBSD *Mapping*

Fe_2O_3 film growth on $SrTiO_3(001)$ substrates is significantly more complicated than growth on $SrTiO_3(111)$ substrates. X-ray diffraction immediately shows that films on $SrTiO_3(001)$ are not singly-textured. Multiple film peaks appear in the θ-2θ scan of the Fe_2O_3 film on $SrTiO_3(001)$ shown in Figure 7.3. After initial X-ray analysis, the film was examined using electron backscatter diffraction. Figure 7.4 shows an inverse pole map of the as EBSD data. While scanning the film, the EBSD software was once again allowed to index each film point as either hematite, magnetite, or strontium titanate. The map in Figure 7.4 only shows points indexed as hematite. Points indexed as either of the other two possible phases appear black on the map. It is noted that the majority of the points in the scan area indexed as hematite, indicating that the film was hematite

	Number of Points	Area Fraction
Red	45,072	0.105
Cyan	37,497	0.088
Purple	55,640	0.130
White	103,881	0.244
Yellow	14,914	0.035
ALL DATA	425,917	1.000

TABLE 7.1: Summary of the area fraction of points falling into the five color bins from the map in Figure 7.4. The total number of points falling into one of the five color bins is 257,004, representing a 60.4% fraction of the total number of points.

FIGURE 7.5: Inverse pole figure of the entire dataset represented in Figure 7.4.

phase Fe_2O_3, and that the collected diffraction patterns were from the film, not the substrate. It is apparent that the texture of the film on $SrTiO_3(001)$ is not random. The inverse pole map shows grains falling into five distinct color bins. These bins will be referred to as red, cyan, purple, white, and yellow. Table 7.1 lists the fraction of points in the scan that make up each color bin.

The fractions do not add up to 1, as the color bins do not include any of the black points in the map, nor the points on the map falling outside these color bins. When the entire scan area is shown, outlying points are not visible on the map. When zoomed in, individual outlier points are clearly visible, and account for the points not used in calculating the following pole figures. The total area fraction represented on this map represents a majority (60.4%) of the collected points. This proportion of points is similar to the number of points obtained if the entire dataset is partitioned to only include points with a confidence index greater than 0.1 (compared to a mean value of 0.18). That partition includes all the color bins here, though it is important to note that partitioning via confidence index was not used to create the actual datasets. It is pointed out only to support that the population of points used in the following calculations likely correspond to high quality measurements.

Figure 7.5 is an inverse pole figure of the points on the map in Figure 7.4. Similar to the pole figures presented earlier, inverse pole shows the distribution of crystallographic directions normal to the sample surface in the crystal reference frame. While the pole figure shows the distribution of a given crystallographic direction in the sample reference frame, the inverse pole figure shows the distribution of all crystallographic directions in a given sample direction. In this case, the figure shows the distribution of crystallographic directions that lie in the sample normal direction. Once again, red represents areas of high population, while blue represents areas of low population. Five distinct maxima are observed, correlating with each of the colors observed on the

	Orientation
Red	(0001)
Cyan	$(1\bar{2}10)$
Purple	$(10\bar{1}2)$
White	$(1\bar{2}13)$
Yellow	$(0\bar{1}14)$

TABLE 7.2: Miller indices for the orientation represented by each of the color bins seen in the inverse pole map in Figure 7.4.

FIGURE 7.6: Pole figure maps representing the five data partitions used for texture analysis. Each map is a subset of the data presented in Figure 7.4.

inverse pole map. Each maximum occurs at a low index plane. Table 7.2 summarizes the crystal direction corresponding to each color bin. These zones represent the planes that will be analyzed using pole figures.

The data was manually partitioned into subsets corresponding to each color bin. This allows for texture analysis of each set of orientations independent of the other sets. This is a distinct advantage of using the EBSD technique over x-ray diffraction pole figure analysis. Unlike X-ray diffraction, which examines the entire scan area simultaneously, EBSD ties each piece of orientation data back to a location on the sample. After measurement, data can be partitioned and manipulated; subsets of data can be extracted for further analysis. Data partitioning was performed by clicking on a point on the map, after which the software highlights all points within a specific tolerance angle (typically 15°). Additional points were clicked until all points within a specific color bin were highlighted, as determined by manual inspection. Once all points of a specific color were highlighted, the data was extracted into a new dataset.

Figure 7.6 shows the resulting inverse pole maps from this procedure. The spacial distribution of the color bins across the scan area is nonuniform. Portions of the scan area have a much higher distribution of grains of a certain orientation. For example, the upper left and upper right portions of the scan area show a much higher percentage of grains colored purple or white. At this point, it is unknown why the distribution between the observed orientation groups is not homogeneous across the scan surface. Possible explanations could include local temperature differences, surface roughness differences (increased or decreased step concentration), or surface impurities. Each of these factors could lead to different surface diffusion and nucleation rates, causing differing nucleation and growth rates than for other areas of the sample, which in turn affects orientation preferences.

FIGURE 7.7: (a) Inverse pole figure for the data in the red partition. (b) Pole figure for the (0001) reflection of the red partition.

FIGURE 7.8: Pole figures for the prismatic reflections showing 12-fold symmetry in the plane of the sample.

Pole Figure Analysis

From the previous section, there are five distinct orientation relationships to determine. The partitioned data was used to determine what these relationships are for each set of grains. Pole figures were then generated for each of the datasets. The following is an analysis of each set of pole figures. Unlike for the data presented for growth on $SrTiO_3(111)$ substrates, in this case the substrate crystal directions and sample orientation in the microscope were tracked. For all of the following pole figures, the x- and y-axes represent the substrate (100) and (010) directions, and the substrate (001) is normal to the plane of the figure.

Red Partition

The partition colored red on the inverse pole map represents film grains with a c-axis orientation. This is reflected in the inverse pole figure and (0001) pole figure found in Figure 7.7. This pole figure verifies that the (0001) zone is orthogonal to the sample surface. Both of these planes are perpendicular to the c-axis, and are expected to have plane normals parallel to the sample surface. The pole figures in Figure 7.8 verify this to be the case. Both pole figures show 12-fold symmetry, with maxima occurring at the edge of the pole figure at regular 30° intervals. Four of the maxima occur in alignment along the substrate <110> direction. This is consistent with the previously observed in plane orientation relationships for growth on $SrTiO_3(111)$ substrates. The $SrTiO_3$ [110] lattice distance shows 3.8% mismatch with the Fe_2O_3 a-axis lattice parameter. The ($10\bar{1}0$), ($1\bar{1}00$), ($01\bar{1}0$) are all crystallographically equivalent planes, separated by 60°. Alignment of three equivalent film directions along four possible <110> substrate directions gives rise to the twelve fold symmetry seen in the pole figure. The same logic extends to the ($1\bar{2}10$) pole figure. For this partition, the orientation relationships can be defined as $Fe_2O_3(0001)||SrTiO_3(001)$ and $Fe_2O_3(10\bar{1}0)||SrTiO_3(110)$. Equivalent prismatic planes in the Fe_2O_3 crystal structure give rise to the 12-fold symmetry observed for the ($10\bar{1}0$) and ($1\bar{2}10$) pole figures. Each of the three equivalent <$10\bar{1}0$> directions aligns with one of the four substrate <110> directions. This combination results in the 12-fold symmetry.

FIGURE 7.9: (a) Inverse pole figure for the cyan partition, representing grains with a $(1\bar{2}10)$ orientation. (b) Pole figure for the (0001) reflection of the cyan partition. (c) $(1\bar{2}10)$ pole figure for the cyan partition. The four maxima near the substrate <111> directions were unexpected, based on the inverse pole figure.

FIGURE 7.10: Inverse pole figures showing (a) the $(1\bar{1}02)$ orientation of the purple grains and (b) the $(1\bar{2}13)$ orientation of the white grains.

Cyan Partition

This partition represents grains near the $(1\bar{2}10)$ orientation, as shown in the inverse pole figure depicted in Figure 7.9(a). The hexagonal unit cell is aligned with its c-axis in the plane of the sample surface. The pole figure for the (0001) plane in Figure 7.9(b) demonstrates this alignment. It shows that the (0001) zone lies in plane, with maxima along the <110> directions, and secondary maxima spaced at 30 degree intervals. These secondary maxima are much less intense than those along the <110> directions, roughly 3-4 MRD compared to a maximum of 12 for the main peaks. Given that this partition represents points with the $(1\bar{2}10)$ zone out of the surface, it is expected that the pole figure for the $(1\bar{2}10)$ reflection would show a single maximum at the center of the pole figure. The actual pole figure, shown in Figure 7.9(c), is slightly more complicated. As expected, the most prevalent orientation for the $(1\bar{2}10)$ zone in this partition is directly out of the plane of the sample. However four secondary maxima are observed, aligned along the <111> substrate directions, tilted 57° away from the sample normal direction. This orientation is explored in more detail for the purple and white partitions, which both share this alignment of the film c-axis with a substrate <111> direction. The reasons for the c-axis alignment along the (110) direction, and for the $(1\bar{2}10)$ peaks along the substrate (111) directions are not yet understood. It is possible that during the binning of the original dataset, a certain subset of points falling between the white bin and the cyan bin were included in the latter group, resulting in the secondary peaks shown here. The orientation relationships are $Fe_2O_3(0001)\|SrTiO_3(110)$ and $Fe_2O_3(1\bar{2}10)\|SrTiO_3(001)$.

Purple and White Partitions

The white and purple partitions represent the most interesting orientation relationship between the film grains and the substrate. These partitions represent grains with $(1\bar{1}02)$ and $(1\bar{2}13)$ orientations respectively. Inverse pole figures verifying these orientations are shown in Figure 7.10. The inverse pole figures suggest that both of these orientations represent grains that have a c-axis tilted roughly the same angle away from normal to the sample surface. The surface orientation differs by a rotation around this tilted c-axis. Pole figures for the (0001) planes for these partitions are shown in Figure 7.11. Both pole figures show the same orientation preference for the (0001) reflection. Four maxima

FIGURE 7.11: Pole figures for the (0001) reflection for the purple partition (a) and the white partition (b). The (0001) zone is located directly in line with the substrate <111> directions.

FIGURE 7.12: Pole figure for the prismatic zones of the white and purple partitions. These pole figures suggest a three fold rotation around the film c-axis (which is aligned along the substrate [111] direction, as seen in Figure 7.11).

are observed, located 57-60° from the center of the pole figure. The four maxima are observed in line with the (111) cubic substrate directions. The substrate (111) direction is located 54.7° away from the out of plane (001) direction. The angle between the (0001) and ($1\bar{1}02$) planes for the Fe_2O_3 film is 57.6°, and the angle between the (0001) and ($1\bar{2}13$) directions is 61°. If the orientation relationship for these film grains and the substrate is driven by the alignment of the substrate (111) direction with the film (0001) direction, this would lead to ($1\bar{2}13$) and ($1\bar{1}02$) planes parallel to the sample surface, as observed in the inverse pole figure.

For these grains, the orientation relationship can be summarized with the relation $Fe_2O_3(0001)||SrTiO_3(111)$. This is the same relationship determined for films on Sr-TiO3(111) substrates. However in that case, the (111) direction was directly out of the plane of the sample, and an in plane direction with low lattice mismatch was identified to explain the in plane alignment. In this case, the 2-D lattice parameters at the sample surface don't appear to be the driving force for the film's orientation relationship. Instead, substrate directions drive the relationship. More vectors than just the substrate and film normal and in plane directions must be taken into account to predict the structure of the film. The same epitaxial relationship of the film c-axis aligning with the substrate (111) direction, even when that substrate direction is tilted to high angles away from the surface.

In some ways, this is similar to the idea of axiotaxial film growth. Axiotaxy is defined as a fiber-like film growth mode, with a film direction aligning along a substrate direction, though not necessarily the substrate direction orthogonal to the substrate surface. In both axiotaxy and the purple and white partitions of the films reported here, crystal directions appear as the dominant driver of orientation relationship, rather than lattice match between the substrate and the film. However, axiotaxial growth exhibits a rotational degree of freedom around the film growth axis. If these partitions showed true axiotaxial growth, the pole figures for the prismatic planes of the film would be expected to show circular patterns around the rotation axis. This is not the case. Figure 7.12 shows pole figures for the prismatic ($1\bar{2}10$) and ($10\bar{1}0$) planes. Instead of circular bands, these faces demonstrate 3-fold symmetry when rotated around the film (0001) direction. In the case of the white partition, the ($10\bar{1}0$) film direction appears to line up with the substrate (110) directions. For the purple partition, the substrate (110) direction lines up with the film ($1\bar{2}10$) direction. The maxima along the rolling direction (RD) and the transverse direction (TD) in these pole figures are located 45° away from

FIGURE 7.13: Inverse pole figure showing the $(01\bar{1}4)$ orientation of yellow grains.

FIGURE 7.14: Pole figure for the $(01\bar{1}4)$ reflection of the $(01\bar{1}4)$-oriented yellow partition.

the center of the figure. This supports the idea that these maxima are in line with the (011) directions.

For all data represented in these pole figures, the orientation relation $Fe_2O_3(0001)\|SrTiO_3(111)$ holds true. For the white partition, that is, grains with the direction normal to the film $(1\bar{2}13)$ plane normal to the surface, the $(10\bar{1}0)$ planes are in line with the substrate (110) planes. For the purple partition, grains with a $(1\bar{1}02)$ orientation, the $(1\bar{2}10)$ planes are in line with the substrate (110) planes.

Yellow Partition

The final partition of this dataset is not yet understood. The yellow partition represents a significantly smaller portion of the original scan than the other datasets, and doesn't lend itself to easy interpretation either through lattice mismatch or an analysis of c-axis tilt angles, as were used for previous orientation relationship determination. This partition represents $(01\bar{1}4)$ oriented grains, as determined from the inverse pole figure and $(01\bar{1}4)$ pole figure shown in Figures 7.13 and 7.14.

Figure 7.15 shows a pole figure for the (0001) plane. The maxima for this pole figure are less easily understood. The pole doesn't show the same qualities seen in the previous figures; the (0001) zone isn't located in alignment with easily identified low-index substrate directions, and doesn't show the 4-fold or 12-fold symmetry seen in previous cases. The maxima in the southern hemisphere of the pole figure do suggest the beginnings of twelve fold symmetry. The lack of highly evident maxima corresponding to the remaining points of the 12-fold rotation could be a result of the small size of this dataset. The low number of points could mean that this pole figure shows an incomplete picture, and more scan data would fill in the rest of the symmetry. Two peaks, colored red and located just below the horizontal axis, are significantly stronger than the remainder, and suggest a possible starting point for future examination. From the inverse pole figure in Figure 7.13, the orientation relationship between the substrate and film normal is $Fe_2O_3(01\bar{1}4)\|SrTiO_3(001)$. The in plane relationship is not yet determined. At this point no clear explanation for the nucleation of $(01\bar{1}4)$ oriented film grains has been discovered.

FIGURE 7.15: Pole figure for the (0001) reflection of the yellow partition.

Discussion

For each orientation group,[*] the orientation relationship was determined. In some cases the same alignment of a vector or plane was found, even though the out of plane orientation differed. For example, the cyan, white, and purple orientations all share the relationship $Fe_2O_3[10\bar{1}0]||SrTiO_3[1\bar{1}0]$. The purple and white orientations both have their (0001) planes parallel to the substrate (111) planes.

An interesting way to understand the observed epitaxial relationships is to consider the arrangement of close-packed (eutactic)[88] networks.[†] The hematite structure is a hexagonal close packed (hcp) network of oxygen atoms, with iron atoms filling ⅔ of the interstitial sites. The close packed oxygen plane is the (0001) plane, and the close packed direction within this plane is the <$1\bar{1}00$> family of directions. The $SrTiO_3$ substrate is a cubic close packed (ccp) network of SrO_3 atoms, with titanium atoms in ¼ of the octahedral interstitial sites. The close packed planes are the {111} family of planes, and the close packed directions within that plane are <$1\bar{1}0$>.

Each orientation group is represented by the alignment of one or both of the close packed plane or close packed direction between film and substrate. The white partition, oriented at ($1\bar{2}13$), represent grains with both the close packed planes and directions forming the orientation relationships. In this partition, the (0001) planes of the film is parallel to the substrate (111) planes. The film [$10\bar{1}0$] film direction is parallel to the substrate [$1\bar{1}0$] direction. This orientation represents a continuation of the eutactic network between the substrate and film.

Other partitions have at least one close packed alignment. The cyan orientation represents the alignment of the close packed directions. The red orientation also matches the close packed direction. The purple orientation shares the alignment of the close packed planes exhibited by the white partition, but the close packed directions are not aligned. Instead, the close packed direction of the film is rotated ~30° from the substrate close packed direction.

These results suggest that an analysis of the eutactic network can provide a useful guide for the prediction and analysis of film textures, especially in the case of heteroepitaxy with poor lattice parameter matching. In this case, it is difficult to find an arrangement for the hexagonal film that matches well with the cubic substrate. Instead, those close packed network suggests the alignments seen in these results.

---

[*]With the exception of the yellow grains, for which a clear orientation relationship could not be determined.

[†]Chapter 8 also discusses Fe_2O_3 thin film growth and the concept of eutactic arrangements in the context of growth on high index surfaces of polycrystalline substrates.

7.3 CONCLUSIONS

Hematite Fe_2O_3 films were grown on single crystal $SrTiO_3$ substrates. On (111) oriented substrates, the orientation relationships between film and substrates were determined to be $Fe_2O_3(0001)\|SrTiO_3(111)$ and $Fe_2O_3(10\bar{1}0)\|SrTiO_3(1\bar{1}0)$. Polycrystalline films grew on (001) oriented substrates. The film grains showed preferred orientations, falling into five orientation groups. A portion grains were (0001) oriented, a second group was oriented with the (0001) zone parallel to the sample surface, and a portion retained the $Fe_2O_3(0001)\|SrTiO_3(111)$ relationship, despite the (001) orientation of the substrate.

Chapter 8

Hematite Film Growth on Polycrystalline Substrates

This chapter presents results for the growth of Fe2O3 films on polycrystalline SrTiO3 substrates. Film growth on polycrystalline substrates allows for interesting, high throughput explorations of orientation effects on film growth and photochemical activity. The polycrystalline substrate exposes a much wider range of orientation conditions than are available for single crystal substrates. Additionally, a single film deposition results in thousands of individual orientation relationships. By using electron backscatter diffraction, local orientation relationships can be observed and determined.

8.1 FILM GROWTH AND ORIENTATION DATA COLLECTION

Following the deposition parameters in Section 3.1, a 50 nm film was deposited on a polycrystalline $SrTiO_3$ pellet. The substrate pellet was prepared as described in Section 3.1. The substrate was approximately 2 mm thick and 8 mm in diameter. Depositions parameters were as described in Table 3.2. After deposition, an area of the film was mapped using electron backscatter diffraction (EBSD). The film was polished away by hand using 0.3 μm colloidal silica. The film and substrate were easily differentiated, as the film was red and the substrate was tan. Polishing was stopped when no more red material was visible on the surface of the pellet, after ~30 s. The sample was returned to the SEM, and the same area of the surface was mapped. The relatively large size of the polishing abrasive used to remove the film reduced the pattern quality of the diffraction patterns, however image acquisition parameters could be adjusted to obtain sufficient image quality (IQ) and confidence index (CI) parameters. The data was processed with one iteration of a grain dilation algorithm, and subsequently assigning a single average orientation to each grain. In the grain dilation cleanup method, points not belonging to an already identified grain (based on misorientation angle and grain size) are changed to the orientation of the nearest grain. For this procedure, the minimum grain size was 5 pixels and the grain tolerance angle was 5°. The grain averaging procedure uses a

FIGURE 8.1: EBSD maps of the same area of a 50 nm Fe2O3 film on a polycrystalline SrTiO3 substrate. Outlined areas represent the same area of the sample.

FIGURE 8.2: High resolution EBSD detail showing the lamellar structure of Fe2O3 film grains within a single substrate grain.

tolerance angle to identify grains, and then assigns a single orientation to that grain, averaging the orientation of all points within the identified grain. The results of these two cleanup procedures are maps with clearly identified grains of a single orientation.

The substrate and film maps are shown in Figure 8.1. The map in Figure 8.1(a) is the film, while Figure 8.1(b) depicts the the same area of the substrate after film removal. The outlined regions in each map represents pairs of film and substrate grains. For most substrate grains, a similar clearly distinguishable set of film grains can be outlined, with borders matching the shape of the corresponding substrate grain. In general, each substrate grain nucleates a set of film grains, often corresponding to two distinct orientations. Even film grains that appear to be a single red color are actually multiple film grains, as determined by the EBSD software. These sets of film grains typically appear in lamellar formations, shown in the high resolution scan detail in Figure 8.2.

The colors used in inverse pole maps such as those presented in Figure 8.1 represent the orientation of each point on the map. The orientation assignment for each color is determined using the color filled standard stereographic triangle. The substrate map represents grains representing the entire color space of the key, suggesting a random arrangement of orientations. Conversely, the inverse pole figure for the film shows grains that are varying shades red, orange, pink, and yellow. These colors represent film grains located near the (0001) orientation, which is represented by solid red on the inverse pole maps. This suggests that the film grains are all nearer each other in orientation compared to the substrate. This doesn't take into account differences between the film and substrate phases when describing the orientation of their respective grains. Because of its higher symmetry, the entire range of orientations of the cubic substrate can be represented in a smaller standard stereographic triangle than the hexagonal film material. The angle between the red, (001)-oriented and blue, (111)-oriented substrate grains (the maximum misorientation for cubic crystals) is 54.7°. For the hexagonal Fe_2O_3, the angle between red grains and blue grains is 90°. Figure 8.3 shows the relationship of the cubic and hexagonal stereographic triangles to each other and the entire stereographic projection. The same color scale represents a wider set of orientations in the hexagonal system. As

FIGURE 8.3: Relationship of the standard stereographic triangles for hexagonal and cubic systems to each other and the complete stereographic projection.

FIGURE 8.4: Standard stereographic triangles representing the orientations of all grains in Figure 8.1. Each point on the triangles represents a grain used for orientation calculations. Shaded points in the hexagonal film triangle represent film grains with an outlier "out of plane" orientation relationship.

a result, a simple comparison of the color variance between these two images doesn't accurately reflect the differences in orientation spread for the two maps.

8.2 ORIENTATION RELATIONSHIP ANALYSIS

For Fe_2O_3 films on single crystal $SrTiO_3$ (001) substrates, the orientation relationship was $Fe_2O_3(0001)||SrTiO_3(111)$ for a significant portion of film grains (~90%), even though the $SrTiO_3$ (111) direction was not the out of plane direction. It was hypothesized that a similar relationship could be determined for the substrate grains tilted away from the (111) direction on the polycrystalline substrate. The $Fe_2O_3(0001)||SrTiO_3(111)$ orientation relationship would persist, even for grains tilted away from (111) orientation. To test this hypothesis, data from these maps was exported in the form of a text file containing a single line for each identified grain of the scan. Each grain was assigned a unique number ID. This ID was included, along with the Euler angles corresponding to the angle of that grain. The grain ID for each film grain was manually paired with the grain ID for its corresponding substrate grain. This was done through visible inspection of the maps depicted in Figure 8.1. Only film grains that could clearly be assigned to a substrate grain were included in the pairing list. Because multiple film grains exist on a single substrate grain, in many cases multiple pairings exist for a single substrate grain. A program was then used to calculate the minimum angle between a film direction and a substrate direction, taking into account symmetry operations for the film and substrate crystal structures.

117 such film/substrate pairs were analyzed to determine their orientation relationships. Because each substrate grain corresponds to multiple film grains, the 117 substrate grains represent 501 distinct film grains. Figure 8.4 shows standard stereographic triangles for the film and substrate, with each point within the triangles representing a substrate or film grain used for orientation relationship calculations. The substrate grains range widely over the entire area of the cubic standard stereographic triangle. The film grains are clustered near the (0001) point of the triangle. Once again, the same caveat as for the inverse pole maps comes into play. The angle between the (001) point and the edge for the cubic triangle ranges from 45° for the (101) corner and 54.7° for the (111) corner. Then angle between the (001) point and all edge points for the hexagonal triangle is 90°. The angular spread of the points represented in the film triangle is close to the same angular spread represented by the entire area of the cubic substrate triangle.

When the angle between the substrate [111] direction and the film [0001] direction is calculated for the 501 identified pairs in these scans, the average angle between the

Min	0.26
Q1	1.86
Median	2.77
Q3	3.64
Mean	4.22
Std. Dev.	6.50
Lower Fence	-3.46
Upper Fence	8.96

TABLE 8.1: Statistical descriptors of $Fe_2O_3[0001]/SrTiO_3[111]$ orientation relationship data.

FIGURE 8.5: Plot of the angle of misorientation between the film [0001] direction and the substrate [111] direction (out of plane, blue) and the film [10$\bar{1}$0] direction and substrate [1$\bar{1}$0] direction (red).

substrate [111] and the film [0001] is 4.22°. If outliers, defined as

$$\text{Lower Outlier} < \text{Lower Fence} = Q_1 - 3(Q_3 - Q_1) \qquad (8.1)$$
$$\text{Upper Outlier} > \text{Upper Fence} = Q_3 + 3(Q_3 - Q_1) \qquad (8.2)$$

where Q_1 is the lower quartile, Q_3 is the upper quartile, and $Q_3 - Q_1$ is the interquartile range, the average angle is 2.62°. Table 8.1 lists the statistical descriptors of the orientation relationship calculations. For the majority of substrate/film pairs, the film c-axis grew parallel to the substrate [111] direction, regardless of that direction's angle away from the surface normal. This orientation relationship is labeled as the "out of plane" relationship, mirroring the results for film growth on single crystal (111) oriented $SrTiO_3$ substrates.

The same orientation program was used to calculated the angle between the substrate [110] direction and the film [10$\bar{1}$0] direction. This proposed relation reflects observed alignment of the prismatic directions for films grown on single crystal substrates. The average angle between the calculated directions was 2.45°. By the same analogy to growth on $SrTiO_3$(111) substrates as for the Fe2O3[0001]||SrTiO3[111], this alignment of the film [10$\bar{1}$0] direction and the substrate [110] direction is labeled as the "in plane" relationship.

Figure 8.5 tabulates the results for the orientation relationship calculations including all calculations for both alignments, the "out of plane" Fe2O3[0001]||SrTiO3[111] and the "in plane" Fe2O3[10$\bar{1}$0]||SrTiO3[1$\bar{1}$0]. For each plot, the majority of calculated relationships fall within the calculated upper fence. In general, points that were outliers (beyond the upper fence) for the "out of plane" relationship were also outliers for the "in plane" relationship. It is important to note here that the description of these points as outliers does not imply an error in data collection, or that the values calculated for these points don't represent the actual orientation relationships. This is shown here for six example substrate grains, on which outlier film orientation were found. Each identified

Substrate ID	Film ID	$[0001]_{Film}/[111]_{Sub}$ (°)	$[10\bar{1}0]_{Film}/[110]_{Sub}$ (°)
652	645	37.59	18.39
	747	37.62	18.35
	764	37.88	18.16
804	914	32.45	25.11
	915	32.52	25.20
	1020	32.67	25.21
	922	32.73	25.22
828	1081	12.10	25.74
	1089	12.80	26.11
	1100	12.84	26.13
946	1409	33.78	8.59
	1422	38.32	16.55
	1393	38.43	12.53
	1395	39.41	12.75
1468	2044	19.73	20.29
	2058	19.79	20.48
	2175	19.84	20.60

TABLE 8.2: List of misorientation angles for grains that do not follow the observed orientation relationship between substrate and film.

film grain had consistent "out of plane" and "in plane" orientation relationships. These relationships are listed in Table 8.2. While within each grain, the orientation relationship is consistent, there is no single alignment that would describe all of these points. Three substrate grains promoted films with the c-axis angled 30-40°from the substrate [111] direction. Two additional grains prompted film grains with a ~12° misorientation and a ~20° misorientation. Similarly, the "in plane" orientation relations are generally consistent within each substrate grain, but no single orientation relationship describes all the outlier grains.

8.3 DISCUSSION

Similar to the previously discussed growth of polycrystalline Fe_2O_3 films on $SrTiO_3$ (001) substrates, the orientation relationship between the substrate and film is more complicated than the typical lattice parameter or interface plane view of epitaxy. A 2D description of the lattice matching wouldn't necessarily predict the consistent orientation relationship seen over a wide range of substrate orientations. Similarly, a description of the orientation relationship relying solely on out of plane and in plane vectors in the sample reference frame doesn't show the underlying consistent orientation relationship

for these films on polycrystalline substrates. If the conventional sample normal vector were to be used to describe each substrate grain orientation relationship, the result would be 117 different orientation relationship descriptions, rather than the one consistent descriptor from the lattice reference frame used here to describe the majority of film-substrate pairs.

Across wide ranges of substrate orientations, the orientation relationship of the film [0001] and [$10\bar{1}0$] directions aligned with the substrate [111] and [$1\bar{1}0$] directions respectively. This relationship matches that observed for films on (111)-oriented single crystal substrates, as well as for 2 of the observed classes of film grains on (001)-oriented single crystal substrates (the purple and white partitions reported in § 7.2 (p. 63).) Based on single crystal substrate results, grains oriented very near the (111) orientation would be expected to show this relationship from a simple 2D lattice parameter analysis.*

An analysis of the close packed (eutactic)[88] crystal directions of the film and substrate leads to a proposed mechanism for the persistent orientation relationship. The hematite structure is a hexagonal close packed (hcp) network of oxygen atoms, with iron atoms filling ⅔ of the interstitial sites. The close packed oxygen plane is the (0001) plane, and the close packed direction within this plane is the <$1\bar{1}00$> family of directions. The $SrTiO_3$ substrate is a cubic close packed (ccp) network of SrO_3 atoms, with titanium atoms in ¼ of the octahedral interstitial sites. The close packed planes are the {111} family of planes, and the close packed directions within that plane are <$1\bar{1}0$>. The close placed planes, Fe_2O_3[0001] and $SrTiO_3$[111], are also the planes that represent the "out of plane" orientation relationship. The close packed planes are consistently aligned between substrate and film grains. The close packed directions match the determined "in plane" orientation relationship. For Fe_2O_3 films grown on $SrTiO_3$ substrates, the close packed network is aligned between film and substrate over a wide spread of substrate orientation conditions.

It is noted that the use of multiple film/substrate pairs for each substrate grain affects the validity of the statistical analysis of the data. Because each substrate grain resulted in an average of ~4 calculated orientation relationships, much of the data can be thought to represent redundant information. Each additional film grain doesn't represent an entirely unique substrate-grain pair. Despite this, the decision was made to include all data for orientation relationship calculations. In all cases, at least two different film orientation bins were observed on a single substrate grain, regardless of the actual number of film grains. Manually selecting just one of these orientation families could leave out important differences between the film grains. Additionally, in some cases, some film grains showed a very small misorientation between the selected substrate and film directions, while other film grains *on the same substrate grain* showed a much larger misoriention. If only one film grain was selected for each substrate grain, this effect could be amplified or completely missed, depending on the random selection of film grain. Finally, the inclusion of all film/substrate orientation calculations provides

---

*See § 7.1 (p. 57).

a higher sample size. The larger sample size will result in a more accurate statistical depiction of the total population, so long as the limitations here are understood.

The use of polycrystalline substrates and electron backscatter diffraction mapping for film growth analysis represents a technical step forward. The combination of these techniques, called combinatorial substrate epitaxy (CSE), allows for high throughput studies of film growth on high and low index orientations. With the inclusion of a local probe property measurement technique, such as the marker reactions used in this document or AFM probing of electronic properties, effects of orientation on material properties can be investigated. Using CSE, a single film deposition results in hundreds of individual substrate/film pairs. Each of these pairs can be thought to represent a single growth experiment. Even if single crystal substrates could be obtained in all of these orientations, the deposition time alone would prohibit such wide-ranging epitaxy analyses.

8.4 CONCLUSION

Fe_2O_3 films were grown on polycrystalline $SrTiO_3$ substrates. The film-substrate orientation relationship was consistent for most substrate grains. The close packed (eutactic) network of the film grains aligned with that of the substrate grains. For the $Fe_2O_3/SrTiO_3$ system, this results in an arrangement described by $Fe_2O_3[0001]||SrTiO_3[111]$ and $Fe_2O_3[10\bar{1}0]||SrTiO_3[1\bar{1}0]$. This orientation relationship is the same as observed for films on (111)-oriented single crystal substrates, however in this case, the (111) plane is not parallel to the surface for most substrate crystallites. The eutactic orientation relationship persisted, even when the close packed plane was tilted away from the surface normal.

PART IV

EXPERIMENTS ON BISMUTH FERRITE

Chapter 9

Photochemical Reactivity of Bismuth Ferrite Ceramics

The majority of the text in this chapter appears in *ACS Applied Materials & Interfaces*, 2011, 3 (5), pp 1562-1567.[89] It represents the culmination of experimental work from the initial stages of Ph.D. research. The interaction of visible light absorbing films on ferroelectric substrates provided the initial research questions that lead to the research that makes up the bulk of this document. It also represents further experiments regarding the effects of built-in electric fields at the surface of ferroelectric semiconductors on photochemical performance.

9.1   BACKGROUND

Spatially selective photochemical reactivity on the surfaces of ferroelectrics, initiated by the absorption of UV light, has been used to make nanoscale patterns of reduced metal.[20,24–26] The mechanism of the spatially selective reactivity is thought to be the spontaneous polarization in the ferroelectric domains, which bends the bands of electronic states so that photogenerated electrons and holes are transported in opposite directions.[90,91] As a result, electrons are transported to the surfaces of positive domains where reduction products form and holes are transported to the surfaces of negative domains where oxidation products form.[20,21,23,28,59,92]

Spatially selective reactivity induced by ferroelectric polarization may also be beneficial for water photolysis. The recombination of photogenerated charge carriers and the back reaction of intermediate species are major factors that limit the efficiency of water photolysis catalysts,[15,93] and it is possible that these processes will be mitigated by band bending in the domains. This concept has led to a number of studies involving water photolysis[94–96] and spatially selective reactivity on ferroelectric surfaces.[20,21,23,28,59,60,97] However, because the ferroelectrics used in the past have had relatively wide band gaps, they absorbed only a small fraction of the solar spectrum in the UV range. Therefore,

even if losses due to recombination and back reaction are reduced, the overall efficiency suffers from the poor match of the energy levels with the solar spectrum.

The spatial selectivity of photochemical reactivity has been studied on BaTiO3,[20,21,28,59] LiNbO3,[24] and Pb(Zr_xT_{1-x})O_3 (PZT),[25,26] all of which have band gaps larger then 3.0 eV. Here, we investigate the spatial selectivity of ferroelectric and semiconducting BiFeO3, which has a band gap of about 2.5 eV.[98–100] It has been reported BiFeO3 can photochemically degrade organic compounds in visible light[101,102] and thin films of BiFeO3 are photoconductive in visible light.[98] Polycrystalline BiFeO3 ceramics have a polarization of 6.1 µC cm⁻² along the <111> directions of the pseudo-cubic perovskite cell.[103] The purpose of this chapter is to report on the spatially selective photochemical behavior of BiFeO3 surfaces activated by visible light and the relative effects of grain orientation and domain orientation. The products of the reduction reaction correlated with the positions of ferroelectric domains with a positive component of the polarization perpendicular the BiFeO3 surface. On the basis of this and other observations reported below, it is concluded that the ferroelectric polarization decreases electron drift to the surface in domains with a negative component of the polarization perpendicular the surface, causing spatially selective photochemical behavior that is more sensitive to domain orientation than crystal orientation. Further work on the photochemical properties of BiFeO3 and BiFeO3/TiO2 heterostructures was carried out by Zhang.[104] Work on Fe2O3 that comprise the bulk of this document results from the exploration of Fe2O3 as a potential overlayer to iron-based ferroelectric substrates such as BiFeO3.

9.2   EXPERIMENTAL DETAILS

All general procedures described in Chapter 3 were followed. Specific experimental details are described in this section. Polycrystalline pellets of BiFeO3 were prepared from Bi_2O_3 and Fe2O3 starting powders. Powder X-ray diffraction indicated that the majority phase was BiFeO3. Small amounts of $Bi_2Fe_4O_9$, $Bi_{25}FeO_{40}$, and Fe2O3 were also detected in the diffraction pattern and will be referred to collectively as minority phases. The grain orientations within a 1 mm × 1 mm area were determined by electron backscatter diffraction (EBSD) mapping. All patterns were indexed using a cubic reference frame, as the small rhombohedral distortion[37] of BiFeO3 is difficult to distinguish using EBSD. When analyzing the EBSD data, orientations with a confidence index less than 0.1 were removed and appear black in the resulting EBSD maps. Any collection of neighboring orientation points that were misoriented from each other by less than 5° were assumed to belong to a single grain. The orientation of the grain was then determined by averaging the collection of individual orientation points associated with that grain.

Photochemical behavior was examined using the reduction of silver ions to neutral silver, depositing the insoluble silver on the surface.[105,106] The assembly was illuminated for 30 min by a commercially available blue LED (λ_{peak} = 470 nm, Philips Lumileds, San Jose, CA). The LED was powered by a DC supply, set to deliver a constant current of

FIGURE 9.1: (a) Inverse pole figure map showing the grain orientations in the area of the polycrys-
talline BiFeO3 surface where the surface reactivity was determined. Each color corresponds to an
orientation in (b). The orientations of the 24 grains that were studied in detail are illustrated in (c).
The grains with orientations marked by the triangle, square, and diamond are discussed in more
detail below.

FIGURE 9.2: Topographic AFM images of BiFeO3 grain surface with a (001) orientation (a) before
and (b) after the photochemical reduction of Ag. The topographic contrast in both images is 60 nm
from bright to dark. (c) Height profile corresponding to the lines drawn in a and b demonstrating the
height of silver deposits and the spatially selective nature of silver deposition. (d) Out-of-plane PFM
phase image of the same area of the sample. Dark contrast in the image corresponds to regions with a
-180° phase shift (positive polarization) and bright regions correspond to a phase shift of 0° (negative
polarization).

100 mA, corresponding to a power of 0.37 W. The locations of the reaction products
were then determined by AFM imaging. Only samples illuminated by the LED showed
evidence of silver reduction; the surfaces of control samples left in the dark remained
clean. X-ray diffraction of a sample illuminated for several hours (to increase the amount
of reaction product) confirmed that metallic silver had been formed, consistent with
previous findings on other oxides. [20,61]

Scanning probe characterization was performed using either an NT-MDT NTegra or
Solver Next AFM/STM (NT-MDT, Moscow, Russia). Sample topography before and after
photochemical reaction was determined using conventional contact or semicontact
modes with similar results. Conventional methods were used for piezoresponse force
microscopy (PFM) measurements. [107] In this case, a conductive TiN coated cantilever
was used. For scanning tunneling spectroscopy measurements, a 80/20 PtIr tip was
used.

9.3 RESULTS

An inverse pole figure map of the area of the sample used in this study is shown in
Figure 9.1. Each pixel is colored by orientation according to the legend in Figure 9.1(b).
Typically, the undetermined orientations (black points) occur because there was a
grain boundary, pore, or minority phase at that position. The regions of constant color
correspond to grains of constant orientation. Twenty-four of these grains were selected
for closer examination and their orientations are illustrated in Figure 9.1(c). Each
point in Figure 9.1(c) represents an orientation in the standard stereographic triangle of
distinguishable crystal orientations.

AFM images of the grain with the orientation marked by the triangle in Figure 9.1(c)
are shown in Figure 9.2. The surface orientation of this grain is, within the experimental
uncertainty, (001). The same location is shown before and after the photochemical

reduction of silver in images (a) and (b) in Figure 2, respectively. Topographic contrast in the AFM images arises from pores (P), residual polishing scratches (PS), minority phases (MP), surface contamination SC), and boundaries between ferroelectric domains (DB);[48] examples of each feature are labeled on the micrographs. Regions of minority phase were assigned to round features within grains in the AFM images. The presence of minority phase in the bulk was confirmed from the results of X-ray diffraction. These areas are clearly visible in polarized light optical microscopy and in AFM images. The combination of the appearance in optical and AFM microscopy and X-ray diffraction results suggests this assignment as minority phases is appropriate. In Figure 9.2(b), the reduced silver corresponds to areas of bright contrast in the AFM images. The areas of silver deposition follow the areas of ferroelectric domains visible on the images of the clean surface and the heights of the silver deposits vary between 20 and 130 nm. Height profiles are depicted in Figure 9.2(c) for the lines drawn in the AFM images shown in images (a) and (b) in Figure 9.2 before and after the reaction. This direct comparison of the same area of the sample shows a clear distinction in heights for domains before and after the reduction of silver.

After the silver was removed from the sample surface, the sample was returned to the microscope and the same area was examined using piezoresponse force microscopy (PFM). The silver was removed by wiping the surface with a cotton swab and rinsing with deionized water. AFM scans after cleaning show that all silver was removed from the sample. Figure 9.2(d) shows a PFM phase image for the same area of the sample surface depicted in images (a) and (b) in Figure 9.2. The direction of the polarization vector determines the phase lag between the AC bias of the tip and the deflection. Throughout this chapter, domains with a positive out-of-plane polarization will be referred to as "positive" domains and domains with a negative out-of-plane polarization will be referred to as "negative" domains. In the PFM images, the phase lag is 180° for positive domains and 0° for negative domains.[74,75,108,109] Areas of silver deposition correspond to domains that appear dark in the PFM image. These areas correspond to a phase lag of 180°, consistent with positive domains. Bright areas in the PFM image, consistent with negative domains, correspond to areas without significant silver reduction.

The domain polarization is along <111> type directions and the orientations of the boundaries between domains are 110 and 100 type planes for 71° and 109° domain boundaries, respectively.[48] For 180° boundaries, where the polarization vectors are anti-parallel, the plane can take any orientation in the zone of [111]. Therefore, in the general case, we can expect to see both straight and wavy boundaries. When the 71° and 109° domain boundaries intersect the (001) surface, they create traces that intersect at 45° and 90°. Note that all of the straight lines that appear to be domain boundaries in Figure 9.2 are consistent with these expected angles. Grains of other orientations consistently showed either straight lines traversing the entire grain, or combinations of straight and curved boundaries, as illustrated in Figure 9.3.

Figure 9.3 shows AFM topography, PFM phase, and height profile comparisons for two additional grains of the 24 orientations in Figure 9.1(c). The orientation of the grain in Figure 9.3(a) is indicated by the diamond in Figure 9.1(c) and the orientation

FIGURE 9.3: (a, d) Topographic images of BiFeO3 grains after the photochemical reduction of silver. Light to dark contrast for both images is 60 nm. (b, e) Out-of-plane PFM phase images for the same areas. Dark contrast corresponds to a positive out of plane polarization. (c, f) Height profiles corresponding to the line drawn in a and d. The green lines show the topography before the reaction.

FIGURE 9.4: Current versus tip bias measured in a scanning tunneling spectroscopy experiment on the surface of BiFeO3.

of the grain in Figure 9.3(d) is indicated by the square. These results, and those shown in Figure 9.2, are representative of all of the orientations. Silver was reduced on the surface in patterns corresponding to the underlying domain structure. Positive domains promoted silver reduction and negative domains had little to no solid product on the surface after reaction. The amounts of silver reduced on the surfaces shown in Figure 9.3 are similar to the amounts in Figure 9.2 and are characteristic of all of the grain orientations in Figure 9.1(c). In other words, no systematic variation in reactivity could be detected as a function of orientation in this work. However, later studies of a larger number of grains has shown some variation in the reactivity as a function of orientation, though the correlation with domain structure was always observed. In other words, the domain pattern reactivity still dominates the spatial selectivity, but certain orientations did have increased reactivity on the locally reactive domains.

To probe the electronic properties of the sample, current-voltage curves were acquired in the scanning tunneling spectroscopy mode. Because this was done in air, we assume that the tip is actually in weak contact with the sample. Current-voltage curves were acquired at periodic positions on the surface and all appeared similar. A typical curve is shown in Figure 9.4, where rectifying behavior is observed; current flows from the sample to the tip at all positive biases but no current flows from the tip to the sample until the tip is at least one volt more negative than the sample. This behavior is characteristic of a p-type semiconductor where the Fermi level is near the lower edge of the band gap. When the tip is positive with respect to the sample, electrons flow from occupied states in the valence band to the tip. When the tip is made more negative than the sample, the Fermi level of the tip moves through the band gap of the sample until it reaches empty states near the conduction band edge, and electrons can then flow from the tip to the sample. This is illustrated with schematic energy level diagrams in Figure 9.5. A simple two-point resistivity measurement showed that the sample was only weakly conductive and had a resistivity of approximately $1 \times 10^7 \ \Omega$ cm.

9.4   DISCUSSION

The results presented here indicate that the photochemical reduction of silver, initiated by visible light, is spatially selective on the BiFeO3 surface. This is similar to what has

FIGURE 9.5: Diagram showing the theory of scanning tunneling spectroscopy measurements. When the tip is within the band gap, current cannot flow. As the tip is moved to a more positive voltage than the Fermi level, current begins to flow from the sample to the tip. When the tip is moved to a voltage more negative than the Fermi level, electrons flow from the tip to the sample. The voltage difference between the onsets of current flow is roughly equal to the band gap. The horizontal position of the curve determines the carrier type.

been observed previously on BaTiO3, SrTiO3, and PZT when illuminated under UV light. [21,23,29,61,92] Here we propose a model for the surface electronic band structure of BiFeO3, and how it is affected by ferroelectric polarization, to explain the observed reactivity. The proposed energy level structure, shown in Figure 9.6, is based upon a number of assumptions. First, the electron affinity of the BiFeO3 (4.6 eV) was approximated using the method described by Morrison. [8] The band gap of BiFeO3 has been reported over a wide range (2.2-2.7 eV) in different sources; [98–100] in the construction of Figure 9.6, we assumed a band gap of 2.5 eV. Most reports in the literature indicate that BiFeO3 is p-type [110,111] and this is consistent with the current-voltage response shown in Figure 9.4.

FIGURE 9.6: Schematic band diagrams for BiFeO3. In the figure, is the work function, E_o, E_c, E_F, and E_v are the energy levels of a free electron, the conduction band edge, the Fermi level, and the valence band edge, respectively. (a) Bands in bulk BiFeO3. (b) Bands of BiFeO3 in contact with solution, with the standard redox potential for Ag^+/Ag labeled vs the normal hydrogen electrode. (c) Bands in contact with solution and a positive out-of-plane polarization. (d) Bands in contact with solution and a negative out-of-plane polarization.

Figures 9.6(a) and 9.6(b) compare the band positions in bulk BiFeO3 with those near the surface when in contact with solution, with no out-of-plane polarization. Interface states cause downward band bending at the surface of a p-type semiconductor in contact with water. [8] In this case, electron-hole pairs generated within the depletion region are driven apart by the electric field. Electrons are driven towards the surface and holes are driven away from the surface. When electrons reach the surface, they can reduce adsorbed species. Panels (c) and (d) in Figure 9.6 show the effect of ferroelectric polarization on the band bending near the surface. The polarization vector in positive domains, depicted in Figure 9.6(c), causes an increased accumulation of negative charge just below the surface. Band edge energies are driven further downward and the driving force for electrons to reach the surface and participate in photochemical reduction is increased. The opposite is true for a negative domain, which is depicted in Figure 9.6(d). The negative out-of-plane component of polarization causes an increase in positive charge just below the surface and this reduces the downward band bending. If the magnitude of the polarization vector is large enough, the bands bend upwards. We take the experimental observation that silver does not reduce on the surfaces of negative domains as evidence that the bands are bent upward and depict them as

such in Figure 9.6(d), creating a barrier for electrons. In other words, photogenerated electrons within the band bending region are driven away from the surface and this shuts off the silver reduction reaction in these domains. Because electrons and holes are driven to different areas of the surface, the chances of charge carrier recombination are reduced. Additionally, intermediate species produced during the reaction are located in physically separate areas of the surface, reducing back reaction. Because of this, the fields generated by the ferroelectric polarization might improve the efficiency of photochemical reactions. Finally, we note that throughout this discussion, we have ignored the effect of adsorption from the solution. In this case, we would expect aqueous Ag^+ cations to enrich or adsorb at the surfaces of negative domains and be repelled from positive domains. Because reduced silver is found only on the positive domains, the observed spatially selective reactivity is not consistent with adsorption processes.

There are two proposed mechanisms for the orientation dependence of the reactivity of a ferroelectric material. The first is that photochemical reactions on metal oxides are anisotropic. [29,61,62,78,112] While the origins of this anisotropy have not been clearly established, they are presumably connected to the orientation dependence of surface structure, composition, and the exact positions of band edges on the surface. [29,80] This phenomenon is potentially important in the design of a photolysis catalyst. [113]

The second mechanism by which crystal orientation might affect reactivity relates to the crystallographic restrictions on domain polarization. For a given ferroelectric material, the direction of ferroelectric polarization is limited to a distinct set of crystal directions. In the case of $BiFeO_3$, the polarization occurs along the 111 family of directions. [103] The out-of-plane component of the polarization vector is thought to play the most significant role in affecting photochemical activity. Varying the grain orientation changes the possible values of the out-of-plane component of each of the possible polarization directions. For example, a (111)-oriented crystal can have two antiparallel polarization vectors pointing perpendicular to the surface. The remaining six directions point 29° above or below the surface plane, greatly reducing the out of plane component of polarization. In the case of a (001)-oriented grain, all of the polarization vectors point 54° above or below the surface, resulting in an equal out-of-plane magnitude of polarization for all directions. Dunn and co-workers [114] reported on differences in the photochemical reduction of Ag on (001) and (111) oriented PZT, finding that that positive domains in films of both orientations have a similar reactivity, but that negative domains completely stop the reactivity only on the (111) orientation where the polarization is perpendicular to the surface. Burbure and co-workers(10) reported on the relative reactivity of (001), (011), and (111) $BaTiO_3$ (which is polarized along [100]), and found comparable activity for reduction on all three surfaces.

In the current study, spatially selective reactivity was observed for all grain orientations. Contrary to the observations on PZT thin films, even grains with the (001) orientation strongly suppress the reduction of silver in the negative domains (see Figure 9.2). This difference cannot be explained by differences in the polarization: PZT is reported to have a larger remnant polarization than $BiFeO_3$ and that would favor increased spatial selectivity in PZT, counter to what is observed. [115] It is possible that

differences in the microstructure might account for differences in the reactivity. The $BiFeO_3$ crystals studied here were many tens of micrometers in extent, while the PZT was a 70 nm thick film with grains of similar sizes.[114] Because there are geometric constraints on the development of space charges in nano-sized grains, it is possible that the band bending regions are larger in the microcrystalline $BiFeO_3$ samples studied here.[116]

While the differences between $BiFeO_3$ and PZT cannot be resolved from the present observations, the results presented here demonstrate that the ferroelectric domain structure is more important than grain orientation in determining surface reactivity. In grains where ferroelectric domains are present, reactivity was observed to be selective and the heights of reduced silver on the reactive domains did not systematically depend on grain orientation. This lack of a strong anisotropy in reactivity indicates that the relative orientation of the polarization vector is sufficient in $BiFeO_3$ to control the spatial selectivity, consistent with previously published results for $BaTiO_3$.[117] If the relative magnitude of the polarization normal to the surface determined local reactivity, then (111) oriented $BiFeO_3$ grains should have the greatest reactivity in domains with a positive polarization points toward the outer surface. However, the reactive domains on grains oriented near (111) were not noticeably more reactive than reactive domains on grains with different orientations. The same is true for the unreactive, negative domains, where the bands bend upward. A possible explanation for this behavior is found by comparing the depletion layer width and the penetration depth of the illumination. If the photon penetration depth is smaller than the space charge region that results from the ferroelectric polarization, increasing the width of the space charge layer causes no increase in reactivity. All photogenerated charge carriers are already created within the space charge region and driven to or from the surface. Yang et al.[118] estimate a depletion layer width of 300 nm for $BiFeO_3$. The penetration depth for 460 nm light in $BiFeO_3$ is approximately 36 nm, using the extinction coefficient data from Kumar et al.[55] In this case, the space charge region is much larger than the penetration depth, and any increase in the width of the space charge region will not increase the photochemical reactivity of the material. As a result, in any domains where the bands are bend downward, silver is reduced, and in any domains where they are bent upward, no silver is reduced.

It has recently been shown that thin titania films supported by $BiFeO_3$ are also active for silver reduction using the same light source.[104] This indicates that it should be possible to create a heterostructured core-shell photocatalyst of $BiFeO_3$ particles coated by a thin layer of titania that will combine the favorable band edge positions and stability of the titania surface with the light absorbing and charge separating characteristics of the $BiFeO_3$ core. The present results suggest that in such a composite material, the shape of the $BiFeO_3$ crystals will not be important, but the size will. To effectively absorb light, the cores will have to be at least twice the absorption depth and to effectively separate charge, they should be large enough to sustain a ferroelectric polarization that promotes band bending, and this is twice the width of the space charge region. Because these two lengths will not generally be the same, the reactivity may be size dependent.

9.5   CONCLUSION

BiFeO3 surfaces exhibit spatially selective visible-light photochemical activity. Silver ions in solution were photochemically reduced by the BiFeO3, depositing solid silver on the surface in patterns corresponding to positive ferroelectric domains. Upward band bending in the negative domains prevents electrons from reaching the surface and these locations do not reduce silver. Electric fields arising from ferroelectric domains at the surface overwhelm anisotropy in the photochemical activity that might arise from grain orientation alone.

PART V

SUMMARY, CONCLUSIONS, & FUTURE PATHS

Chapter 10

Conclusions & Future Work

10.1 SUMMARY OF PHOTOCHEMICAL ACTIVITY RESULTS

The visible light photochemical activity of Fe_2O_3 in different structures has been studied. Anisotropic photochemical reactivity was observed for bulk hematite polycrystals. Two identical Fe_2O_3 films supported on different substrates showed highly different photochemical activities. The film supported on the $SrTiO_3(111)$ surface was much more reactive than the film on $Al_2O_3(0001)$. These films were even more reactive than for bulk Fe_2O_3 polycrystals, even though significantly less light was absorbed in the film structure, owing to the thinness of the film.

The same was true for films on polycrystalline $SrTiO_3$ substrates. The reactive grains of films on polycrystalline substrate were significantly more reactive than the bulk material. The orientation dependence of reactivity for these films echoed that of bulk Fe_2O_3, but increased the range of orientations that promoted reactive grains. For the bulk material, only grains located relatively near the $(1\bar{2}10)$ orientation were observed to be reactive. For the film, grains significantly farther from this orientation were observed to be reactive, and grains that were completely nonreactive in the bulk material were at least moderately reactive for the film.

The orientation dependence of the photochemical reactivity of Fe_2O_3 itself is a new observation. Previous studies of anisotropic photochemical activity for hematite crystals were much narrower in scope, focusing only on differentiating basal and prismatic surfaces. The work in this document was able to differentiate levels of reactivity between different prismatic surfaces, as well as the reactivity of high index surfaces. Additionally, Kelvin probe force microscopy showed that the surface potential of reactive grains was higher than that for nonreactive grains.

10.2   SUMMARY OF FILM GROWTH RESULTS

In the process of examining the photochemical activity of Fe_2O_3 films, Fe_2O_3 film growth was also studied. Electron backscatter diffraction was used to map the orientation of substrates and their corresponding films. From this data, orientation relationships between the substrate and film were determined. Polycrystalline films on $SrTiO_3(001)$ substrates showed unusual texture. It was determined that for a significant portion of film grains, the grain orientation was a result of the alignment of crystal directions far away from the surface normal. For $SrTiO_3(001)$ substrates, the alignment of the substrate [111] direction with the film [0001] direction was observed. The corresponds with the orientation relationship observed on $SrTiO_3(111)$ substrates. The idea of epitaxy on high index orientations was also examined through EBSD studies of film growth on polycrystalline substrates. For films on polycrystalline substrates, it was observed that the film accepted its orientation according to the eutactic arrangement of the substrate grains. As the arrangement of the close packed network of the substrate tilted in space, the arrangement of the close packed network of the film followed. The close packed network of the film consistently lined up with that of the substrate over a wide spread of substrate orientations.

Together, this work represents a step forward in the understanding of mechanisms for creating charged interfaces. It also represents progress in the incorporation of visible light active materials into these heterostructures. In the experiments presented in this document, visible light illumination drives most photochemical reactions. Charge carriers are only generated in the film, different from earlier studies on heterostructures with charged interfaces. EBSD has previously been used to study the orientation relationships between substrate and film. However the analysis presented in this document is significantly more complicated. Unlike earlier studies, entire maps of film orientations could be obtained. This allows for the analysis of a much larger dataset. The study of polycrystalline film growth and texture on single crystal substrates, and the use of EBSD to measure epitaxy at high index orientations is an interesting new development.

10.3   SUMMARY OF BISMUTH FERRITE RESULTS

$BiFeO_3$ surfaces exhibit spatially selective visible-light photochemical activity. Silver ions in solution were photochemically reduced by the $BiFeO_3$, depositing solid silver on the surface in patterns corresponding to positive ferroelectric domains. Upward band bending in the negative domains prevents electrons from reaching the surface and these locations do not reduce silver. Electric fields arising from ferroelectric domains at the surface overwhelm anisotropy in the photochemical activity that might arise from grain orientation alone.

10.4   FUTURE PATHS

The work presented in this document provides numerous research paths for future exploration. The results presented here are not entirely consistent with the hypothesis that the presence of polar surface terminations are responsible for the increased photochemical activity. The comparison of photochemical activity for Fe_2O_3 films on $SrTiO_3(001)$ and $SrTiO_3(111)$ surfaces is not yet complete. This comparison removes other possibilities for the explanation of the higher reactivity of films on $SrTiO_3(111)$ substrates. The difficulty in this comparison lies in the differing microstructures of films on $SrTiO_3(001)$ and $SrTiO_3(111)$. This comparison would test the hypothesis that the polar $SrTiO_3(111)$ surface is responsible for the increased reactivity. Additionally, experiments designed to explicitly isolate the presence and effects of polar surfaces would help reinforce this interpretation of the results reported within this document.

The use of electron backscatter diffraction and polycrystalline substrates to perform combination substrate epitaxy (CSE) experiments is still in its infancy. So far, this technique has been used to study TiO_2 film growth on $BaTiO_3$ and $BiFeO_3$ and, within this document, Fe_2O_3 films on $SrTiO_3$ substrates. These leave a huge range of film and substrate materials open for future exploration with this technique. Additionally, the idea of eutactic epitaxy arrangements offers an opportunity to predict and develop models for film growth on high index surfaces or for complex heteroepitaxial systems. Future results could be used to develop a model for the thermodynamic and kinetic factors influencing the relative rates of nucleation and growth for eutactic orientations.

Finally, the use of the marker reactions in this document provides initial evidence regarding the photochemical activity of the materials presented in this document. However, the marker reactions are significantly different in nature than those involved in the practical applications of photochemically active materials. Implementing conventional photoelectrochemical testing methods for the analysis of the heterostructures presented in this document would help compare the structures here to other reports of photochemical activity.

References

[1]   Report, Basic Energy Sciences Workshop: "Basic Research Needs for the Hydrogen Economy." Tech. rep., 2004.

[2]   A. Fujishima and K. Honda: *Nature*, 1972. vol. 238 (5358), pp. 37–38.

[3]   M. Grätzel: *Nature*, 2001. vol. 414, pp. 338–344.

[4]   A. J. Frank, I. Willner, Z. Goren, and Y. Degani: *Journal of the American Chemical Society*, 1987. vol. 109 (12), pp. 3568–3573.

[5]   K. E. Karakitsou and X. E. Verykios: *The Journal of Physical Chemistry*, 1993. vol. 97 (6), pp. 1184–1189.

[6]   A. L. Linsebigler, G. Lu, and J. T. Yates: *Chemical Reviews*, 1995. vol. 95 (3), pp. 735–758.

[7]   G. N. Schrauzer and T. D. Guth: *Journal of the American Chemical Society*, 1977. vol. 99 (22), pp. 7189–7193.

[8]   S. R. Morrison: *Electrochemistry at Semiconductor and Oxidized Metal Electrodes*, Plenum Pub Corp, New York, 1980.

[9]   R. Memming: *Semiconductor Electrochemistry*, John Wiley & Sons, New York, 2001.

[10]   *CRC Handbook of Chemistry and Physics*, CRC Press, New York, 2007, 88th ed.

[11]   F. E. Osterloh: *Chemistry of Materials*, 2008. vol. 20 (1), pp. 35–54.

[12]   ASTM Standard: "ASTM G173-03: Standard Tables for Reference Solar Spectral Irradiances: Direct Normal and Hemispherical on $37°$ Tilted Surface." Tech. rep., ASTM International, West Conshohocken, PA, 2008.

[13]   M. Kaneko and I. Okura: *Photocatalysis: Science and Technology*, Springer, New York, 2002.

[14]   M. Kitano, K. Tsujimaru, and M. Anpo: *Topics in Catalysis*, 2008. vol. 49 (1-2), pp. 4–17.

[15]   A. Kudo and Y. Miseki: *Chemical Society Reviews*, 2008. vol. 38 (1), pp. 253–278.

[16]   L. Marusak: *Journal of Physics and Chemistry of Solids*, 1980. vol. 41 (9), pp. 981–984.

[17]   M. Lines and A. Glass: *Principles and Applications of Ferroelectrics and Related Phenomena*, New York, 1977.

[18]   G. Haertling: *Journal of the American Ceramic Society*, 1999. vol. 82 (4), pp. 797–818.

[19]   P. Forsbergh Jr: *Physical Review*, 1949. vol. 76 (8), pp. 1187–1201.

[20]   J. L. Giocondi and G. S. Rohrer: *The Journal of Physical Chemistry B*, 2001. vol. 105 (35), pp. 8275–8277.

[21]   N. V. Burbure, P. A. Salvador, and G. S. Rohrer: *Chemistry of Materials*, 2010. vol. 22 (21), pp. 5831–5837.

[22]   J. Giocondi: *Effect of Dipolar Fields, Surface Termination, and Surface Orientation on Photochemical Reactions on Transition Metal Oxides.* Ph.D. thesis, Carnegie Mellon University, 2003.

[23]   J. L. Giocondi and G. S. Rohrer: *Chemistry of Materials*, 2001. vol. 13 (2), pp. 241–242.

[24]   J. N. Hanson, B. J. Rodriguez, R. J. Nemanich, and A. Gruverman: *Nanotechnology*, 2006. vol. 17 (19), pp. 4946–4949.

[25]   S. V. Kalinin, D. A. Bonnell, T. Alvarez, X. Lei, Z. Hu, J. H. Ferris, Q. Zhang, and S. Dunn: *Nano Letters*, 2002. vol. 2 (6), pp. 589–593.

[26]   D. Tiwari and S. Dunn: *Journal of Materials Science*, 2009. vol. 44 (19), pp. 5063–5079.

[27]   N. V. Burbure, P. A. Salvador, and G. S. Rohrer: *Journal of the American Ceramic Society*, 2006. vol. 89 (9), pp. 2943–2945.

[28]   N. Burbure, P. A. Salvador, and G. S. Rohrer: *Chemistry of Materials*, 2010. vol. 22, pp. 5823–5830.

[29]   J. Giocondi and G. S. Rohrer: *Journal of the American Ceramic Society*, 2003. vol. 86 (7), pp. 1182–1189.

[30]   M. Opel: *Journal of Physics D: Applied Physics*, 2012. vol. 45 (3), pp. 033001–033032.

[31]   M. A. Herman, W. Richter, and H. Sitter: *Epitaxy: Physical Principles and Technical Implementation*, vol. 62 of *Springer Series in Materials Science*, Springer, New York, 2004.

[32] D. E. Hooks, T. Fritz, and M. D. Ward: *Advanced Materials*, 2001. vol. 13 (4), pp. 227–241.

[33] Y. Lin, G. Yuan, S. Sheehan, S. Zhou, and D. Wang: *Energy & Environmental Science*, 2011. vol. 4 (12), pp. 4862–5096.

[34] K. Sivula, F. Le Formal, and M. Grätzel: *ChemSusChem*, 2011. vol. 4 (4), pp. 432–449.

[35] M. Gondal, A. Hameed, Z. Yamani, and A. Suwaiyan: *Applied Catalysis A: General*, 2004. vol. 268 (1-2), pp. 159–167.

[36] J. Cao, T. Kako, N. Kikugawa, and J. Ye: *Journal of Physics D: Applied Physics*, 2010. vol. 43 (32), pp. 325101–325108.

[37] J. Luo and P. A. Maggard: *Advanced Materials*, 2006. vol. 18 (4), pp. 514–517.

[38] Y. Wang, T. Yu, X. Chen, H. Zhang, S. Ouyang, Z. Li, J. Ye, and Z. Zou: *Journal of Physics D: Applied Physics*, 2007. vol. 40 (13), pp. 3925–3930.

[39] H. Maruska: *Solar Energy Materials*, 1979. vol. 1 (5-6), pp. 411–429.

[40] A. S. Bhalla, R. Guo, and R. Roy: *Materials Research Innovations*, 2000. vol. 4 (1), pp. 3–26.

[41] A. Kingon, J. Maria, and S. Streiffer: *Nature*, 2000. vol. 406 (6799), pp. 1032–1038.

[42] W. Z. Zhu and S. C. Deevi: *Materials Science and Engineering: A*, 2003. vol. 362 (1-2), pp. 228–239.

[43] S. P. Jiang: *Journal of Materials Science*, 2008. vol. 43 (21), pp. 6799–6833.

[44] J. Fergus: *Sensors and Actuators B: Chemical*, 2007. vol. 123 (2), pp. 1169–1179.

[45] D. Murphy, S. Sunshine, R. Van Dover, R. Cava, B. Batlogg, S. Zahurak, and L. Schneemeyer: *Physical Review Letters*, 1987. vol. 58 (18), pp. 1888–1890.

[46] E. Lombardo and M. Ulla: *Research on Chemical Intermediates*, 1998. vol. 24 (5), pp. 581–592.

[47] M. Cardona: *Phys Rev*, 1965. vol. 114, pp. 651–655.

[48] G. Catalan and J. F. Scott: *Advanced Materials*, 2009. vol. 21 (24), pp. 2463–2485.

[49] I. Kornev, S. Lisenkov, R. Haumont, B. Dkhil, and L. Bellaiche: *Physical Review Letters*, 2007. vol. 99 (22), pp. 227602–1–227602–4.

[50] S. Shetty, V. Palkar, and R. Pinto: *Pramana–Journal of Physics*, 2002. vol. 58 (5-6), pp. 1027–1030.

[51]   H. Miao, Q. Zhang, G. Tan, and G. Zhu: *Journal of Wuhan University of Technology-Mater. Sci. Ed.*, 2008. vol. 23 (4), pp. 507–509.

[52]   F. Kubel and H. Schmid: *Acta Crystallographica*, 1990, pp. 1–5.

[53]   J. F. Ihlefeld, N. J. Podraza, Z. K. Liu, R. C. Rai, X. Xu, T. Heeg, Y. B. Chen, J. Li, R. W. Collins, J. L. Musfeldt, X. Q. Pan, J. Schubert, R. Ramesh, and D. G. Schlom: *Applied Physics Letters*, 2008. vol. 92 (14), pp. 142908–1–142908–3.

[54]   S. J. Clark and J. Robertson: *Applied Physics Letters*, 2007. vol. 90 (13), pp. 132903–1–132903–3.

[55]   A. Kumar, R. C. Rai, N. J. Podraza, S. Denev, M. Ramirez, Y.-H. Chu, L. W. Martin, J. Ihlefeld, T. Heeg, J. Schubert, D. G. Schlom, J. Orenstein, R. Ramesh, R. W. Collins, J. L. Musfeldt, and V. Gopalan: *Applied Physics Letters*, 2008. vol. 92 (12), pp. 121915–1–121915–3.

[56]   S. Streiffer, C. Parker, A. Romanov, M. Lefevre, L. Zhao, J. Speck, W. Pompe, C. Foster, and G. Bai: *Journal of Applied Physics*, 1998. vol. 83 (5), pp. 2742–2753.

[57]   D. B. Chrisey and G. K. Hubler: *Pulsed Laser Deposition of Thin Films*, Wiley-Interscience, New York, 1994.

[58]   A. J. Francis and P. A. Salvador: *Journal of Applied Physics*, 2004. vol. 96 (5), pp. 2482–2493.

[59]   A. Bhardwaj, N. V. Burbure, A. Gamalski, and G. S. Rohrer: *Chemistry of Materials*, 2010. vol. 22 (11), pp. 3527–3534.

[60]   J. L. Giocondi and G. S. Rohrer: *Topics in Catalysis*, 2008. vol. 49 (1-2), pp. 18–23.

[61]   J. B. Lowekamp, G. S. Rohrer, P. A. Morris Hotsenpiller, J. D. Bolt, and W. E. Farneth: *The Journal of Physical Chemistry B*, 1998. vol. 102 (38), pp. 7323–7327.

[62]   P. A. Morris Hotsenpiller, J. D. Bolt, W. E. Farneth, J. B. Lowekamp, and G. S. Rohrer: *The Journal of Physical Chemistry B*, 1998. vol. 102 (17), pp. 3216–3226.

[63]   J. W. Bullard and M. J. Cima: *Langmuir*, 2006. vol. 22 (24), pp. 10264–10271.

[64]   G. A. Parks: *Chemical Reviews*, 1965. vol. 62 (2), pp. 177–198.

[65]   M. Kosmulski: *J Colloid Interface Sci*, 2004. vol. 275 (1), pp. 214–24.

[66]   M. Kosmulski: *J Colloid Interface Sci*, 2002. vol. 253 (1), pp. 77–87.

[67]   M. Kosmulski: *Chemical Properties of Material Surfaces*, Marcel Dekker, Inc., New York, 2001.

[68] B. G. Ershov, E. Janata, and A. Henglein: *The Journal of Physical Chemistry*, 1993. vol. 97 (2), pp. 339–343.

[69] D. L. Van Hyning, W. G. Klemperer, and C. F. Zukoski: *Langmuir*, 2001. vol. 17 (11), pp. 3128–3135.

[70] D. Dingley: *Materials Science and Technology*, 1997. vol. 13, pp. 69–78.

[71] A. J. Schwartz and M. Kumar: *Electron Backscatter Diffraction in Materials Science*, Springer Verlag, New York, 2009.

[72] M. Birkholz: *Thin Film Analysis by X-Ray Scattering*, John Wiley & Sons, New York, 2006.

[73] G. Binnig, C. Quate, and C. Gerber: *Physical Review Letters*, 1986. vol. 56 (9), pp. 930–933.

[74] S. V. Kalinin and D. Bonnell: *Physical Review B*, 2002. vol. 65 (12), pp. 125408–1–125408–11.

[75] S. V. Kalinin, E. A. Eliseev, and A. N. Morozovska: *Applied Physics Letters*, 2006. vol. 88 (23), pp. 232904–1–232904–3.

[76] T. Jungk, Á. Hoffmann, and E. Soergel: *Applied Physics Letters*, 2006. vol. 89 (16), pp. 163507–1–163507–3.

[77] B. J. Rodriguez: *Journal of Applied Physics*, 2004. vol. 95 (4), pp. 1958–1962.

[78] T. Ohno, K. Sarukawa, and M. Matsumura: *New Journal of Chemistry*, 2002. vol. 26 (9), pp. 1167–1170.

[79] P. Hotsenpiller, J. Bolt, W. Farneth, J. Lowekamp, and G. Rohrer: *The Journal of Physical Chemistry B*, 1998. vol. 102 (17), pp. 3216–3226.

[80] J. L. Giocondi, P. A. Salvador, and G. S. Rohrer: *Topics in Catalysis*, 2007. vol. 44 (4), pp. 529–533.

[81] J. L. Giocondi and G. S. Rohrer: *Mat. Res. Soc. Symp. Proc.*, 2003. vol. 751, pp. 19–24.

[82] C. M. Eggleston, A. J. A. Shankle, A. J. Moyer, I. Cesar, and M. Grätzel: *Aquatic Sciences*, 2009. vol. 71 (2), pp. 151–159.

[83] N. Iordanova, M. Dupuis, and K. M. Rosso: *Journal of Chemical Physics*, 2005. vol. 122 (14), pp. 144305–1–144305–10.

[84] D. Benjelloun, J.-P. Bonnet, J.-P. Doumerc, J.-C. Launay, M. Onillon, and P. Hagenmuller: *Materials Chemistry and Physics*, 1984. vol. 10 (6), pp. 503–518.

[85]   M. N. Huda, A. Walsh, Y. Yan, S.-H. Wei, and M. M. Al-Jassim: *Journal of Applied Physics*, 2010. vol. 107 (12), p. 123712.

[86]   A. Schultz, P. A. Salvador, and G. S. Rohrer: *Chemical Communications*, 2012. vol. 48 (14), pp. 2012–2014.

[87]   R. French and H. Müllejans: *Journal of the American Ceramic Society*, 1998. vol. 81 (10), pp. 2549–2547.

[88]   M. O'Keeffe: *Acta Crystallographica*, 1977. vol. A33, pp. 924–927.

[89]   A. Schultz, Y. Zhang, P. A. Salvador, and G. S. Rohrer: *ACS Applied Materials & Interfaces*, 2011. vol. 3 (5), pp. 1562–1567.

[90]   P. Brody: *Solid State Communications*, 1973. vol. 12 (7), pp. 673–676.

[91]   V. Fridkin: *Ferroelectrics*, 1984. vol. 53, pp. 169–187.

[92]   S. Dunn, P. M. Jones, and D. E. Gallardo: *Journal of the American Chemical Society*, 2007. vol. 129 (28), pp. 8724–8728.

[93]   K. Domen: *Surface photochemistry*, chap. Characteristics of Photoexcitation Processes on Solid Surfaces, John Wiley & Sons Inc, New York, 1996.

[94]   Y. Inoue: *Energy & Environmental Science*, 2009. vol. 2 (4), pp. 364–386.

[95]   Y. Inoue, O. Hayashi, and K. Sato: *Journal of the Chemical Society, Faraday Transactions*, 1990. vol. 86 (12), pp. 2277–2282.

[96]   Y. Inoue, K. Sato, K. Sato, and H. Miyama: *Journal of Physical Chemistry*, 1986. vol. 90 (13), pp. 2809–2810.

[97]   A. Bhardwaj, N. V. Burbure, and G. S. Rohrer: *Journal of the American Ceramic Society*, 2010. vol. 93 (12), pp. 4129–4134.

[98]   S. R. Basu, L. W. Martin, Y. H. Chu, M. Gajek, R. Ramesh, R. C. Rai, X. Xu, and J. L. Musfeldt: *Applied Physics Letters*, 2008. vol. 92 (9), pp. 091905–1–091905–3.

[99]   T. Choi, S. Lee, Y. J. Choi, V. Kiryukhin, and S. W. Cheong: *Science*, 2009. vol. 324 (5923), pp. 63–66.

[100] F. Gao, Y. Yuan, K. F. Wang, X. Y. Chen, F. Chen, J. M. Liu, and Z. F. Ren: *Applied Physics Letters*, 2006. vol. 89 (10), pp. 102506–1–102506–3.

[101] C. M. Cho, J. H. Noh, I.-S. Cho, J.-S. An, K. S. Hong, and J. Y. Kim: *Journal of the American Ceramic Society*, 2008. vol. 91 (11), pp. 3753–3755.

[102] F. Gao, X. Y. Chen, K. B. Yin, S. Dong, Z. F. Ren, F. Yuan, T. Yu, Z. G. Zou, and J. M. Liu: *Advanced Materials*, 2007. vol. 19 (19), pp. 2889–2892.

[103] J. Teague, R. Gerson, and W. James: *Solid State Communications*, 1970. vol. 8 (13), pp. 1073–1074.

[104] Y. Zhang, A. Schultz, P. A. Salvador, and G. S. Rohrer: *Journal of Materials Chemistry*, 2011. vol. 21 (12), pp. 4168–4174.

[105] W. Clark: *Journal of Catalysis*, 1965. vol. 4 (6), pp. 691–696.

[106] J. Herrmann: *Journal of Catalysis*, 1988. vol. 113 (1), pp. 72–81.

[107] J. Christman, R. Woolcott Jr, and A. Kingon: *Applied Physics Letters*, 1998. vol. 73, pp. 3851–3853.

[108] S. V. Kalinin and D. Bonnell: *Physical Review B*, 2001. vol. 63 (12), pp. 125411–1–125411–3.

[109] S. V. Kalinin, E. Karapetian, and M. Kachanov: *Physical Review B*, 2004. vol. 70 (18), pp. 184101–1–184101–24.

[110] B. Vengalis, J. Devenson, A. K. Oginskis, R. Butkute, A. Maneikis, A. Steikoniene, L. Dapkus, J. Banys, and M. Kinka: *Acta Physica Polonica A*, 2008. vol. 113, pp. 1095–1098.

[111] H. G. Yang, H. M. Luo, H. Wang, I. O. Usov, N. A. Suvorova, M. Jain, D. M. Feldmann, P. C. Dowden, R. F. DePaula, and Q. X. Jia: *Applied Physics Letters*, 2008. vol. 92 (10), pp. 102113–1–102113–3.

[112] T. Taguchi, Y. Saito, K. Sarukawa, T. Ohno, and M. Matsumura: *New Journal of Chemistry*, 2003. vol. 27 (9), pp. 1304–1306.

[113] B. D. Sosnowchik, H. C. Chiamori, Y. Ding, J.-Y. Ha, Z. L. Wang, and L. Lin: *Nanotechnology*, 2010. vol. 21 (48), pp. 485601–1–485601–6.

[114] S. Dunn, D. Tiwari, P. M. Jones, and D. E. Gallardo: *Journal of Materials Chemistry*, 2007. vol. 17 (42), pp. 4460–4463.

[115] T. Kobayashi, M. Ichiki, J. Tsaur, and R. Maeda: *Thin Solid Films*, 2005. vol. 489 (1), pp. 74–78.

[116] W. Albery and P. Bartlett: *Journal of the Electrochemical Society*, 1984. vol. 131 (2), pp. 315–325.

[117] N. Burbure, P. A. Salvador, and G. S. Rohrer: *Journal of the American Ceramic Society*, 2010. vol. 93 (9), pp. 2530–2533.

[118] S. Y. Yang, L. W. Martin, S. J. Byrnes, T. E. Conry, S. R. Basu, D. Paran, L. Reichertz, J. F. Ihlefeld, C. Adamo, A. Melville, Y. H. Chu, C. H. Yang, J. L. Musfeldt, D. G. Schlom, J. W. Ager, and R. Ramesh: *Applied Physics Letters*, 2009. vol. 95 (6), pp. 062909–1–062909–3.

PART VI

APPENDIX

Chapter 11

Hematite Films on Polycrystalline Barium Titanate Substrates

This chapter presents results photochemical activity of Fe_2O_3 films deposited on polycrystalline $BaTiO_3$ substrates. $BaTiO_3$ was initally selected as the substrate material for its ferroelectric properties. Photochemical activity under visible and ultraviolet illumination was tested using the marker reaction of the reduction of aqueous silver to solid silver. However, photochemical properties were the primary driver of this investigation, leading to the choice of $BaTiO_3$. Following a suggestion of the dissertation committee, the work was repeated on a polycrystalline $SrTiO_3$ substrate to provide better comparison with results on single crystal $SrTiO_3$ substrates. Those results are presented in Chapters 6 and 8. The results for $BaTiO_3$ substrates are included here to better show the research progression, and to provide initial results for the effect of ferroelectric substrates on the reactivity of Fe_2O_3 films.

11.1 EXPERIMENTAL DETAILS

Polycrystalline $BaTiO_3$ pellets were prepared following the method described by Giocondi.[22] Fe_2O_3 films were deposited on these substrates following the procedures described in Chapter 3 for pulsed laser deposition. For film growth analysis, the film thickness was 180 nm to ensure EBSD signals were representative the film, rather than the substrate. For photochemical activity measurements, the same 180 nm thick film sample was used, as well as 60 nm and 7 nm thick films on different $BaTiO_3$ pellets.

11.2 DOMAIN-SELECTIVE REACTIVITY

Earlier work studying the photochemical activity of thin titania films supported on ferroelectric substrates has shown that photochemical reaction with aqueous salts occurs

on spatially selective regions of the film surface, corresponding to the ferroelectric domains of the substrate.[21,27,28] Burbure[21] attempted to qualitatively describe the band structure of these heterostructures, and the resulting band diagrams are depicted in Figure 11.1. Burbure proposed that the band bending in the substrate arising from

FIGURE 11.1: Schematic showing the proposed band bending of a TiO2/BaTiO3 heterostructure owing to the ferroelectric BaTiO3 substrate.[21]

the ferroelectric field is responsible for driving charge carriers in opposite directions, and that domains of opposite polarization will drive opposite charge carriers to the surface of the film. The film material was assumed to be too thin to allow for total equilibrium between the film bands, the substrate bands, and the solution. The scheme in Figure 11.1 suggests that charge carriers in the film experience an electric field in the opposite direction of the field experienced in the substrate. It was assumed that the charge carriers reaching in the film would arrive with enough energy to reach the surface of the film. But the question of what happens to charge carriers generated in the film remains. The scheme in Figure 11.1 suggests that if charge carriers were generated solely in the film material, domain-selective reactivity would persist, but would occur on domains of the opposite polarization. In the TiO2/BaTiO3 system, this effect couldn't be tested. Because the film is so thin, it is stated that the majority of the charge carriers involved in photochemical reaction are generated in the substrate. Additionally, the band gaps of the substrate (~3.2 eV) and film (~3.0 eV) materials were too similar to use optical filters to prevent charge carriers from being generated in the substrate.

The use of Fe2O3 as a film material presents the opportunity to overcome those limitations, and test the photochemical behavior of charge carriers generated in the film. Under the visible light illumination used for earlier photochemical experiments, charge carriers would only be generated in the film of an Fe2O3/BaTiO3 heterostructure. The band gap of the substrate is too large for the absorption of blue light to excite an electron from the valence band to the conduction band. The marker reaction of the reduction of aqueous silver was used to test the spatial selectivity of reaction for charge carriers generated in the visible light absorbing film.

A 60 nm hematite film was deposited on a polycrystalline BaTiO3 substrate. The substrate was prepared, polished, and annealed as described in the experimental chapter of this document. Deposition procedures and conditions were the same as described previously for the growth of Fe2O3 films. Figure 11.2 shows the AFM micrographs surface of the film after the photochemical marker reaction with AgNO3 under blue LED illumination. Illumination time was 30 min, and the current through the LED was 500 mA. Unlike the TiO2/BaTiO3 heterostructures, the reaction product on the surface of Fe2O3 films on BaTiO3 substrates do not appear in patterns corresponding to the ferroelectric domains of the substrate. This was true for all examined grains of the sample. This suggests that under visible light illumination, when charge carriers are only generated in the film, spatially selective reactivity does not occur.

FIGURE 11.2: Surface of an Fe_2O_3 film on $BaTiO_3$ after reaction with $AgNO_3$ solution under visible light illumination. No patterns corresponding to the ferroelectric domains of the substrate are observed.

The selectivity of photochemical reactions on Fe_2O_3/$BaTiO_3$ heterostructures under ultraviolet illumination was also tested. Under UV light, the majority of the charge carriers are expected to be generated in the substrate, and the behavior of the heterostructure is expected to be similar of that of TiO_2 films on $BaTiO_3$ substrates. AFM scans of the surface of the 7 nm thick film before and after reaction under UV light are shown in Figure 11.3. No domain-specific spatially-selective reactivity is observed in

FIGURE 11.3: AFM deflection image of the surface of a 7 nm thick Fe_2O_3 film on $BaTiO_3$ after reaction with $AgNO_3$ under UV light. The heterostructure does not show the same behavior as TiO_2/$BaTiO_3$ heterostructures.

these micrographs. No other examined areas of the sample showed spatially selective reactivity.

Burbure observed that spatially-selective reactivity could be turned off by increasing the thickness of the film, or by increasing the density of charge carriers in the film. It was hypothesized that both of these factors resulted in a completely screened space charge-region within the film. By increasing the film thickness without changing the charge carrier concentration in the film, eventually the film is thicker than the space-charge region in the film. The film is able to completely screen the electric fields arising from the buried ferroelectric interface, and spatially-selective reactivity no longer occurs. As the width of the space charge region is inversely proportional to the carrier concentration in the film. If the carrier concentration in the film is increased, the space-charge width is decreased, and even very thin films are able to completely screen the fields from ferroelectric polarization. A possible explanation for the lack of spatially-selective reactivity on the Fe_2O_3 films is the possibility of a much higher film charge carrier density than for TiO_2 films. If this is the case, it is possible even the 7 nm Fe_2O_3 film could be completely screening the ferroelectric polarization.

For all Fe_2O_3 films on $BaTiO_3$ substrates, spatially selective photochemical reactivity was never observed. This suggests that Fe_2O_3 films behave fundamentally differently than TiO_2 films on the same substrates. Film quality and interface quality are possible explanations for the differing behavior. Chemical similarity between TiO_2 and $BaTiO_3$ could result in higher quality films, with fewer defects in the film. As defects are scattering centers, acting as obstacles to charge carrier transport, a lower quality film would hinder the movement of charge carriers from the substrate to the surface of the film. The results on Fe_2O_3 film growth presented earlier in this chapter show that a significant fraction of the substrate grains nucleated epitaxial film grains of high enough

crystallinity for automated EBSD indexing. This suggests that poor film quality is not the explanation for the lack of selective reactivity. The nature of the interface between the film and substrate is not known. If the interface is composed of a thin layer of highly disordered material, this could prevent charge carriers from leaving the substrate and entering the film. This would explain the overall low levels of reactivity observed, and the lack of selective reactivity. A final explanation would be that the charge carrier concentration in the film is high enough that even a 5 nm film completely screen the charge of the ferroelectric substrate. Currently, the charge carrier density of the Fe_2O_3 films is unknown. An accurate measurement of the film charge carrier density will help determine whether this is the cause of the lack of spatially-selective reactivity.

11.3   GRAIN-SELECTIVE REACTIVITY

While testing for selective reactivity resulting from the ferroelectric domains of the substrate, and it was observed that certain film grains of an Fe_2O_3 film on polycrystalline $BaTiO_3$ were much more reactive than other grains. Figure 11.4 shows a screen capture of the optical viewing system taken during AFM measurements of the film surface after reaction with $AgNO_3$. Some grains appear brown in the image. These grains correspond

FIGURE 11.4: Screenshot of the optical viewing system of an AFM showing grain selective reactivity. Brown grains correspond to regions with a high concentration of photochemical reaction product on the surface.

to grains with a high amount of reaction product on the surface. After the surface of the sample was cleaned, as shown in Figure 11.5, all the grains appeared similar, and the reaction product was no longer visible. A difference in photochemical reactivity

FIGURE 11.5: The same area of the surface depicted in Figure 11.4 after cleaning, showing that the brown material was indeed reaction product, and could be cleaned from the surface.

high enough to be so easily observed in the optical viewing system of the AFM has not typically been observed in previous experiments on other material systems.

The area of the sample shown in this figure corresponds to the same area of the sample used to determine the orientation relationships between the substrate grains and the film grains. As a result, the orientations of the substrate and film grains are known. Figure 11.6 shows the optical microscopy image overlaid on the inverse pole map, clearing showing that the grains with a consistent, easily indexed orientation were the grains with the high photochemical activity. What is striking is that the grains with

FIGURE 11.6: Inverse pole map from Figure **??**(b) overlaid on the image from Figure 11.4. In many cases, the grains that showed high photochemical activity are also grains that nucleated high quality Fe2O3 films.

high photochemical activity correspond to grains that indexed well during the EBSD scan.

Two explanations are proposed for the increased reactivities of these grains. All of the film grains with high reactivity are oriented near the (0001) direction, with the c-axis pointing out of the sample surface. The substrate grains are predominately (111) and (011) oriented grains. All of the film grains that did not demonstrate high reactivity were also grains that were not indexed during the automated EBSD process. This suggests that the grains are either amorphous, or polycrystalline with grain sizes much smaller than the electron probe.

It has been demonstrated previously that c-axis oriented Fe2O3 supported on single crystal (111) oriented SrTiO3 substrates are highly reactive. The highly active grains in this sample show the same orientation relationship, and have similar planes oriented out of the surface. If the charged interface hypothesis presented in Chapter 5 is correct, this could be the same mechanism responsible for the highly reactive nature of these grains. The (001) perovskite surface is neutral, existing as termination of BaO and TiO2 layers. The (111) and (110) surfaces of BaTiO3 are polar, consisting of (111) terminations here, and BaTiO and O$_2$ layers for the (110) surface. The fact that the highly active film grains are all supported on substrate grains with orientations near the polar (111) or (110) surface suggests that the polar surface is responsible for the increased reactivity.

However, as described previously, grains with poor crystallinity and a high concentration of structural defects such as grain boundaries and dislocations are associated with decreased photochemical reactivity. The grains that were not highly active were also the grains believed to be of poor crystalline quality. They were not automatically indexed during EBSD scanning, and manual inspection of the EBSD pattern quality for these locations showed that patterns were extremely poor or non existent for these areas of the sample. As a result, these experiments are not conclusive evidence that the charged surface hypothesis is solely responsible for the differing reactivities of the grains in this sample.

11.4   CONCLUSIONS FOR POLYCRYSTALLINE SUBSTRATES

Heterostructures of Fe2O3 films on polycrystalline BaTiO3 substrates do not show the same photochemical behavior as for TiO2 films on BaTiO3 substrates. No spatially selective reactivity corresponding to ferroelectric domains was observed, even for very thin films. High reactivity was observed on film grains with films near the (0001)

orientation, though whether this is because of the film orientation, substrate surface polarity, or higher crystalline quality of the film is unknown.